TECHNISCHE UNIVERSITÄT DARMSTADT

Enhancing Thermal Energy Storage in blended cementitious Composites through Sensible and Latent Heat Integration

submitted in fulfilment of the requirements for the degree of
Doctor of Engineering (Dr.-Ing.)
to the Department of Civil and Environmental Engineering
of the Technical University of Darmstadt
by Mona Nazari Sam

Darmstadt, 2024

First reviewer: Prof. Dr. Holger Lutze
Second reviewer: Prof. Dr.-Ing. Jens Schneider

Nazari Sam, Mona: Enhancing Thermal Energy Storage in
blended cementitious Composites through Sensible and Latent Heat Integration
Darmstadt, Technische Universität Darmstadt
Year thesis published in TUprints 2024
URN: urn:nbn:de:tuda-tuprints-266808
Date of the viva voce 07.02.2024

Mass and Energy are different forms of the same thing.

$E=mc^2$

(Albert Einstein)

Preamble

To achieve the degree of Doctor of Engineering (Dr.-Ing.) in the Civil and Environmental Engineering Department at Darmstadt University of Technology, this PhD thesis studies the field of thermal energy storage within blended cementitious composites. The main goal of this study is to enhance thermal energy storage capacities in binder-based composite materials by sensible and latent heat integration. The integration of sensible and latent heat mechanisms offers a promising way to improve energy efficiency by reducing energy consumption in the building sector and enabling the expansion of renewable energy infrastructures while contributing to global CO_2 reduction goals.

By Comprehensive research into the fundamental properties, composition, and behavior of blended cementitious composites, the potential for enhanced thermal energy storage to be effectively utilized in these widely used building materials is established. Through strategically applying the principles of sensible and latent thermal energy storage, this work aims to contribute to urgent challenges related to climate change crisis and energy sustainability boom.

The findings and observations presented in this PhD study not only contribute to a better understanding of sensible and latent thermal energy storage principles but also provide a valuable basis for further research, innovation, and applications in the field of energy storage within building insulation materials.

Acknowledgement

My academic journey at Darmstadt University of Technology in the Civil and Environmental Engineering Department comes to an end. In this way, I want to thank all the people who supported me during this challenging time. Their encouragement helped me to shape the most meaningful chapter of my life.

First, I am grateful to my professors, Professor Holger V. Lutze, and Professor Jens Schneider. Their impact on this journey was significant. Their guidance, mentorship and trust have not only influenced my personal growth but have also formed the core of this research. I also want to share my special thanks to Prof. Antonio Caggiano for his constant and great support during this time. He showed me the way to become an independent researcher and lightened my way in the dark parts.

It has been an honor for me to work with outstanding researchers during this time. A special thanks to Prof. Victor Fachinotti for his generous academic support. Very special thanks to Dr. Ignacio Peralta for his continuous encouragement and guidance. They both were always there to discuss scientific topics and answered my questions with generosity.

I want to express my deepest thanks and appreciation to my family in Tehran for their constant love, support, and encouragement during this challenging journey in Germany. Their belief in me was my source of strength.

I am also thankful to my dear friends and colleagues Dr. Neven Ukrainczyk, Adrian Zimmermann, Shifan Zhang, Dr. sha Yang, Dr. Oliver Vogt, Dr. Saulo Rocha Ferreira, Luciano Sambataro, Agustin Laveglia, Helga Janning, Stephan Weber and Yvette Schales, who offered their support during both the highs and lows of this journey. Their friendship and support were a source of comfort and motivation for me.

I would also like to express my sincere thanks to my lovely friends Susanne Hanesch, Ghada Elserafi, Milena Frank, Darja Lykova and Samim Mehdizadeh who have shared the path with me for the last 9 years.

Finally, my warm thanks to everyone who, directly or indirectly, played a role in the completion of this work. Your contributions have been instrumental in my academic journey.

Abstract

The increasing energy consumption for heating and cooling of the continuously growing building stock is a significant cause of the global rise in anthropogenic CO_2 emissions. Efficient management of thermal energy flows throughout, across and around the building envelope can lead to a significant reduction in annual energy consumption for buildings. This, in turn, enhances overall construction energy efficiency by effectively stabilizing temperature fluctuations through the day and across seasons. A highly promising approach to achieve this involves utilizing Phase Change Materials (PCMs) within blended cementitious composites, characterized by a responsive and adaptable porous microstructure that has the potential to store/release solar and/or environmental heat/cooling energy. Unlike common insulation materials, the proposed highly porous thermal energy storage (TES) composite is non-flammable, recyclable, and offers both insulation and effective heat storage/release functionality.

The correlation between microstructural parameters of porous cementitious composites and related thermophysical properties have been the object of extensive study for many decades due to its wide relevance in engineering problems and applications. Research efforts on characterizing thermal properties have predominantly focused on numerically and experimentally assessing the homogenized thermal conductivity of porous cementitious composites. However, these efforts have often disregarded the integration of sensible/latent thermal energy storage, as well as the consideration of the geometrical categorization of the pore structure. The significance of the latter becomes pronounced as the pore volume fraction increases, leading to the predominantly interconnected pores. This issue requires the thorough thermo-physical characterization of individual constituents, including their interconnections and their effects on homogeneous thermal parameters. In this context, a significant contribution of this PhD study is to investigate the optimal balance between thermal insulation and heat storage capacity, utilizing compatible materials and components.

Additionally, a simplified methodology is developed, proposing an analytical predictive model based on the findings from this research and other relevant sources. The proposed analytical model concerns the stochastic characteristic of the pore structure and allows the prediction of homogenized thermal conductivity of porous blended cementitious systems (also known as concrete foam) with/without integrated latent heat thermal energy storage (LHTES). The introduction of two fundamental parameters played a major role in this approach. Particularly, the microstructural fitting parameters A and Φ_m, associated with air inclusion fraction and void geometry, are defined concerning the model proposed by Nielsen (1974). The model parameters were calibrated using a wide variety of experimental data, effectively capturing microstructure's impact on thermal conductivity and TES parameters. The proposed approach aligns well with experimental findings, making it suitable for designing two-phase blended cementitious foams. This methodology is then extended to solve energy transport equations within complex mineral foam structures, including those with LHTES components. Importantly, it eliminates the need for costly experimental setups and complex computer analyses to determine effective thermal conductivity, i.e., k_{eff}.

The suggested novel functional material combines advanced insulation properties with significant energy storage capacity, exceeding improvements by more than 59% for thermal performance (by considering porosities higher than 74%). The determined calibration parameters and established classification of the porous composite given in this work contribute to norms and standards for the thermal characterization of porous mineral composites in application scenarios. The methodology proposed for designing this innovative functional material has the potential to extend its applicability to other porous blended composites.

Zusammenfassung

Der Heiz- und Kühlenergieverbrauch im expandierenden Baubestand trägt maßgeblich zum weltweiten Anstieg der anthropogenen CO_2-Emissionen bei. Die effektive Steuerung der thermischen Energieflüsse und der Wärme- bzw. Kälteverluste über die Gebäudehülle eröffnet eine bedeutsame Gelegenheit zur Reduzierung des jährlichen Energieverbrauchs, indem die täglichen und saisonalen Temperaturschwankungen abgemildert werden. Ein vielversprechender Ansatz hierfür besteht in der Integration von Phasenwechselmaterialien (PCMs) in zementgebundene Verbundstoffe. Diese Verbundstoffe zeichnen sich durch eine adaptive poröse Mikrostruktur aus und bieten das Potenzial, Solar- und/oder Umgebungsenergie in Form von Wärme und Kälte zu speichern und freizusetzen. Im Gegensatz zu konventionellen Isolationsmaterialien weist der vorgeschlagene hochporöse thermische Energiespeicher (TES)-Verbundwerkstoff die Merkmale der Nichtbrennbarkeit und Recycelbarkeit auf, während er gleichzeitig die doppelte Funktion der Isolation und der effektiven Wärmespeicherung und -freisetzung verkörpert.

Die Korrelation zwischen den mikrostrukturellen Parametern poröser zementgebundener Verbundstoffe und den zugehörigen thermophysikalischen Eigenschaften ist seit vielen Jahrzehnten Gegenstand umfangreicher Untersuchungen aufgrund ihrer breiten Anwendbarkeit in ingenieurtechnischen Problemen und Anwendungen. Forschungsbemühungen zur Charakterisierung thermischer Eigenschaften haben sich hauptsächlich auf die numerische und experimentelle Bewertung der homogenisierten Wärmeleitfähigkeit poröser zementgebundener Verbundstoffe konzentriert. Diese Bemühungen haben jedoch oft die Integration sensibler/latenten thermischen Energiespeichers vernachlässigt und die Betrachtung der geometrischen Kategorisierung der Porenstruktur ausgeklammert. Die Bedeutung letzterer wird deutlich, wenn das Porenvolumenverhältnis zunimmt und vorherrschend miteinander verbundene Poren auftreten. Diese Fragestellung erfordert eine gründliche thermo-physikalische Charakterisierung der einzelnen Bestandteile, einschließlich ihrer Wechselbeziehungen und deren Auswirkungen auf homogene thermische Parameter im Verbundmaterial– ein bedeutsamer Beitrag dieser Promotion, der darauf abzielt, ein optimales Gleichgewicht zwischen thermischer Isolierung und Wärmespeicherkapazität unter Verwendung kompatibler Materialien zu erreichen.

Des Weiteren wurde in dieser Arbeit ein vereinfachtes analytisches Vorhersagemodell auf Basis der Erkenntnisse aus dieser Forschung und anderer relevanter Quellen entwickelt. Das analytische Modell bezieht sich auf die stochastische Charakteristik der Porenstruktur und ermöglicht die Vorhersage der homogenisierten thermischen Leitfähigkeit von porösen zementgebundenen Verbundwerkstoffen mit oder ohne integrierte latente Wärmespeicherung (Latent Heat Thermal Energy Storage). Die mikrostrukturellen Kalibrierungsparameter A und Φ_m, die mit Luftanteil und Porengeometrie in Verbindung stehen, werden anhand des von Nielsen (1974) vorgeschlagenen Modells definiert. Die Modellparameter wurden anhand verschiedener experimenteller Daten kalibriert und erfassen effektiv den Einfluss der Mikrostruktur auf die thermische Leitfähigkeit für die Gestaltung von zweiphasigen zementgebundenen Verbundwerkstoffen.

Diese Methodik wird anschließend erweitert, um Energieübertragungsgleichungen in komplexen zementgebundenen Schaumstoffstrukturen zu lösen, einschließlich solcher mit LHTES-Komponenten. Dabei entfällt die Notwendigkeit für aufwendige experimentelle Aufbauten und komplexe Computeranalysen zur Bestimmung der effektiven thermischen Leitfähigkeit (k_{eff}).

Das vorgeschlagene Funktionsmaterial (hochporöse, zementgebundene Verbundwerkstoffe mit oder ohne integrierte latente Wärmespeicherung) vereint fortschrittliche Isolationseigenschaften, die jene herkömmlicher Schichten übertreffen, mit erheblicher Energiespeicherkapazität und die Verbesserungen bei der thermischen Leistung um mehr als 59 % (Porosität höher als 74 %). Zudem wird eine effiziente Methodik zur Gestaltung dieses innovativen Funktionsmaterials entwickelt. Die ermittelten Kalibrierungsparameter und die etablierte Klassifizierung des porösen Verbundwerkstoffs tragen zur Entwicklung von Normen und Standards für die thermische Charakterisierung von porösen mineralischen Verbundwerkstoffen in verschiedenen Anwendungsszenarien bei. Diese Methode hat das Potenzial, ihre Anwendbarkeit auf andere poröse Verbundwerkstoffe auszuweiten.

Content

Nomenclature

Symbol	Designation
b	thermal effusivity
C_p	Heat capacity at constant pressure
ρC_p	Volumetric heat capacity at constant pressure
c_p	specific heat capacity at constant pressure
k, λ	thermal conductivity
k_{eff}, λ_{eff}	effective thermal conductivity
H, h	enthalpy
L	length
m	mass of sample material
Q	quantity of stored heat
R	thermal resistance
U	thermal transmittance
t	time
T	temperature
T_m	melting temperature
d	thickness
V	volume
X	Cartesian coordinate
α	thermal diffusivity
β, R	heat rate constant
ε, p	porosity
ρ	density
Φ	heat flow, heat flux

List of Abbreviations

Abbreviation	Explanation
PCMs	Phase Change Materials
MPCMs	Microencapsulated Phase Change Materials
TES	Thermal Energy Storage
LHTES	Latent Heat Thermal Energy Storage
TESS	Thermal Energy Storage Foam
NZEBs	Nearly-Zero Energy Buildings
IEA	International Energy Agency
DSC	Differential Scanning Calorimetry
EPS	Expandiertes Polystyrol

List of Figures

List of Tables

1 Introduction

1.1 Motivation and context of the study

Today, about 75% of the building stock in the EU lacks energy efficiency, resulting in a substantial portion of utilized energy being wasted [1]. Furthermore, as indicated by the International Energy Agency, the floor area within the global buildings sector is anticipated to increase by 75% between 2020 and 2050. While the heating and cooling sector is steadily transitioning towards cleaner, low-carbon energy sources, approximately 75% of the fuel consumed in this sector still originates from fossil fuels [2]. As of 2021, a challenging goal was proposed by the European Commission: “Europe must realize a fully decarbonized and zero-emission building stock by 2050 [3]”. To successfully achieve the ambitious decarbonization goal, substantial reductions in both space heating and cooling demands are necessary, achievable through building envelope improvements in Nearly-Zero Energy (NZE) retrofit and new constructions [4].

Notably, space cooling has experienced the fastest growth among building end-uses since the year 2000 due to elevated temperatures, including around 21.5 million buildings in Germany [5]. In 2020, space cooling accounted for only 5% of global building energy use. This demand is expected to increase in the coming decades, with 650 million air conditioners expected by 2030 and an extra 2 billion by 2050. Annual electricity demand for space cooling rises by 1%, reaching 2,500 TWh by 2050 [6]. Considering these facts, every preserved kilowatt-hour of thermal energy, whether heat or cold, achieved through enhancements in the thermal envelope, directly and consistently enhances the building's energy performance, energy efficiency, and contributes to climate protection.

In practical application, to achieve enhancements in the thermal envelope involves selecting materials with higher thermal resistance (R-value) or lower thermal transmittance, also known as the heat transfer coefficient (U-value). Nevertheless, this is not universally true, as several studies demonstrate that increasing thermal resistance beyond a certain point may lead to an increase in the overall annual energy consumption. This highlights the significance of additional factors such as internal heat gains and the cooling/heating set-point temperature in energy analysis [7]. Highly insulated buildings are prone to overheating due to quicker

internal temperature response to solar and internal gains. In addition, from a technical standpoint and based on the present state of knowledge, there exists a finite limit to reducing the U- value (1/thickness/thermal conductivity) of building envelopes. This achievable U-value is limited by factors such as the existing wall structure, the insulation material's thickness and thermal conductivity of the insulation layer [8].

Overcoming the mentioned limitations and drawbacks involves focusing on the dynamic energy performance of the building envelope, primarily through the implementation of thermal adaptive systems. These envelopes demonstrate an impressive ability to adapt to fluctuating inputs, including solar radiation, oscillations in outdoor temperature, occupancy patterns, and the heating/cooling demands influenced by both seasonal and daily climatic variations [9].

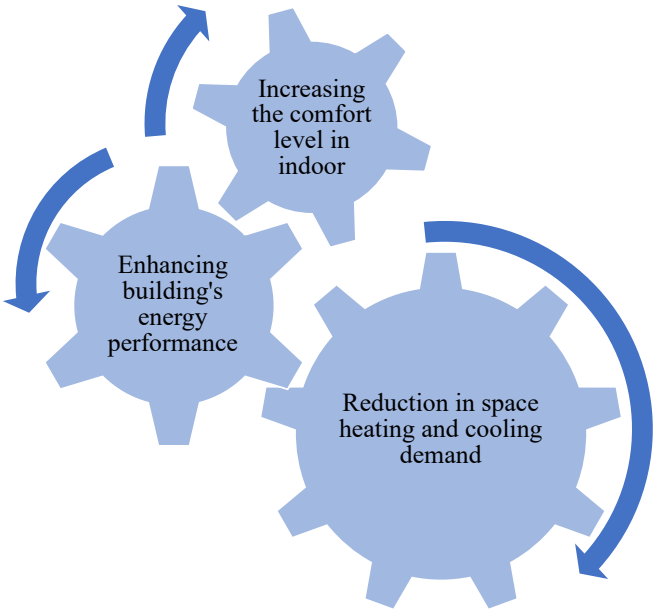

Figure 1. Study's overall goals.

In thermally adaptive systems, the primary material parameters of significance include not only thermal resistance (R-value) but also sensible/latent heat storage capacity (C_p) of the system. Incorporating both high thermal resistance and significant sensible /latent heat capacity within the envelope will overcome the mentioned limitations and drawbacks linked to conventional static insulators [10] and lead to exceptional overall thermal performance. In this context, thermal energy storage (TES) plays a key role in shaping the future of NZE structures, to both fulfill the need for increasing the comfort level and reducing energy demand in buildings, as aimed in this study, see Figure 1.

Thermal energy storage (TES) in construction elements can be attained using sensible, latent, and thermochemical-based materials. Among these, latent heat storage polymers, also known as Phase Change Materials (PCMs), offer a bright perspective in building solutions [11]. Advanced insulation materials in combination with intelligent passive energy storage systems based on phase change materials (PCMs) can significantly reduce energy consumption for heating and cooling in buildings [12]. Phase change materials (PCMs) have the property of undergoing a phase change at specific temperatures, absorbing, or releasing energy in the process [13]. Among the spectrum of studied techniques, the microencapsulation of PCMs and

their integration into construction materials, especially within the thermal envelope, stands out for its superior thermal performance [14] [15].

In the ongoing developments within the construction industry, where cement usage has expanded over the last century due to its cost-effectiveness, durability, and recyclability, innovations have been mainly focused on enhancing performance, efficiency, and sustainability [16]. These advancements involve transforming cement-based materials into insulation and thermal energy storage composites, progressing towards more sustainable construction practices [17].

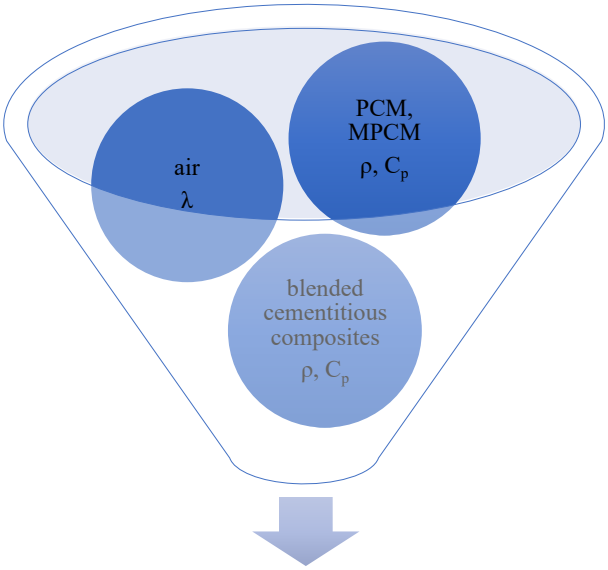

Figure 2. Developing thermally adaptable insulations from cementitious composites with a significant volume of air and combined insulation/heat storage functionality.

Cementitious materials with a controlled volume of air voids, achieved through physical homogenization and referred to as porous cementitious composites or thermal energy storage foam (TESS), exhibit excellent insulating properties, see Figure 2 [18]. The thermal insulation characteristics of porous cementitious composites are significantly influenced by the micro-scale porous structure within the material. Inclusion of small air-filled pores results in superior insulating properties characterized by significantly lower thermal conductivity when compared to the original dense mineral structure [19]. This correlation is particularly based on the specific chemical composition of the cement and any additional components used [20]. These composite materials derive their mechanical strength from the geometric structure of the internal cementitious lamellas enveloping the air bubbles [21]. Optimizing the micro-meso structure of the porous structure to maximize the proportion of air and incorporating latent heat storage microcapsules can substantially decrease resource consumption and CO_2 emissions over the lifespan of the material [22].

Through the intelligent addition of microencapsulated phase change materials (MPCMs) within the lamellae of the binder structure of the foam, a significant improvement in the energy performance of Thermal Energy Storage Foam (TESS) can be achieved [21][22][23]. The latter presents a practical solution to fabricate

lightweight, robust, durable, and multifunctional structures for utilizing locally accessible renewable resources and harmonizing indoor energy demand and supply [24]. The combination of the high insulation provided by porous cementitious foam (TESS) with the significant heat storage capability of MPCM results in a thermally adaptable envelope with a combined insulation and storage function for building applications [25]. These advanced materials exhibit a porous microstructure that is responsive to external parameters and holds the potential to store and release energy through cyclic and reversible phase transitions between solid and liquid states (or viceversa). The inclusion of blended cement composite as base material or skeleton often results in foams with reduced density, enhanced thermal and acoustic performance, improved mechanical properties, enhanced fire-resistant characteristics and lower environmental impact compared to certain traditional insulation materials [26].

This strategic approach aims to reduce overall annual heat/cold loss while simultaneously increasing the thermal inertia of the building envelope through improved heat storage potential. However, given the complex nature of dynamic envelope behavior and control parameters, including the incorporation of heat storage, it is important to assess energy-saving potentials during the design phase and evaluate the overall building energy usage. Providing standardized data on TESS insulation materials, with or without MPCM, including information about density, thermal conductivity, specific heat, enables a uniform and comparable LCA-based approach for assessing the sustainability of the advanced TESS composites [27].

This requires a thorough analysis within individual components and their interconnection to the overall material efficiency. This analysis involves optimizing/reducing cement usage, adjusting maximum porosity, maximizing the MPCM contribution, and enhancing overall material efficiency, see Figure 2. The result is a decrease in embodied emissions and a significant incorporation of both bio-sourced and environmentally friendly materials, as developed within the scope of this PhD Thesis.

1.2 Research Objectives

Based on the previously mentioned aspects and identified research gaps, the main research objective of this PhD thesis can be formulated as follows:

Experimental, Empirical and Theoretical demonstration of the combined Influence of Sensible and Latent Heat Storage on the Insulation Capacity of Porous blended cement-based Composites

To address this objective, it is important to assess materials and methodologies for their potential applications. Consequently, the following specific sub-research objectives are formulated:

1. **PCM COMPONENT MICRO-LEVEL: “A comparative Study on the Thermal Energy Storage (TES) Performance of Bio-based and Paraffin-based PCMs”**

This contributes to the following research gaps:

- Dynamic Analysis: Limited research focuses on understanding the dynamic behavior of PCMs under various heating and cooling rates, which is essential for real-world applications [15].

- Characterization Techniques: developing improved techniques to accurately characterize the thermal properties of PCMs, especially at different phases.
- Standardization of characterization methods: establishment of uniform and consistent procedures for assessing the thermal properties of phase change materials to ensure comparable results when characterizing PCMs. This allows for better benchmarking and evaluation across different studies and applications. Standardized procedures are needed to enhance the reliability of data by minimizing variations introduced by different testing techniques and/or used equipment. This reliability is required for making informed decisions about PCM selection and application.
- Transitioning from paraffin-based phase change materials (PCMs) to bio-based alternatives: representing a strategy to address the environmental concerns linked with paraffin-based PCMs, preserving to minimize any impact on performance. These substitutes must maintain thermal compatibility and enabling efficient separation through recycling. This effort resulted in the development of a new generation of environmentally friendly energy storage materials, which stands as a remarkable contribution of this PhD study.[1]

2. PCM-PASTE COMPOSITE MICRO-LEVEL: "Enhancing Thermal Energy Storage of Mineral-Based Composites through Microencapsulated Phase Change Materials: Thermophysical and Mechanical Investigation "

The Research contributes to the following research gaps:

- Performance Optimization: optimizing the formulation and integration of microencapsulated phase change materials within blended cement-based composites to achieve maximum thermal energy storage efficiency.
- Thermomechanical Coupling: understanding the interactions between thermal cycling and mechanical properties of the composites.
- Enhanced Thermophysical Characterization: assessing measurement techniques to accurately characterize the thermophysical properties of these composites, particularly in relation to their phase change behavior.
- Material Compatibility: investigating the compatibility of blended cement-based matrices with the polymeric shell of Microencapsulated Phase Change Materials (MPCMs) to ensure effective synergy.
- Providing thermophysical properties for implementation in subsequent investigations of adaptive insulation: extensive research on the thermophysical properties essential for future studies on adaptive insulation and enhanced thermal energy storage using MPCMs.

[1] https://patentscope.wipo.int/search/en/detail.jsf?docId=DE391896767&_cid=P10-LEPCLD

3. **PCM-FOAM COMPOSITE MESO-LEVEL: “Modelling porous cementitious media with/without integrated latent heat storage “**

The study contributes to the following research gaps:

- Model Efficiency: developing an approach that's both efficient and precise. Balancing complexity with a simplified methodology to develop a valuable tool for engineers. The latter helps to better understand, predict, and optimize the thermal conductivity/thermal performance of porous cementitious media with/without integrated latent heat storage in the context of adaptive building envelope design.
- Integrating Latent Heat Storage: formulating a concise and accurate analytical technique that examines the influence of integrated latent heat storage materials on the thermal behavior and conductivity of porous mineral-based media.
- Validation and Experimental Data: obtaining comprehensive experimental data on the thermal behavior and performance of porous blended cement-based composites, considering relevant input parameters.
- Evaluating Insulation Efficiency: comparing the Insulation Capacity of blended cement-based composites with and without integrated latent heat against conventional insulators while evaluating relevant parameters for adaptive envelopes, including thermal diffusivity and effusivity.

1.3 Research Methodology

The research methodology for this study is structured into three main steps, each of these steps is based on the existing literature to construct a detailed plan to achieve the study's objectives, see Figure 3:

Components: The first step involves a comprehensive study on individual components that play an important role in the thermal energy storage system. This phase aims to build a robust foundation of knowledge regarding the thermal energy storage properties, characteristics, and behaviors of individual components.

Composites (Micro-): Moving to the second step, the focus shifts to the design of the matrix material and composite structure. Based on the observations gathered from the analysis of individual components, this phase involves combining these components to create an integrated matrix material. The goal is to establish a composite structure that optimally stores and releases thermal energy. This step also considers factors such as compatibility, efficiency, and mechanical properties to ensure the resulting matrix material aligns with the study's objectives.

Foam Predictive Model (Meso-): In the final step, a novel methodology is developed, proposing an analytical predictive model based on the findings from this research and other relevant sources. This model provides a practical tool for evaluating the thermal performance of the porous blended cement-based composite systems using results from the initial two steps. By measuring important factors connected to thermal energy storage in the composite, it becomes possible to evaluate the system's efficiency. Moreover,

this adaptable approach enables iterative optimization. Consequently, the whole system can be improved based on future observations, finally improving the overall performance of the mineral-based thermal energy storage systems in a sustainable way.

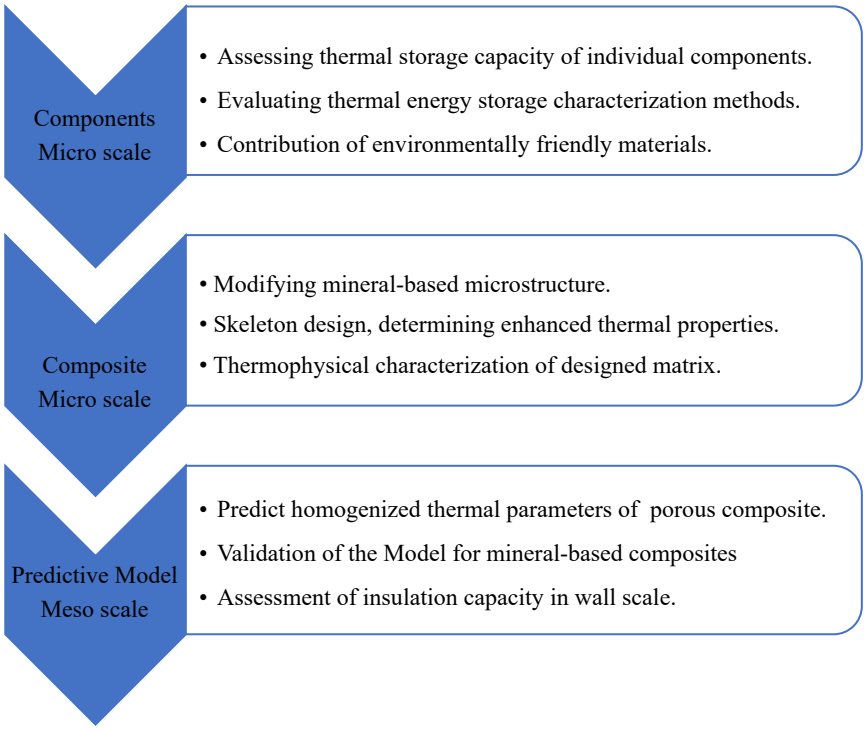

Figure 3. Applied research methodology in this study, illustrated in three main Steps (scales).

The previously mentioned objectives and research steps are related to three publications that contribute to this cumulative dissertation:

Publication 1: Nazari Sam, M., Caggiano, A., Mankel, C., & Koenders, E. (2020). A comparative study on the thermal energy storage performance of bio-based and paraffin-based PCMs using DSC procedures. Materials, 13(7), 1705. DOI: 10.3390/ma13071705, IF: 3.4.

The published version is reproduced in Chapter 2.1 of the thesis.

Publication 2: Sam, M., Caggiano, A., Dubyey, L., Dauvergne, J. L., & Koenders, E. (2022). Thermo-physical and mechanical investigation of cementitious composites enhanced with microencapsulated phase change materials for thermal energy storage. *Construction and Building Materials*, *340*, 127585. DOI: 10.1016/j.conbuildmat.2022.127585, IF: 7.4.

The published version is reproduced in Chapter 2.2 of the thesis.

Publication 3: Nazari Sam, M., Schneider, J., & Lutze, H. V. (2023). Modelling Porous Cementitious Media with/without Integrated Latent Heat Storage: Application Scenario. *Energies*, *16*(18), 6687. DOI: 1073/16/18/6687, IF:3.2.

The published version is reproduced in Chapter 2.3 of the thesis.

1.4 Synopsis

This cumulative PhD thesis presents a comprehensive study through the development of blended cement-based thermal energy storage (TES) composites, centering on three main chapters: Introduction, Research Contributions and Conclusion plus future research directions, see Figure 4.

Chapter 1 serves as an introduction, laying the foundation by introducing the significance of thermal energy storage and outlining the research objectives. Then, the core of the thesis lies within the chapter on research contributions. This chapter addresses three primary objectives. Firstly, a detailed experimental study of individual components, critical and essential to the composite's functionality is presented (see also **Publication 1**). This analysis provides a deep understanding of the fundamental properties and behaviors of these components. Moving forward (i.e., **Publication 2**), the focus shifts to designing an integrated matrix material and composite structure. This step experimentally combines the components, considering compatibility, efficiency, and mechanical properties.

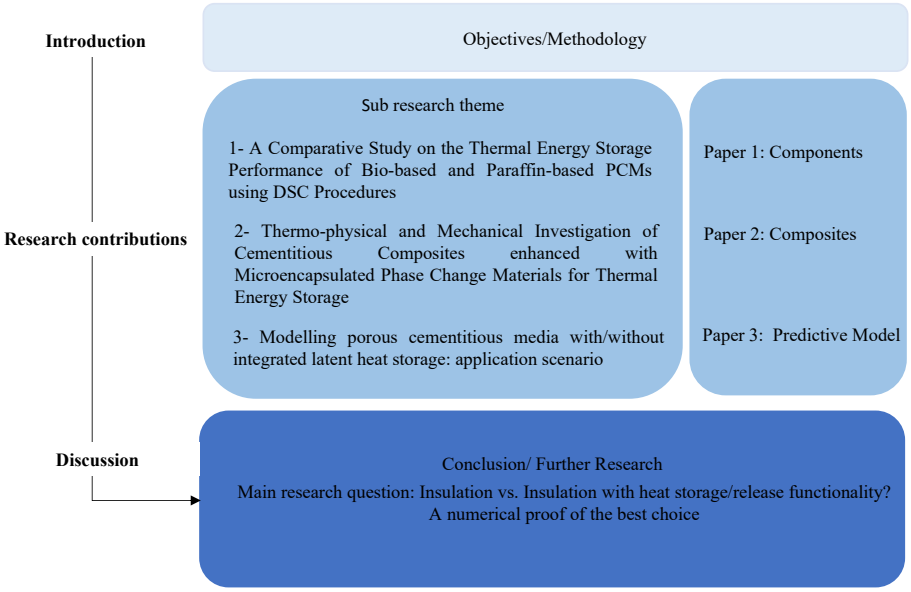

Figure 4. Framework of the study including the introduction, research contributions and conclusion/further research.

Finally, the study progresses further by presenting an analytically based methodology that includes a predictive model for porous TES systems. Synthesizing research findings and external sources, this model (see also **Publication 3**) develops into a practical tool for assessing the thermal performance of the porous cementitious composite systems employable for dynamic envelopes. The methodology's adaptive nature eases iterative optimization, allowing constant improvement based on progressive findings.

The concluding chapter of the thesis highlights the possibilities for further advancements in the field of porous TES systems, particularly their application as adaptable envelopes for achieving CO_2 reduction goals and realizing energy-efficient solutions in the context of nearly zero energy buildings (NZEBs). Finally, this work provides a roadmap for potential future innovations, making a long-term impact on the field of porous thermal energy storage (TES) systems.

References

[1] https://commission.europa.eu/news/focus-energy-efficiency-buildings-2020-02-17_en, (accessed on 27 October 2023).

[2] https://eur-lex.europa.eu/legal-content/EN/TXT/?uri=CELEX%3A52016DC0051, (accessed on 27 October 2023).

[3] https://energy.ec.europa.eu/topics/energy-efficiency/energy-efficient-buildings/energy-performance-buildings-directive_en, (accessed on 27 October 2023).

[4] https://www.iea.org/energy-system/buildings/building-envelopes, (accessed on 27 October 2023).

[5] https://www.dena.de/themen-projekte/energieeffizienz/gebaeude/, (accessed on 27 October 2023).

[6] https://www.energy.gov/sites/default/files/2021-12/IEA, Net Zero by 2050.pdf, 141-146, (accessed on 27 October 2023).

[7] Fawaier, M., & Bokor, B. (2022). Dynamic insulation systems of building envelopes: A review. Energy and Buildings, 270, 112268.

[8] https://www.bmwk.de/Redaktion/EN/Publikationen/energy-efficiency-strategy-buildings.pdf, (accessed on 27 October 2023).

[9] Wang, J. J., & Beltran, L. (2016). Energy Performance Of Future Dynamic Building Envelopes. In Proceedings of the 3rd IBPSA-England Conference BSO 2016.

[10] Casini, M. (2020). Insulation materials for the building sector: A review and comparative analysis. Encyclopedia of Renewable and Sustainable Materials, 121-132.

[11] Wang, P., Liu, Z., Zhang, X., Hu, M., Zhang, L., & Fan, J. (2023). Adaptive dynamic building envelope integrated with phase change material to enhance the heat storage and release efficiency: A state-of-the-art review. Energy and Buildings, 112928.

[12] Romdhane, S. B., Amamou, A., Khalifa, R. B., Said, N. M., Younsi, Z., & Jemni, A. (2020). A review on thermal energy storage using phase change materials in passive building applications. Journal of Building Engineering, 32, 101563.

[13] Carlucci, F., Cannavale, A., Triggiano, A. A., Squicciarini, A., & Fiorito, F. (2021). phase change material integration in building envelopes in different building types and climates: Modeling the benefits of active and passive strategies. Applied Sciences, 11(10), 4680.

[14] Suresh, C., Hotta, T. K., & Saha, S. K. (2022). Phase change material incorporation techniques in building envelopes for enhancing the building thermal Comfort-A review. Energy and Buildings, 268, 112225.

[15] Wang, X., Li, W., Luo, Z., Wang, K., & Shah, S. P. (2022). A critical review on phase change materials (PCM) for sustainable and energy efficient building: Design, characteristic, performance and application. Energy and Buildings, 260, 111923.

[16] Belaïd, F. (2022). How does concrete and cement industry transformation contribute to mitigating climate change challenges?. Resources, Conservation & Recycling Advances, 15, 200084.

[17] Asdrubali, F., D'Alessandro, F., & Schiavoni, S. (2015). A review of unconventional sustainable building insulation materials. Sustainable Materials and Technologies, 4, 1-17.

[18] Zhilyaev, D., Fachinotti, V. D., Zanoni, F., Ortega, A., Goracci, G., Mankel, C., ... & Jonkers, H. M. (2023). Early-stage analysis of a novel insulation material based on MPCM-doped cementitious foam: Modelling of properties, identification of production process hotspots and exploration of performance trade-offs. Developments in the Built Environment, 100243.

[19] Du, Z., Zuo, W., Wang, P., & She, W. (2022). Ultralight, super thermal insulation, and fire-resistant cellular cement fabricated with Janus nanoparticle stabilized ultra-stable aqueous foam. Cement and Concrete Research, 162, 106994.

[20] Rashad, A. M., Essa, G. M., & Morsi, W. M. (2022). Traditional cementitious materials for thermal insulation. Arabian Journal for Science and Engineering, 47(10), 12931-12943.

[21] Wagh, C. D., Indu Siva Ranjani, G., & Kamisetty, A. (2021). Thermal properties of foamed concrete: a review. In 3rd International Conference on Innovative Technologies for Clean and Sustainable Development: ITCSD 2020 3 (pp. 113-137). Springer International Publishing.

[22] Gencel, O., Bilir, T., Bademler, Z., & Ozbakkaloglu, T. (2022). A detailed review on foam concrete composites: Ingredients, properties, and microstructure. Applied Sciences, 12(11), 5752.

[23] Parameshwaran, R., Naresh, R., Ram, V. V., & Srinivas, P. V. (2021). Microencapsulated bio-based phase change material-micro concrete composite for thermal energy storage. Journal of Building Engineering, 39, 102247.

[24] Kumar, D., Alam, M., Sanjayan, J., & Harris, M. (2023). Comparative analysis of form-stable phase change material integrated concrete panels for building envelopes. Case Studies in Construction Materials, 18, e01737.

[25] Snehal, K., & Das, B. B. (2022). Pozzolanic reactivity and drying shrinkage characteristics of optimized blended cementitious composites comprising of Nano-Silica particles. Construction and Building Materials, 316, 125796.

[26] Pavel, C. C., & Blagoeva, D. T. (2018). Competitive landscape of the EU's insulation materials industry for energy-efficient buildings. PUBSY No. JRC108692 EUR, 28816.

[27] Grazieschi, G., Asdrubali, F., & Thomas, G. (2021). Embodied energy and carbon of building insulating materials: A critical review. Cleaner Environmental Systems, 2, 100032.

2 Research Contributions

2.1 A Comparative Study on the Thermal Energy Storage Performance of Bio-based and Paraffin-based PCMs using DSC Procedures

This Chapter is published in: Materials, 13(7), 1705, Nazari Sam, M., Caggiano, A., Mankel, C., & Koenders, E. (2020). A comparative study on the thermal energy storage performance of bio-based and paraffin-based PCMs using DSC procedures.
Author Contributions: Conceptualization, M.N.S. and A.C.; methodology: materials, methods, and processing M.N.S., C.M. and A.C.; data curation, M.N.S., C.M. and A.C.; writing—original draft preparation, M.N.S. and A.C.; writing—review and editing, everybody; supervision, A.C. and E.K.; project administration, E.K.; funding acquisition, E.K.

2.1.1 Introduction

The global challenge to strongly cut back the use of fossil fuels with the aim to implement renewable resources and to neutralize greenhouse gas emissions make energy efficiency a key issue that is at the center of our society [1,2]. According to the EU commission, heating and cooling the residential and non-residential sector accounts for half of the EU's energy consumption, while about 84% of it is still generated from fossil resources [3]. Since the introduction of the new EU Buildings Directive 2019/2021 [4], all member states are obliged to guarantee that all new constructions are designed as "Nearly Zero Energy Buildings" (NZEBs), from the beginning of 2021. This obligation has been already applied to non-residential buildings from the beginning of 2019. Therefore, the development of new and smart energy storage solutions and technologies,

with the aim to use environmental thermal energy more efficiently, and to balance out daily heating/cooling demands, are worth investigation for building applications [5,6].

One promising technique available for Thermal Energy Storage (TES) applications is by implementing Phase Change Materials (PCMs) in construction and building composites [7]. PCMs can be used to store large quantities of heat, not only through their sensible capacity, but also (sometimes predominantly) via their latent storage property [8]. As PCMs can store large amounts of latent heat at constant temperature, they are contributing to the energy efficiency and thermal comfort of residential and non-residential buildings, by balancing out daily environmental heat demands [9]. Consequently, the passive storage/release of latent heat through phase transitions from solid to liquid or vice versa, allows to save considerable amount of primary energy [10]. The principle of latent TES can be employed in a wide range of applications [11], such as, solar heating systems [12], building air conditioning [13], building envelope [14], production of energy-saving cementitious composites [15] and high porous insulation systems [16], waste heat recovery in residential and non-residential sectors [17], and many other applications [18].

Designing large-scale practical applications for passive latent thermal energy storage systems requires in-depth knowledge on the thermal characteristics of PCM before, during and after its phase change. Therefore, an accurate and correct determination of the thermal properties of PCM systems is crucial to efficiently design composite systems or devices that use latent TES [19].

Differential Scanning Calorimetry (DSC) is an effective method to characterize the thermal behavior of PCMs, and to determine their TES capacities, in terms of transition temperature, enthalpy and specific heat, and its stability throughout the various melting and crystallization cycles. The heating and cooling rates of DSC measurements are typically much faster than in real applications, while the sample mass is also very small (less than 90 mg), which might lack representativity for real size applications [20,21]. Some commercially calorimeters are already available on the market for measuring and analyzing larger sample masses with a very high precision and adopting quite low heating rates (as low as 0.01 K/min). Samples with a large mass implicitly show a lower error ratio resulting from reduced sample inhomogeneity. However, larger samples may also strongly affect the course of the measured phase change temperatures (i.e., the onset temperature or the maximum one). It follows that DSC measurements can be affected by changing the heating/cooling rate and/or sample mass. They mainly influence the thermal equilibrium status in the sample, thus producing a shifting of the phase change temperature and lead to non-realistic shapes of the heat capacity and/or enthalpy temperature responses $h(T)$ [22]. Moreover, DSC test results depend on further factors such as sample preparation, correct calibration of the experimental set-up, and many other factors that should, in fact, be standardized to achieve comparable and objective results, under different test environments [23]. Therefore, developing an appropriate and objective methodology, in this field, is essential to improve the accuracy of the PCM characterization procedure and to make measurement errors negligible [24].

An alternative method that overcomes the DSC limitations (i.e., mass influence and heating rate effects) is the T-History Method (THM), which was originally developed by Yinping and Yi [25]. The method records the time–temperature evolutions of PCM samples against a well-known reference material, usually water.

THM easily allows to evaluate the heat capacity, temperature of melting/crystallization, enthalpy, and phase change temperature. The accuracy and soundness of this method was evaluated by many researchers, see for example [26–28]. Hong et al. [29] verified the accuracy of a modified THM for several PCMs, having different freezing patterns. A further improvement of the THM measurement technique was developed by Stankovic and Kyriacou [30]. A procedure to numerically correct the enthalpy-temperature response of PCMs obtained from THM was developed by Tan et al. [31]. Then, a critical comparison between DSC and THM was done by Rathbeger et al. [32]. The authors mainly concluded that the key difference between both methods is represented by the sample size of the investigated material, and the temperature profile to which they are subjected. THM samples are much larger than DSC samples (about 1000 times), while also constant heating and/or cooling temperatures are applied. In addition, THM minimizes heating/cooling rate effects, overcomes sample size issues, and can be used for low thermal conductivity samples. The only drawback of THM, which is crucial for standardized measurements and test procedures, is that the accuracy of the lab results largely depends on the measuring procedures and the self-built calorimeters. For this reason, measurements from different laboratories can differ a lot and are generally not comparable [33].

The main objective of this work is to investigate the thermo-physical properties and heat storage capacity of a representative organic bio-based (non-paraffin) PCM, in terms of phase-change enthalpy, specific heat capacity and melting temperature, using different experimental setups. The influence of various parameters, involved in DSC measurements, are compared with results done on three comparable paraffin waxes. The measurements are carried out in accordance with the currently available standard of the International Energy Agency (IEA), i.e., under the Task 42 Annex 29, to characterize the thermal-energy properties of the PCMs under discussion. Heat-flux DSC dynamic measurements and DSC stepwise procedures are considered and compared to scrutinize the aims.

To the Authors' best knowledge, only a few studies on thermal analysis (even under the still not published final version of the IEA-SHC 42 Annex 29 Standard for common PCMs) are so far available in scientific literature dealing with the use of bio-based PCM. Moreover, no Standard is currently available on the thermal analysis of organic PCMs, but there are some discussions going on in this direction. In this context, with the current paper, the authors like to contribute to this discussion by presenting the differences in DSC responses between three commonly used petroleum-based PCMs (paraffinic) and one novel bio-based PCM. Especially highlighting the differences in TES characteristics and data of various kinds of PCMs, in a general sense. Thus, this document tried to examine if the currently employed procedures can also be applied to other types of PCMs, such as the considered bio-based one investigated in this work. In addition, the presented results lead to demonstrate the feasibility of completely substituting petroleum-based PCMs with a more environmentally friendly bio-based one. This aspect may open doors for a new scenario in research for developing novel PCMs, that can be employed in thermal storage materials for building construction materials, which can be more sustainable, eco-friendly and energy-saving.

The paper is structured as follows: Section 2 reports Materials and Methods of the experimental program and outlines the key thermophysical characteristics of the investigated materials and shows the overall

experimental program. Then, in Section 3, the experimental results for both paraffin and bio-based PCMs are described following the dynamic DSC procedure. Section 4 outlines the results of the stepwise approach where some comparisons between the two alterative procedures are conducted to characterize the TES of the PCMs. Finally, concluding remarks and future developments of this research are addressed in Section 5.

2.1.2 Materials and Methods

In this section, the employed materials, methods, and experimental program, considered for analyzing the TES properties of the selected PCMs, are presented. Particularly, two types of organic phase change materials are analyzed, namely three Paraffin Waxes and one Bio-based PCM, which have physical, kinetic, chemical, and economic relevance for constructions and building application in civil engineering [34,35].

2.1.2.1 Paraffin Wax

Three commercial paraffin-based waxes (RT-series® by Rubitherm GmbH, Berlin, Germany) are used as reference PCMs. These commercial products, having a melting temperature T_m that ranges between 22 °C and 26 °C (suitable for enhancing the thermal comfort in building applications) are selected for this study. More specifically, RT24, RT25 and RT26 are taken into consideration which are characterized with a T_m of 24 °C, 25 °C and 26 °C, respectively.

2.1.2.2 Bio-based PCM

One bio-based PCM has also been investigated in this work as an eco-friendly alternative to the petroleum-based paraffin wax. The bio-based material, viz. PureTemp25 by PureTemp LLC (Minneapolis, MN, USA), made of natural oils with a T_m of 25 °C, is used, while its results can be directly compared to RT25. The thermal properties of the RTs and the biobased PCM are listed in Table 1.

Table 1. Properties of RT24, 25, 26 and PureTemp25 as given by manufacturers´ datasheets [36, 37] l: liquid, s: solid, a: average liquid and solid.

Properties	RT24	RT25	RT26	PureTemp25
Tm (main peak) [°C]	24	25	26	25
Density liquid [kg/l]	0.77 (40 °C)	0.76 (at 40 °C)	0.75 (at 30 °C)	0.86
Density solid [kg/l]	0.88 (15 °C)	0.88 (at 15 °C)	0.90 (at 20 °C)	0.95
Spec. Heat Capacity, l [kJ/kg×K]	-	-	-	2.29
Spec. Heat Capacity, s [kJ/kg×K]	-	-	-	1.99
Spec. Heat Capacity, a [kJ/kg×K]	2	2	2	-
Heat storage capacity [kJ/kg]	160 (16–31 °C)	170 (16–31 °C)	180 (19–34 °C)	187*

**Measurement interval not available in the Datasheet.*

2.1.2.3 Methods

This section reports the methods used to investigate the TES properties of the PCMs presented in Sections 2.1 and 2.2. Two alterative heat-flux DSC methods (Figure 5), namely the dynamic and a stepwise method,

have been considered for this purpose. The German Standards DIN 51005 [38] and DIN 51007 [39] have been considered as a reference to perform the DSC tests (generally applied for this test method to any kind of material), while the IEA standard procedure [40] is followed to determine the heat storage capacity of PCMs.

This section reports the methods used to investigate the TES properties of the PCMs presented in Sections 2.1 and 2.2. Two alterative heat-flux DSC methods (Figure 5), namely the dynamic and a stepwise method, have been considered for this purpose. The German Standards DIN 51005 [38] and DIN 51007 [39] have been considered as a reference to perform the DSC tests (generally applied for this test method to any kind of material), while the IEA standard procedure [40] is followed to determine the heat storage capacity of PCMs.

(a) (b) (c)

Figure 5. (a) Differential Scanning Calorimetry (DSC) 214 Polyma equipment from company Netzsch (Selb, Germany, with a T work range −170 °C to 600 °C — Heating/Cooling rate 0.001 K/min to 500 K/min — Indium Response Ratio > 100 mW/K — Resolution (technical) 0.1 µW — Enthalpy precision ± 0.1% for indium, ± 0.05% to ± 0.2% for most samples), (b) aluminum sample holders (maximum volume capacity of 40 µL) and (c) position into the DSC device.

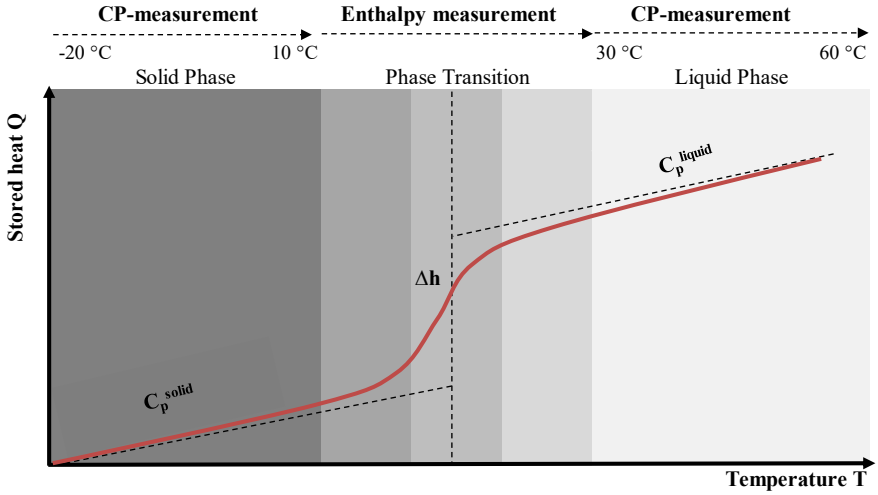

Figure 6. Separation of the measurements in 3 phases: (i) heat (sensible) capacity in solid phase, (ii) heat (latent) capacity under phase change, and (iii) heat (sensible) capacity in liquid phase according to DIN EN ISO 11357-3.

Characterizing the PCMs was done by measuring three cycles over three different temperature ranges: i) solid phase (−20 to 10 °C); ii) phase change/transition (melting and/or crystallization), (10 to 30 °C); and (iii) liquid phase (30–60 °C). Figure 6 shows these three ranges that occur during the DSC heating/cooling tests and describes the typical enthalpy and specific heat capacity evolutions of non-isothermal PCMs.

It may be worth highlighting that only for the dynamic DSC tests, and following the IEA indications [40], each sample measurement consisted of 3 (DSC) cycles over the pre-defined temperature range (−20 to 60 °C). Particularly, the first cycle was performed to eliminate previous thermal histories of the specimen; the second cycle was carried out to identify the TES characteristics; and finally, the third one was done mainly to check the reproducibility of the results and the possible appearance of cyclic chemical instability of the material.

Dynamic DSC Method and Evaluation of TES Parameters

The most common way to operate DSC tests is by performing the experimental procedure with a constant heating/cooling rate. This is known as "dynamic DSC", since the heat transfer (energy) is evolving without a necessary thermodynamic equilibrium inside the analyzed sample. However, DSC measurements with a fast and dynamic process and occurrence of phase change phenomena can be affected by this lack of thermodynamic equilibrium, and hence can provide non-realistic enthalpy temperature data *h (T).* The shape of the latter can be largely affected while the melting point may be systematically shifted towards higher values for the heating cycles, or lower crystallization temperatures for the cooling process.

This will result in significant errors in the temperature-dependent measurements, such that the heat supply/release, referred to each temperature record, cannot be objectively attributed to the real TES values. For this reason, carrying out measurements with different heating rates and mass variations can provide good information about the influence of the measured variables, detects the needed thermal equilibrium status of the material, and verifies the soundness of the measured data.

From a practical point of view and to avoid the above-mentioned complications, the heating (or cooling) rate must be low enough to allow the sample to be measured close to the various isothermal states and with reasonable accuracy. The procedure described in the IEA standard [40] gives some direction in this sense and it was used to control/solve heat rate issues. This was done by changing the heating rate slowly from 10.0 K/min (high rate) to 0.125 K/min (low rate), or even lower, until the temperature difference between two inflection points of consecutive enthalpy curves (i.e., the peaks of the corresponding c_p-T curves), is lower than a predefined threshold (normally fixed by the standard to 0.2 K). Thus, the maximum permissible heating rate will be the minimum heating rate of two consecutive heating curves which comply with the above criterion [40]. A heating rate of 10 K/min was adopted for the measurements in the sensible range following the DIN 51007 [39]. In these measurement conditions, large quantity samples were tested to achieve a proper signal from the device.

The enthalpy change (at both sensible and latent stage), *dH(T),* of a sample, can be evaluated by integrating the heat flow registered during the DSC measurements. It can be assumed that a small variation of enthalpy *dH* (or the specific one, *dh*) is equal to a small amount of heat *dQ* (or the specific one, *dq*) added/released

[42,43]. This is valid for those processes characterized at constant pressure, as it happens during DSC experiments.

Therefore, it can be written that:

$$dH = dQ \qquad m^{sp}dh = m^{sp}dq \tag{1}$$

being

$$dq = c_p^{sp} \cdot dT \tag{2}$$

where m^{sp} is the sample mass, chosen as small as possible to comply with the instrument-specific requirements and to reach the state of equilibrium more quickly [39]. However, m^{sp} should be large enough to guarantee the representativity of the material sample. Furthermore, dT represents a small variation of temperature, and $c_p^{sp}(T)$ the specific heat capacity. Based on the recorded heat flow (DSC signal), the specific heat capacity of the sample $c_p^{sp}(T)$ can be easily determined from Equation (2), as follows

$$c_p^{sp} = \frac{dq}{dT} \xrightarrow[\text{under finite } \Delta T]{} c_p^{sp} = \frac{\Delta q}{\Delta T} \tag{3}$$

while the enthalpy variations have been directly evaluated from Equation (1).

In general, changes in enthalpy (latent heat) or the specific heat capacity (sensible heat) of an examined sample are determined by recording the absorbed heat between two equilibrium states, assigned as baselines of the acquired measurement curves. It is worth highlighting that the baseline-construction due to the specific heat capacity, measurements outside its melting range, is determined by performing three measurements: 1) empty measurement, 2) calibration measurement, and 3) real sample measurement for each temperature range (more details are available in [39]). This is due to the correction of measurement results possible affected by asymmetries and to compensate device specific errors.

Stepwise DSC Method and Evaluation of TES Parameters

A stepwise method is used as an alternative for reducing the heating rate effect that is affecting the measurements of dynamic DSC tests. In the stepwise procedure, the net heat applied in a certain temperature interval, is the same as the amount considered in the dynamic DSC tests (see Figure 7 a, b).

However, the whole interval is sub-divided into small sub-steps. This will favor the accumulation time to reach the thermodynamic equilibrium, between each temperature step, and will improve the temperature resolution (indicated in Figure 7 b), which was assumed to be 1 K in this study [44]. In this procedure, isothermal (equilibrium) states are always awaited between two subsequent temperature steps (i.e., 1 K).

The waiting needed to reach this state of equilibrium mainly depends on the selected (temperature) step and can only be determined empirically. In this work, the waiting times were taken 10 min at the beginning of the melting and 20 min by reaching the melting peaks. More details are described in Section 4.

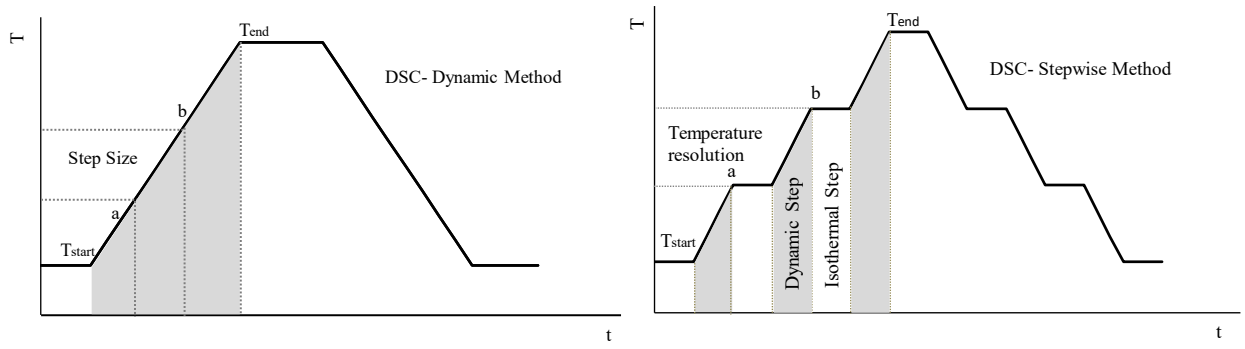

(a) (b)

Figure 7. T(t) program for (a) dynamic DSC method and (b) stepwise DSC method.

The total specific heat, supplied over the individual intervals, is obtained by summarizing the heat increments supplied at each sub-step $\Delta q^{\text{stepwise}}$. Thus, the experimental approach used in the stepwise method to analyze the *h(T)* response of the materials, along with the melting peak temperature T_m, follows the same relationships as proposed for the dynamic DSC test:

$$\Delta H = m^{sp} \Delta h = m^{sp} \Delta q^{\text{stepwise}} \tag{4}$$

2.1.2.4 Experimental Program

For the measurement of each parameter pair (c_p, h) three samples per material (paraffin-based RT24, RT25, RT26 and bio-based PureTemp25, as shown in Figure 8) were considered. Table 2 reports an overview of the full experimental program considered for the dynamic and stepwise method, respectively. The table gives information regarding the considered heating/cooling rates (in both dynamic and stepwise methods), which range from 10 K/min to 5 K/min, 2 K/min, 1 K/min, 0.5 K/min, 0.25 K/min, and 0.125 K/min. Furthermore, the investigated parameters, considered masses and test type of DSC method are also highlighted in the table.

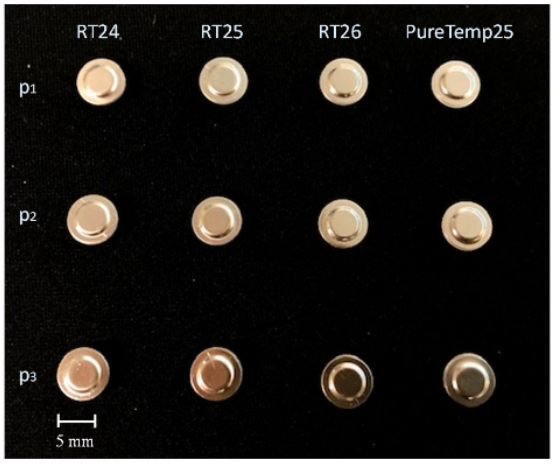

Figure 8. DSC specimens for the measurement of specific heat capacity and enthalpy of Phase Change Materials (PCMs) following the dynamic and stepwise procedures.

Table 2. Samples, heating rates, investigated parameters and DSC test-type applied in this study.

Tests	Materials (mass values in mg)													
	RT24			RT25				RT26			PureTemp25			
	P1	P3	P3	P1	P2	P3	P4	P1	P2	P3	P1	P2	P3	P4
Dynamic Heat Rate (R) (R: 10, 5, 2, 1, 0.5, 0.25, 0.125 K/min)	✓ 18.8	-	-	✓ 17.2	-	-	-	✓ 17.7	-	-	✓ 18.9	-	-	-
Dynamic Sample Mass (R: 0.125, 0.25 K/min)	-	-	-	✓ 16.3	✓ 18.4	✓ 18	✓ 7.9	-	-	-	✓ 18.9	✓ 19	✓ 17.7	✓ 10.1
Dynamic h (T) (R: 0.125 K/min)	✓ 13.3	✓ 16.5	✓ 16.9	✓ 16.3	✓ 18.4	✓ 18	-	✓ 17.7	✓ 18.5	✓ 16.1	✓ 18.9	✓ 19	✓ 17.7	-
Dynamic C_p (T) (R: 10 K/min)	✓ 14.3	✓ 16	✓ 16.1	✓ 17.2	✓ 18.4	✓ 18	-	✓ 16.4	✓ 18.9	✓ 12.4	✓ 10.5	✓ 18.9	✓ 18	-
Stepwise Heat Rate (R:2, 1, 0.5, 0.25, 0.125 K/min)	-	-	-	✓ 16.3	-	-	-	-	-	-	✓ 18.9	-	-	-
Stepwise - h (T) (R: VAR)	-	-	-	✓ 16.3	-	-	-	-	-	-	✓ 18.9	-	-	-

Abbreviations in table: R: heating Rate; h: enthalpy; $c_{p:}$ specific heat capacity; VAR: variable; RT: RubiTherm.

2.1.3 Dynamic DSC Results

2.1.3.1 Heating Rate Effect

Dynamic DSC tests were performed for all PCMs (3 paraffin-based and 1 bio-based), considering several heating rates (ranging from 10 K/min to 0.125 K/min) and various masses. The effect of the heating rate, between 10 °C to 50 °C, was investigated for only one of the samples per each PCM type (labelled as P1 in Table 2 of either RT24, -25, -26 or PureTemp 25).

Figures 8–11 show the resulting $c_p(T)$ and $h(T)$ (latent-only) curves of the samples abovementioned. It can be observed that the melting temperature T_m, defined as the temperature at which the maximum peak of the $c_p(T)$ curve is registered, of all four samples mainly depends on the heating rate. T_m is shifting progressively to lower values with decreasing heating rates. When comparing the different DSC measurements of each sample, the influence of the heating rate on the curves becomes clearly visible. It may be worth mentioning that even the $c_p(T)$ and $h(T)$ (latent-only) curves are largely influenced by the rate of heating during the melting transition, the related measured total specific latent heat (enthalpy) is independent on the heating rate.

From the experimental results (Figures 8–11) it can be also observed that the acceptable heating rate to be selected in order to stay below the defined threshold value of 0.2 K (i.e., the difference between a high and successive smaller heating rate, as proposed by the IEA standard [40] and described in Section 2.3.1), must be 0.125 K/min (or lower) for RT25 and PureTemp 25, and 0.250 K/min (or lower) for RT24 and RT26. This would reduce as much as possible the heating rate issues for the considered PCMs.

The c_p curves of RT24, -25 and -26 with different heating rates contain mainly two (local) peaks, at different temperatures. These double-peak curves become more pronounced for lower heating rates. The first local one, as for each curve and considering 0.125 K/min, was registered at 6.2 °C for RT24 (Figure 9), at 17.6 °C for RT25 (Figure 10) and 17.4 °C for RT26 (Figure 11).

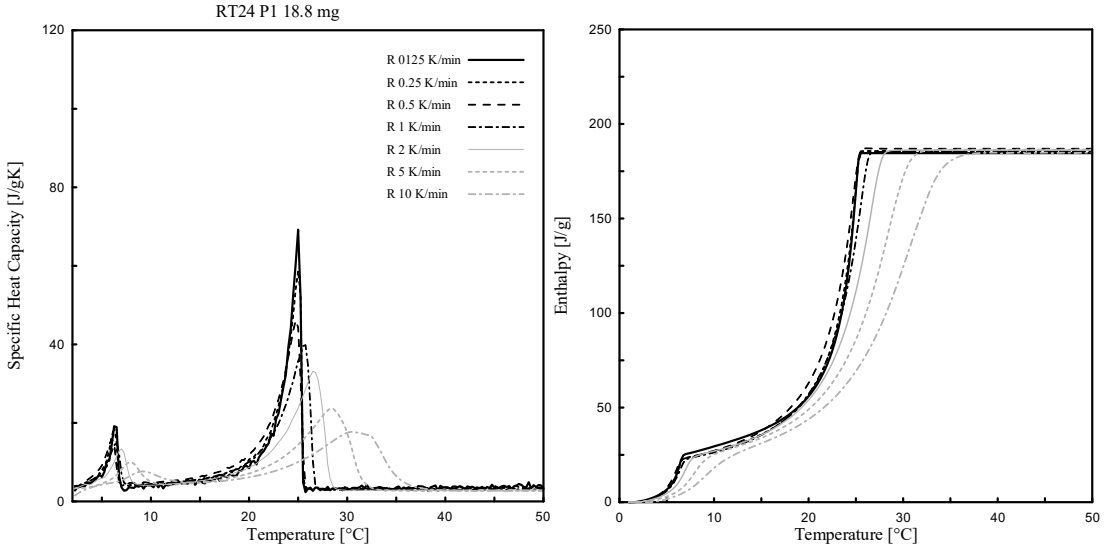

(a) (b)

Figure 9. Dynamic DSC measurements: (a) $c_p(T)$ and (b) $h(T)$ curves (latent only) with different heating rates for RT24.

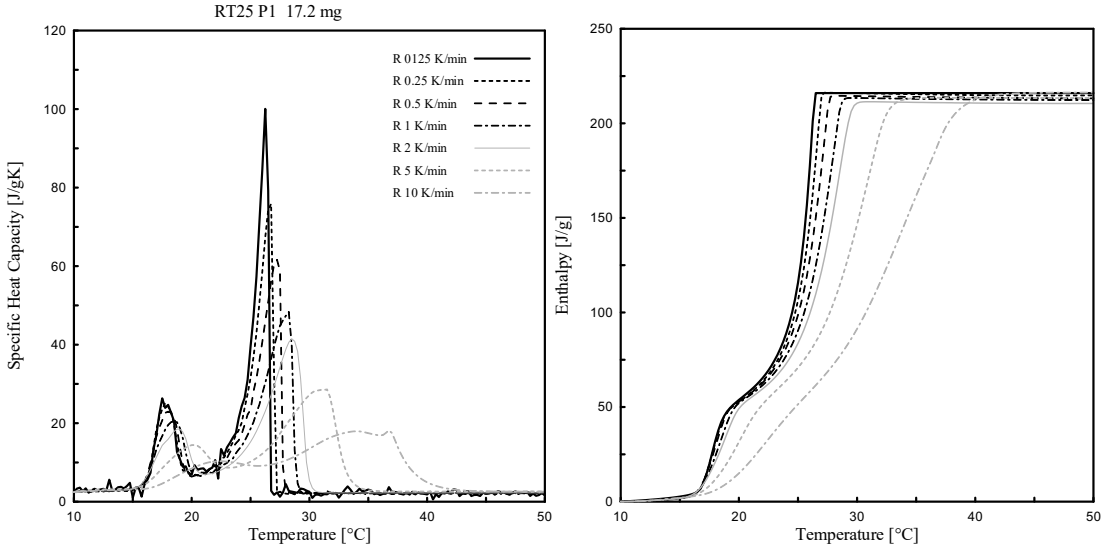

(a) (b)

Figure 10. Dynamic DSC measurements: (a) cp (T) and (b) h(T) curves (latent only) with different heating rates for RT25.

The second local (and maximum) peak, which is representing the melting of paraffin, while adopting a heating rate of 0.125 K/min, was achieved at 25.0 °C for RT24 (Figure 9), at 26.5 °C for RT25 (Figure 10) and 26.2 °C for RT26 (Figure 11). Similar behavior can be observed from the c_p- and h-T (latent-only) DSC

curves of the bio-based PureTemp25. From the DSC tests, two adjacent peaks appear in the c_p-T curves. The first melting temperature of the highest peak was measured at 24.6 °C (Figure 12), while the second local (not maximum) peak was registered at a higher temperature of 26.2 °C. The actual melting peak temperature of 24.6 °C was close to the declared value in the datasheet, which is 25 °C (Table 1). The presence of a local (not maximum) peak, that was detected for both PCM types, could be the result of either a mixture of different compounds, having different chain lengths, or a possible occurrence of solid–solid latent phase transitions prior the melting.

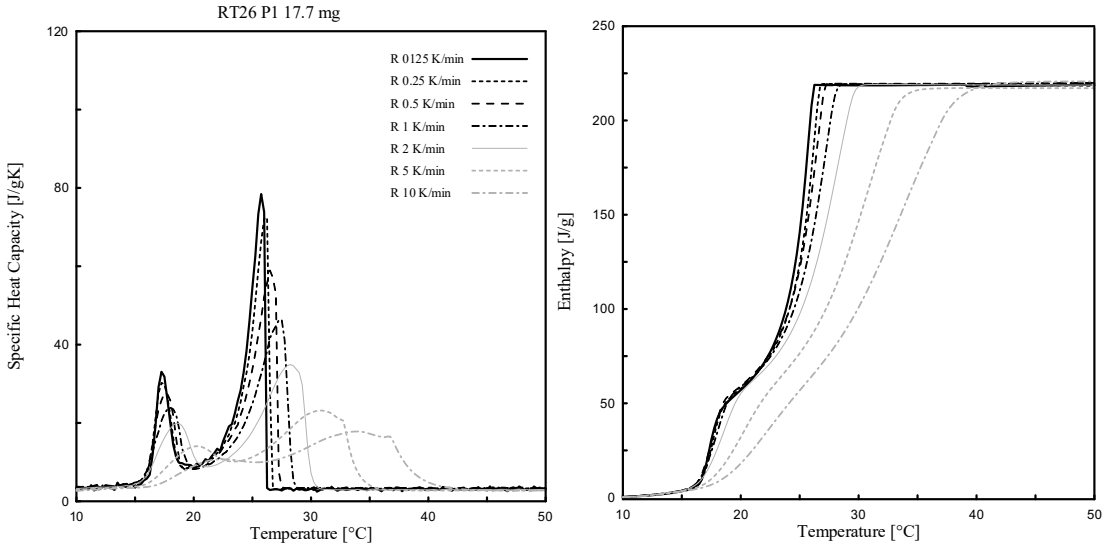

(a) (b)

Figure 11. Dynamic DSC measurements: (a) $c_p(T)$ and (b) $h(T)$ curves (latent only) with different heating rates for RT26.

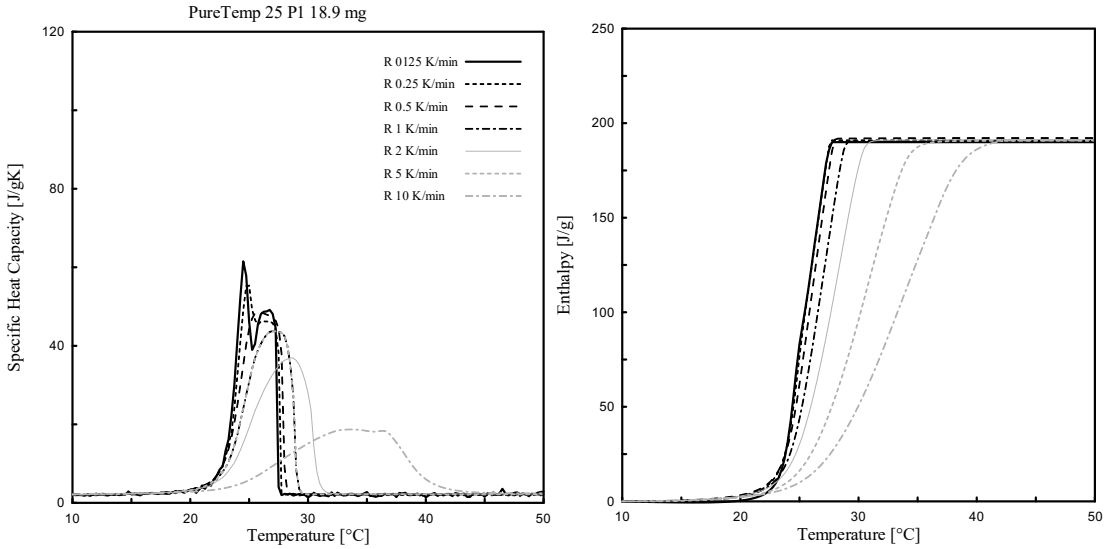

(a) (b)

Figure 12. Dynamic DSC measurements: (a) $c_p(T)$ and (b) $h(T)$ curves (latent only) with different heating rates for PureTemp25.

These results also show that the declared melting temperatures in the datasheets (Table 1) are lower than the ones measured with the dynamic DSC tests. This was expected, since measuring the exact melting peak temperature requires a heating rate that should be as low as possible, meaning theoretically nearly 0 K/min. In practice, this is not feasible, since extremely low heating rates result in very weak signals and characterized by huge noise on the measured signal and implicitly limits the choice of the lowest possible heating rate to be assigned.

2.1.3.2 Mass of Sample Effect for RT25 and PureTemp 25

The effect of the sample mass in the dynamic DSC experiments is discussed in this subsection. Paraffin-based RT25 and bio-based PureTemp 25 were considered for this aim and two masses per each PCM were investigated. Tests were performed considering different heating rates (again ranging from 10 K/min to 0.125 K/min), with temperatures raising between 10 °C and 50 °C; 7.9 mg and 16.3 mg samples were tested for RT25, while 10.1 mg and 18.9 mg for the PureTemp 25.

Figure 13 shows the comparative evolution of the melting peak temperatures, T_m, against the different heating rates by considering the two masses (low mass 7.9 mg and high mass 16.3 mg, respectively). It can be observed that the measured melting points, through the DSC tests for the small sample mass (7.9 mg), rather quickly approximates the melting peak temperature (i.e., 26.0 °C of the lowest heating rate 0.125 K/min). Hence, T_m was 26.50 °C at 0.50 K/min and 26.25 °C at 0.25 K/min. Contrarily, the sample with the higher mass (16.3 mg) showed more influence of the heating rate: i.e., T_m = 27.25 °C at 0.50 K/min, 26.75 °C at 0.25 K/min and 26.25 °C at 0.125 K/min.

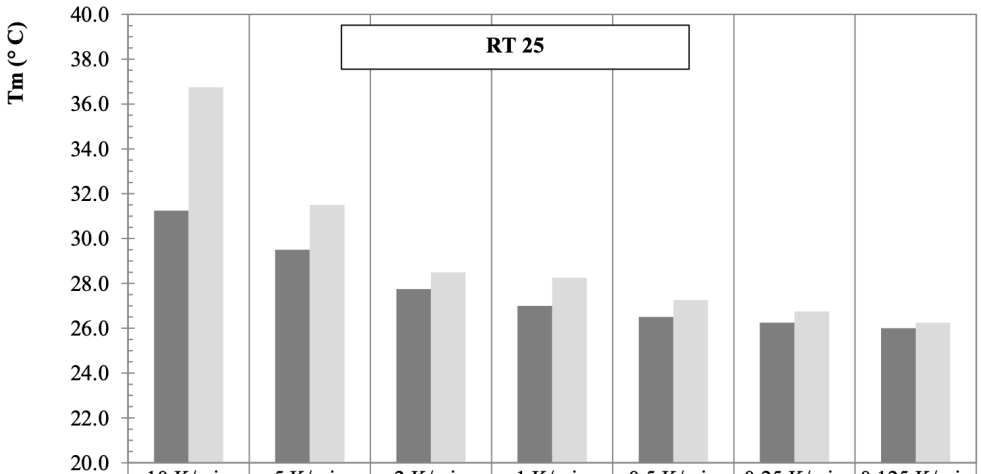

	10 K/min	5 K/min	2 K/min	1 K/min	0.5 K/min	0.25 K/min	0.125 K/min
7.9 mg	31.25	29.50	27.75	27.00	26.50	26.25	26.00
16.3 mg	36.75	31.50	28.50	28.25	27.25	26.75	26.25

Figure 13. Melting peak temperature T_m for dynamic DSC measurements with several heating rates and 2 different masses for RT25.

Also, for PureTemp 25 the comparison of melting peak temperatures, T_m, against the various heating rates and two different masses (10.1 mg and 18.9 mg, respectively) is presented in Figure 14. As for RT25, the

sample with the lower mass (10.1 mg) showed a less influence of the heating rate on the melting peak temperature (e.g., T_m = 24.50 °C at 0.25 K/min and 24.25 °C at 0.125 K/min). For the higher mass (18.9 mg) this was, T_m = 25.00 °C and 24.50 °C, at 0.25 K/min and 0.125 K/min, respectively.

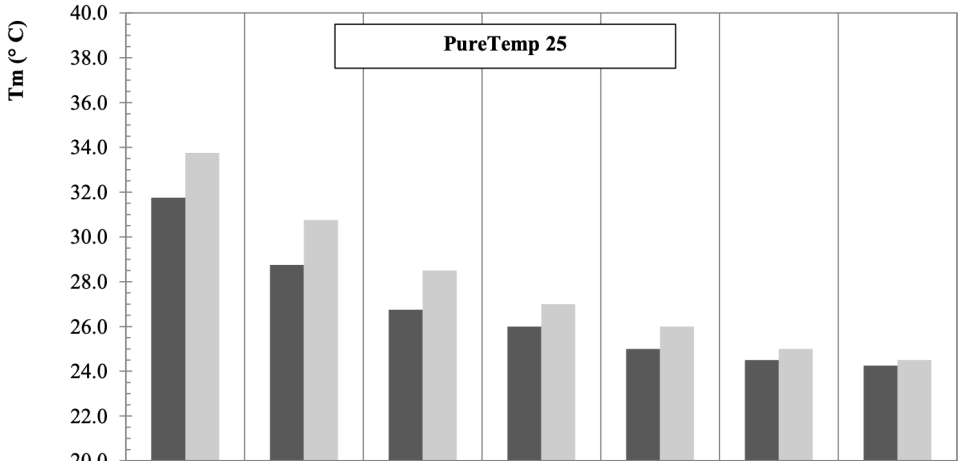

	10 K/min	5 K/min	2 K/min	1 K/min	0.5 K/min	0.25 K/min	0.125 K/min
10.1 mg	31.75	28.75	26.75	26.00	25.00	24.50	24.25
18.9 mg	33.75	30.75	28.50	27.00	26.00	25.00	24.50

Figure 14. Melting peak temperature T_m of dynamic DSC measurements with several heating rates and 2 different masses for PureTemp25.

It should be noted that all curves, which were obtained from measurements with heating rates less than 0.125 K/min, had high fluctuations due to signal noises, which make the evaluation of the data and baseline construction difficult to build up. For this reason, a heating rate of 0.125 K/min was considered as the lowest possible choice at which the instrument could still detect signals that were easy to be analyzed. Moreover, 0.125 K/min, for all tests, provides a proper accuracy to fulfill the IEA standard requirements [40], see Section 2.3.1.

The results in this section showed that the selection of the "heating rate" and "sample mass" arises mainly from a compromise between accuracy of the measurements (enthalpy, specific heat capacities and melting peak values) and mitigation of the data due to heating rate effects. Besides the effect of instrument precision and adopted parameters, the measurement accuracy also depends on the representativeness of the sample, which also requires the analysis of larger masses. However, higher mass samples need a strong reduction of the heating rate for achieving a proper thermal equilibrium and valid TES analysis. From the practical point of view, very low heating rates go along with huge signal noises. Contrarily, in low mass samples, thermal equilibrium can be reached more easily with higher heating rates. Experimentally, the most representative mass should be found first, followed by choosing the proper "noiseless" heating rate.

2.1.3.3 Specific Heat Capacities, Enthalpy and Melting Points for Heating and Cooling

For each type of PCM, six samples were investigated through dynamic DSC tests under both heating and cooling. Three of them were used for $c_p(T)$ characterization, while the remaining three for $h(T)$. Before and

after the non-isothermal phase change (either melting or crystallization), a heating/cooling rate of 10 K/min was adopted for all tests to minimize noise ratios in the signal [39]. In the latent stage, the considered heating/cooling rates were of 0.250 K/min for RT24 and RT26 and 0.125 K/min for RT25 and PureTemp 25. These assumptions were done following the IEA standard procedure [40] to mitigate the influence of the heating/cooling rate for each compound, as discussed in previous Section 3.1.

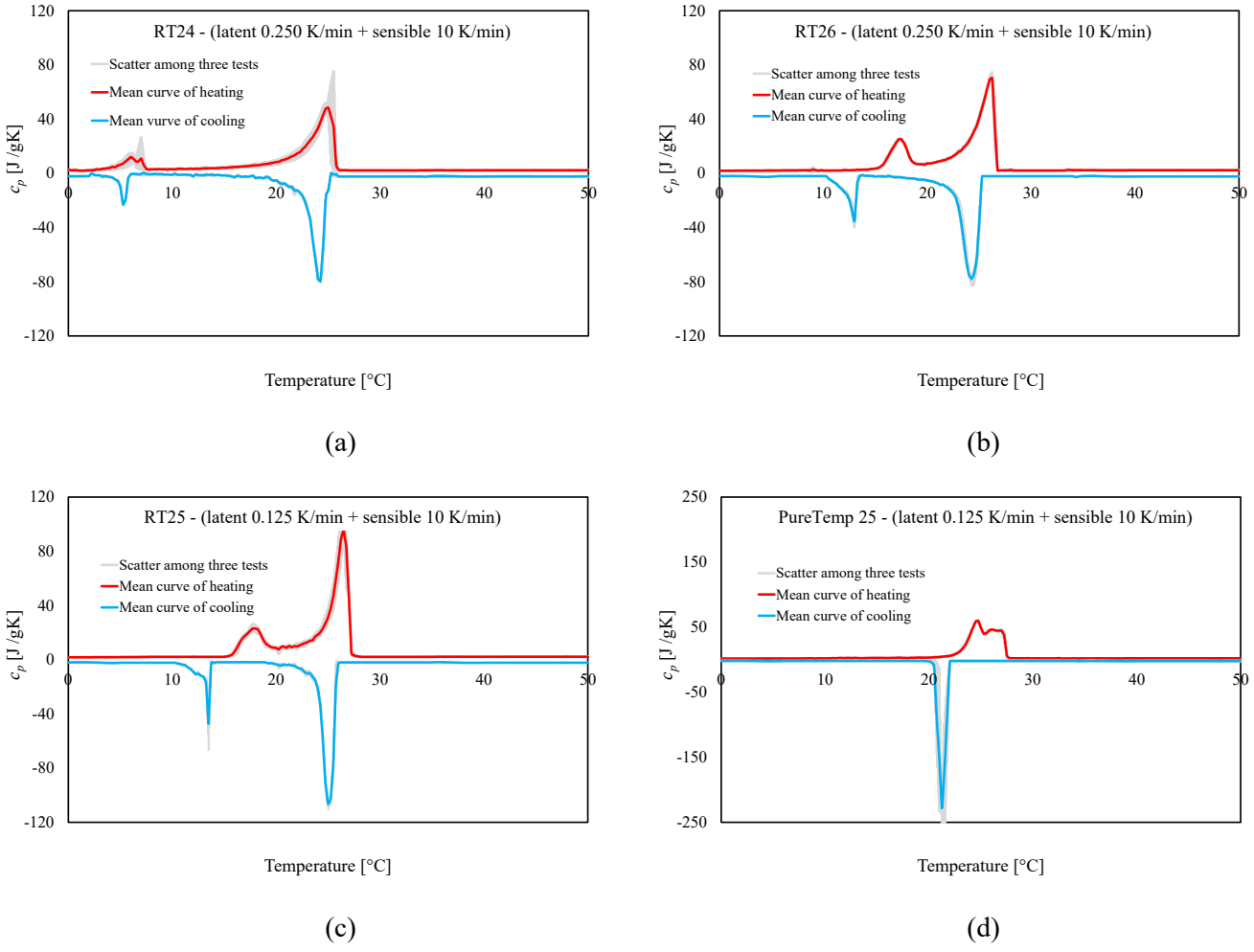

Figure 15. Specific heat capacities following the dynamic DSC tests (for heating between 0 °C and 50 °C and cooling between 50 °C and 0 °C): (a) RT24, (b) RT26, (c) RT25 and (d) PureTemp 25. Note: the total specific heat capacities have been constructed by additively linking the sensible parts with the latent ones.

Figure 15 shows the results of dynamic DSC measurements done for the paraffin waxes (RT24, RT25, RT26) and the biobased PCM (PureTemp 25), for determining the c_p $[J/g \times K]$ versus T [°C] response, in both latent and sensible ranges. All DSC curves are characterized by an almost sensible behavior in the temperature range far from the melting and crystallization points (i.e., in the solid range −20 °C to 10 °C and the liquid range 30 °C to 60 °C), while a non-isothermal latent behavior appears in the phase change region (either with solid-to-liquid and liquid-to-solid responses). It can be also observed that the results show very little (almost negligible) deviation, for all tests, as indicated by the gray area. In the liquid-sensible ranges (i.e., between

30 and 60 °C), the determined specific heat capacities varied between 2.1 and 2.3 J/g × K (for both heating/cooling), for all samples RT24, RT25, RT26 and PureTemp 25. Then, in the lower temperature ranges (solid-sensible responses, between −20 and 10 °C), the c_p values varied between 1.7 and 2.0 J/g×K (for both heating/cooling), for RT24, RT25, RT26 and PureTemp 25. In the latent responses, pronounced peaks developed that represent the solid–liquid and liquid–solid phase changes of the various PCMs.

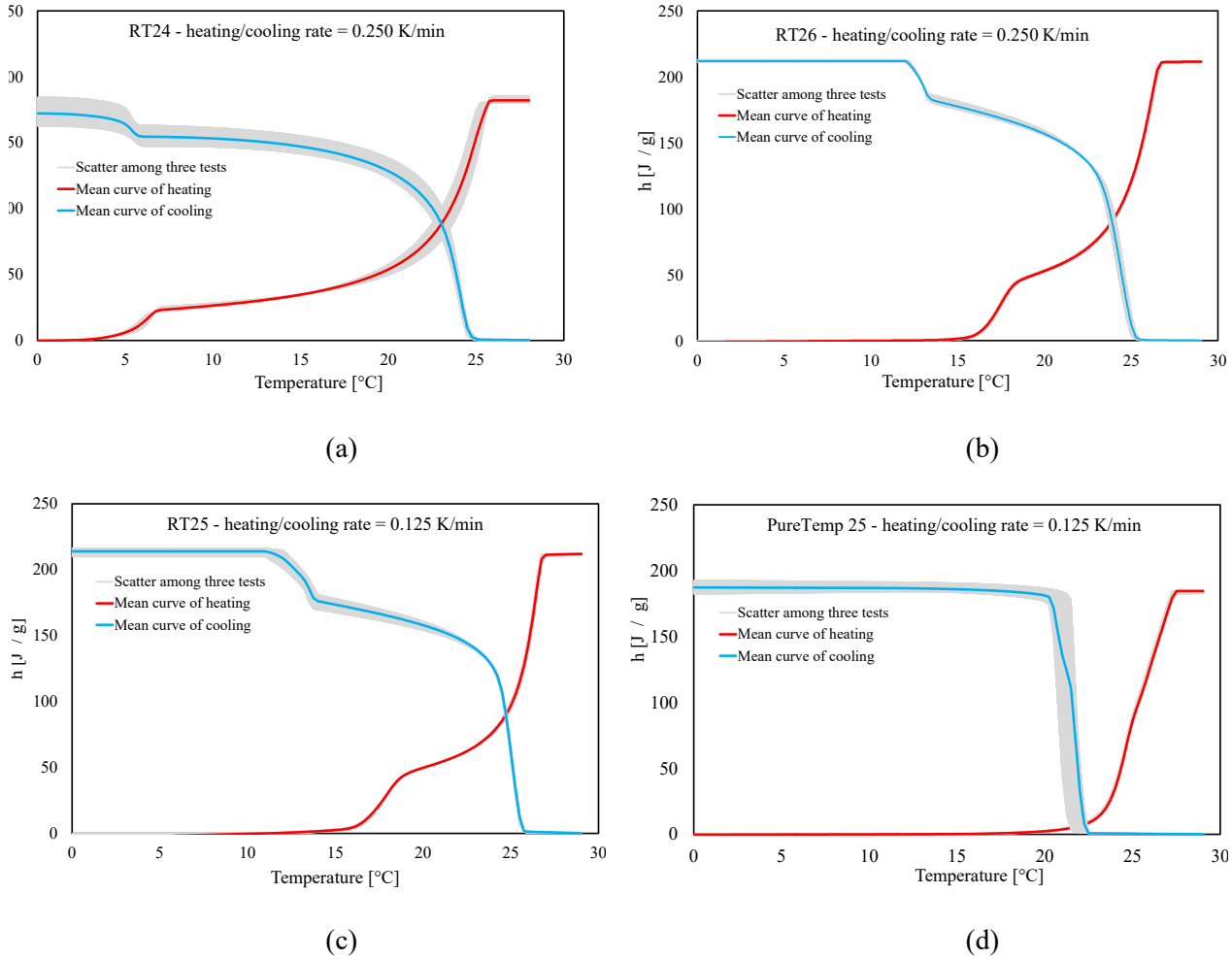

Figure 16. Enthalpy (latent-only) measurements (heating and cooling) following the dynamic DSC tests: (a) RT24, (b) RT26, (c) RT25 and (d) PureTemp 25.

In Figure 16, the resulting enthalpy curves (latent part only), measured with the dynamic DSC method, are shown for all materials. The plotted curves represent the mean values of the measurements done for three samples, over three cycles. These data mainly represent the absorbed/released thermal energies for heating and cooling, respectively, and the unitary latent heat during a phase change. The measured total and specific *h* of each material is shown in Figure 17. It can be observed that the absorbed heat from 0 J/g to the total specific latent heat of each PCM (i.e., 182.1 J/g for RT24, 193.3 J/g for RT25, 211.9 J/g for RT26 and 186.1 J/g for PureTemp 25) is represented by a clear non-isothermal behavior. Similar trends, in a releasing way, from the maximum values of *h(T)* (i.e., form 178.8 J/g for RT24, 213.4 J/g for RT25, 211.4 J/g for RT26 and

186.8 J/g for PureTemp 25) to 0 J/g, can be observed for the cooling responses. From the data, it can be observed that the biobased PureTemp 25, compared to the RT ones, is characterized by a faster acceleration of the *h(T)* response. This means that the phase change occurs in a narrower melting or crystallization range, which is often more appreciated in practical passive applications for buildings.

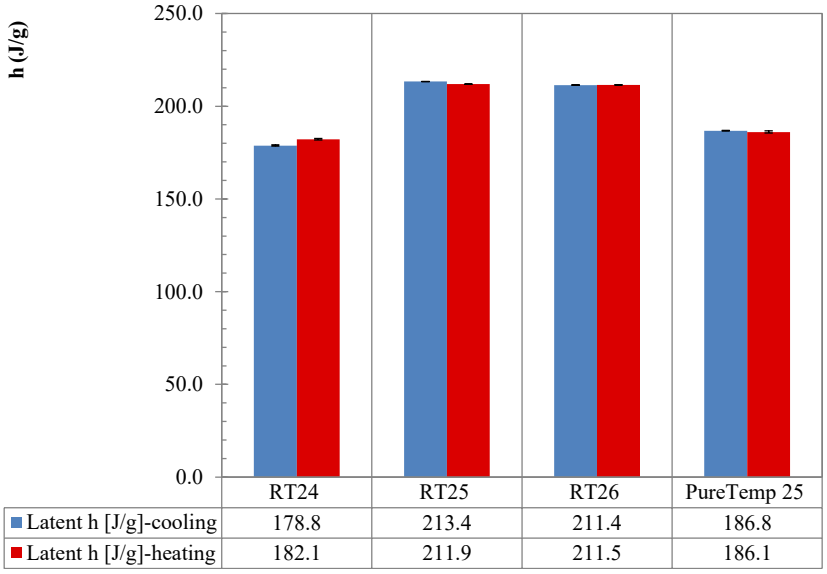

	RT24	RT25	RT26	PureTemp 25
Latent h [J/g]-cooling	178.8	213.4	211.4	186.8
Latent h [J/g]-heating	182.1	211.9	211.5	186.1

Figure 17. Latent absorbed/released h [J/g] during melting/crystallization following the dynamic DSC method.

Finally, the maximum peak temperatures (meaning those points at which the maximum c_p was registered) for either melting or crystallization of all PCMs are compared in Figure 18.

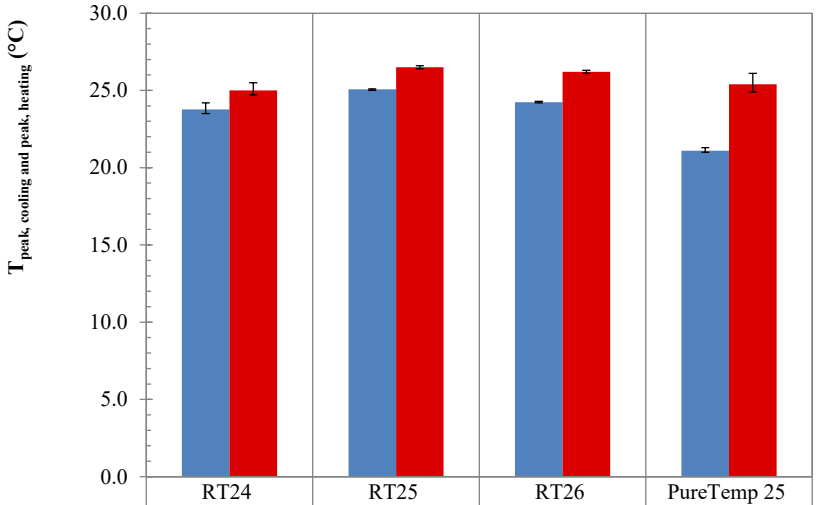

	RT24	RT25	RT26	PureTemp 25
Peak-cooling	23.8	25.1	24.2	21.1
Peak-heating	25.0	26.5	26.2	25.4

Figure 18. Comparison of the maximum peak temperatures (°C) of all samples in the melting/crystallization range.

The graphs further show the “melting” and “crystallization” temperatures of the three specimens, their mean values, and the statistical deviation via error bars. The peak temperature (mean value of three specimens) at which melting happened were detected at 25.0, 26.5, 26.2 and 25.4 °C for RT24, RT25, RT26 and PureTemp

25, respectively. Similarly for the crystallization measurements (again mean value of three specimens), peak temperatures were registered at 23.8, 25.1, 24.2 and 21.1 °C for RT24, RT25, RT26 and PureTemp 25, respectively.

In Figure 18 it can also be seen that there is an obvious difference between the cooling and heating peak temperature. Overheating or subcooling effects [18], occurred due to a kinetic delay in phase transformation, could be a possible explanation for the shifted heating/cooling peaks. Upon the attained results, the subcooling is lower in paraffins, also known as alkanes (about 1.2–2 K), compared to the PureTemp 25 (made of fatty acids) with about 4.3 K subcooling. These phenomena occur even if the amount of stored/released heat stayed almost the same (see Figure 17).

Table 3. Comparison of extrapolated peak initial temperatures (assigned to the transformation temperature) of all samples in the melting/crystallization range according to DIN 51007 [39].

PCM type	**RT24** R 0.250 K/min		**RT25** 0.125 K/min		**RT26** 0.250 K/min		**PureTemp25** 0.125 K/min	
	$T_{onset,\ heatir}$	$T_{onset,\ coolir}$	$T_{onset,\ heatir}$	$T_{onset,\ coolir}$	$T_{onset,\ heatir}$	$T_{onset,\ coolir}$	$T_{onset,\ heatir}$	$T_{onset,\ coolir}$
$P_{1,2,3}$	3.0	24.3	15.5	25.7	15.6	25.1	23.0	21.9

Finally, the $T_{onset,heating}$ and $T_{onset,cooling}$ are reported in Table 3 They are representing the extrapolated peak start temperature (defined $T_{p,ini,e}$ as sample transformation temperature by DIN 51007:2019 [39]). These temperature values represent the intersection point of the extrapolated start baseline with the tangent (or a straight) line through the linearly rising or falling part of the endothermic or exothermic peak. The onset temperatures are worth knowing since at this point the lower surface area of the sample (crucible bottom) begins to change phase, as this temperature can be determined sufficiently reproducible and is almost independent of the heating rate. All other temperatures largely depend on test conditions, masses and heating/cooling rates (as shown in Figures 8–11).

2.1.4 Stepwise DSC Results

2.1.4.1 Heating Rate Effect

Tests with different heating rates (ranging from 2 K/min to 0.125 K/min) have also been performed for the stepwise DSC method. These activities were scheduled for RT25 and PureTemp 25 under temperatures ranging between 10 and 30 °C (a range which is relevant for the phase transition).

Figure 19 a and Figure 20 a show the stored heat, per each temperature interval (being 1 K, representing the difference between two isothermal temperature increments), while the accumulated specific enthalpy (latent part only) is shown in Figure 19 b and Figure 20 b. These results represent the determined partial enthalpies and the cumulated ones between 10 °C and 30 °C from the measurements done for RT25 and PureTemp 25. It is shown in Figures 18 and 19 that all the results, having different heating rates, are completely overlapping. Particularly, the Δq-T and h-T (dotted) curves obtained by considering different heating rates, i.e., 2, 1, 0.5,

0.25 and 0.125 K/min, show almost the same values, with a very small difference in terms of either Δq *or* h values.

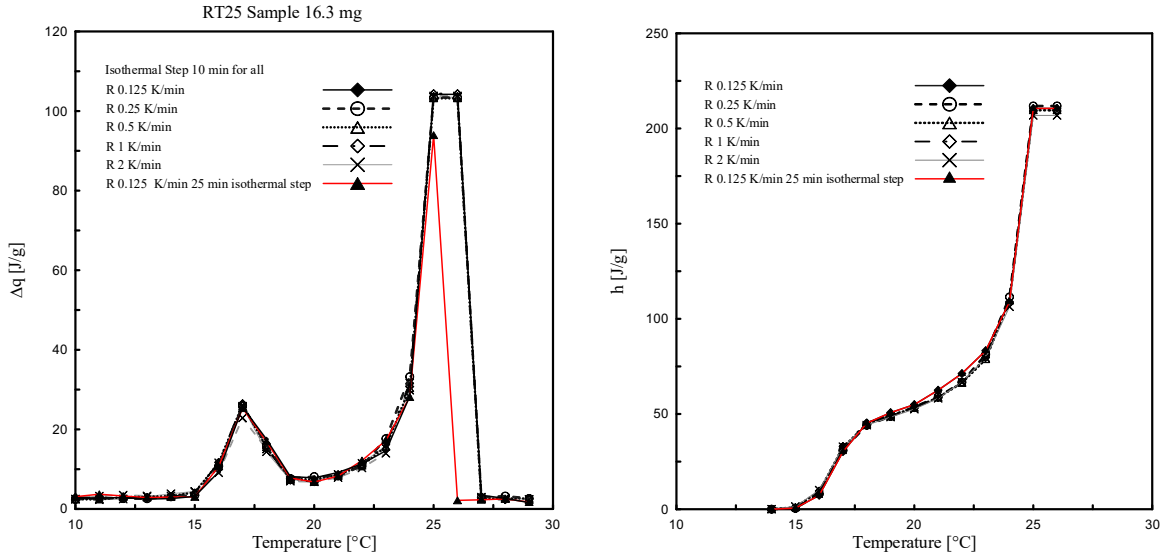

(a) (b)

Figure 19. (a) $\Delta q\ (T)$ and (b) $h(T)$ curves determined through stepwise DSC and considering different heating rates for RT25.

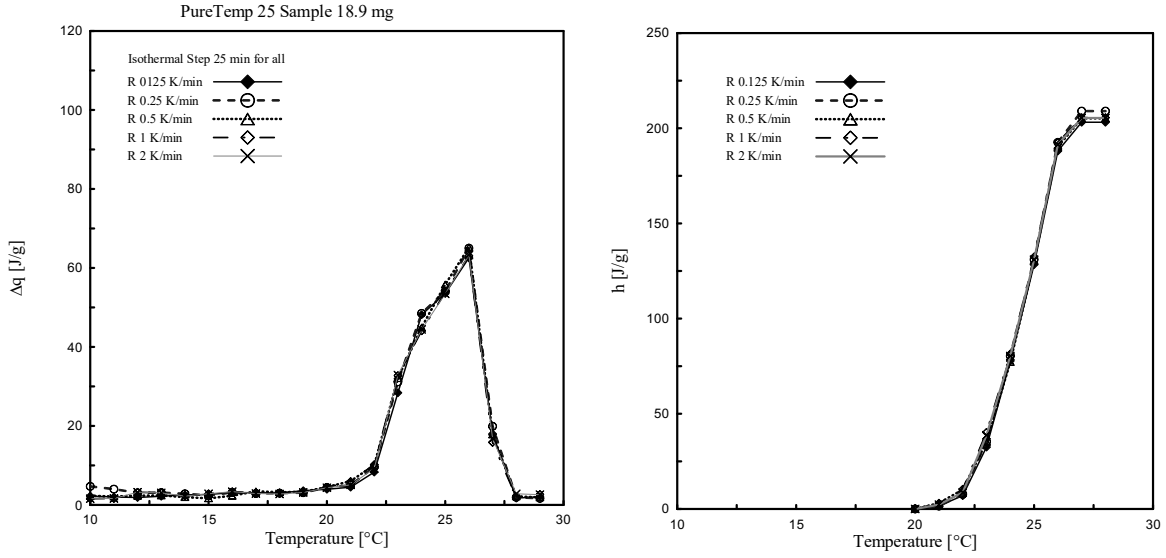

(a) (b)

Figure 20. (a) $\Delta q\ (T)$ and (b) $h(T)$ curves determined through stepwise DSC and considering different heating rates for RT25.

The enthalpy deviation between the different heating curves has a maximum of 5 J/g, and this occurred mainly close to the melting range. This difference is less than 3% of the total and specific heat absorbed in the considered temperature range. This means that with the stepwise method the influence of the heating rate,

which classically affects dynamic DSC measurements, can be neglected. (See section 3.1 where the results were obtained through dynamic DSC measurements).

It may be worth mentioning that the length of the relaxation time (namely, isothermal step) is an important parameter for the temperature resolution of the accumulated heat, especially in the temperature ranges close to the melting peak (defined as the point in which the maximum amount of stored heat can be measured). Particularly, to reach thermal equilibrium in these zones a longer isothermal step is required. This can be observed in Figure 19 a where the highest peak (readable in the ranges 25 °C and 26 °C) for all tests is obtained for heating rates of 2, 1, 0.5, 0.25 and 0.125 K/min, while performed with an isothermal step of 10 min. To evaluate the sensitivity of the results regarding the duration of the applied isothermal step, an additional measurement was conducted for a heating rate of 0.125 K/min and where the isothermal step was increased from 10 min to 25 min with the aim to reach proper thermodynamic equilibrium during the phase change transition (see the red curve in Figure 19). The results clearly show the influence of this increased isothermal step.

2.1.4.2 Enthalpy and Phase Change Temperature

The enthalpy measurements, i.e., the absorbed specific heat along the considered temperature steps, and phase change temperatures obtained by an adopting isothermal step time of 25 min and various heating rates, are reported in this subsection. Both sensible and latent absorbed heat, in the range of 10 °C and 30 °C, are evaluated.

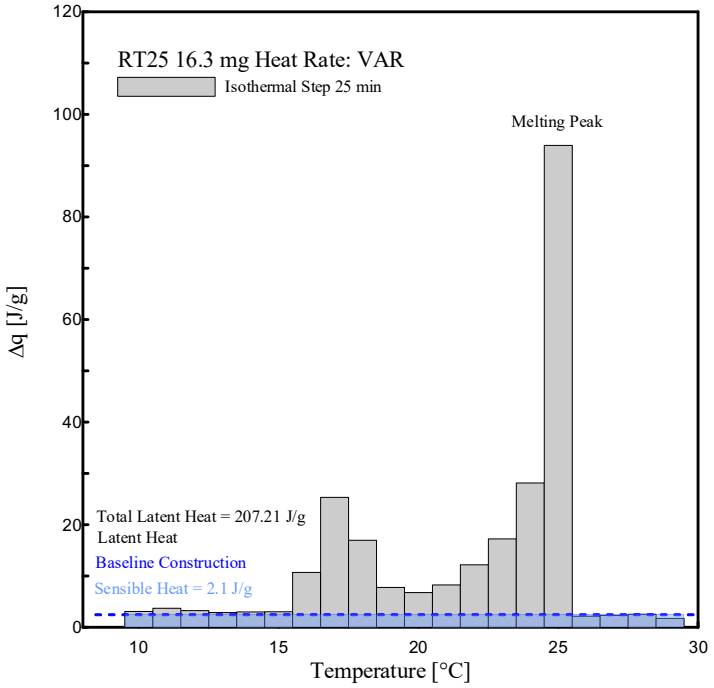

Figure 21. Histogram view of stored heat $\Delta q\ (T)$ for RT25, at several temperature intervals and adopting an isothermal time step of 25 min.

Figure 21 and Figure 22 show a histogram of the stored heat, $\Delta q\ (T)$, between the temperature intervals, representing the temperature resolution of the acquired data, of 1 K, for the tests. The corresponding tabular

data is provided in Table 4. From the results, the melting of RT25 mainly starts at 15 °C and ceases at 26 °C. A baseline construction was used to evaluate and separate the sensible part form the latent one. The sensible absorbed heat was evaluated at 2.10 J/g, which agreed with the value declared in the datasheet, i.e., 2 J/g, (see Table 1).

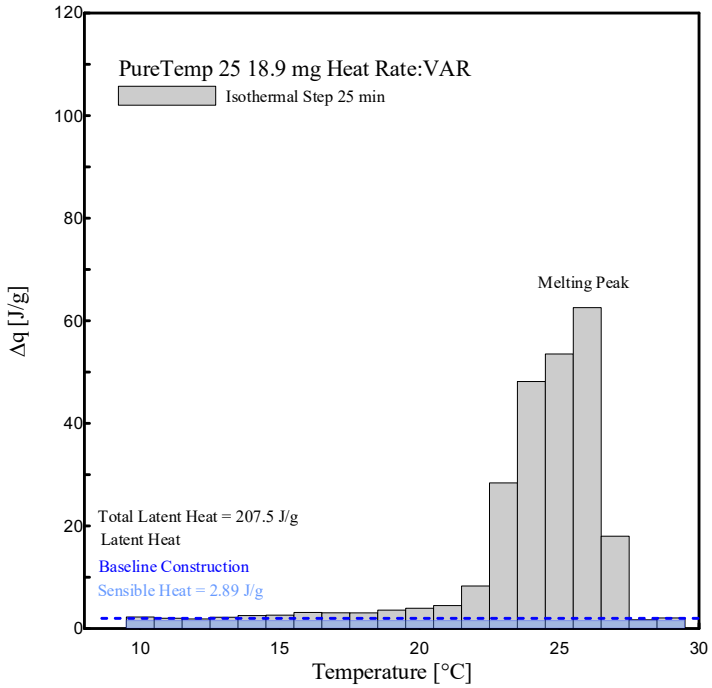

Figure 22. Histogram view of stored heat $\Delta q\ (T)$ for PureTemp 25, at several temperature intervals and adopting an isothermal time step of 25 min.

The melting peak temperature as indicated in Figure 21 can be appreciated in the range of 25–26 °C. The (latent) melting of the PureTemp 25 takes place in a smaller temperature interval (from 21 °C to 28 °C, see Figure 22). The absorbed sensible heat of PureTemp 25 was evaluated to 2.89 J/g while its melting point falls in the range of 25–26 °C.

The phase transition enthalpy (considering the latent part only), in the defined melting range of 15 °C to 26 °C and constructing the baseline at 15 °C, was 207.21 J/g for RT25 (see Table 4). This value is slightly different to the one measured through the dynamic DSC measurements (211.9 J/g reported in Figure 17). The total latent heat of PureTemp 25, evaluated in the temperature range between 21 °C and 28 °C, is 207.5 J/g (see Table 4), which somehow deviates from the value measured using the dynamic DSC method (186.1 J/g, showed in the Figure 17).

However, it may be worth mentioning that the results obtained from dynamic DSC tests, or the stepwise methods are highly depending on the baseline construction, which separates the sensible heat from the latent part. As the baseline-construction can be done more precisely for the dynamic DSC method rather than for the stepwise one, the results of the latent heat by using both the methods might be significantly affected.

From the results it can be stated that the stepwise DSC method is capable of cleaning and eliminating the heating rate effects, which is classically of interest for dynamic DSC measurements. It is a more appropriate method that can capture the total enthalpy in the defined temperature range by applying predefined

temperature steps, and for validating the melting peak (range) more precisely than with dynamic DSC tests. However, some drawbacks are still characterizing the stepwise DSC method, which is mainly that the temperature resolution adopted in these approaches is still too high. The smaller the temperature steps, the better the temperature resolution. However, the measuring time could be considerably longer as the step sizes decrease. In general, the shape characterization of $c_p(T)$ curves can be achieved faster (and more properly) by using the dynamic DSC method than the stepwise one.

Table 4. Stored heat values (sensible = S, latent = L and total = S + L) of RT 25 and PureTemp 25, as shown in Figures 20 and 21.

Temp. Range [°C]	RT25 (Mass: 16.3 mg)		PureTemp25 (Mass: 18.9 mg)	
	Δq (total: S+L) [J/g]	Δq (L) [J/g]	Δq (total: S+L) [J/g]	Δq (L) [J/g]
15 to 16	3.03	0.93	-	-
16 to 17	10.70	8.60	-	-
17 to 18	25.33	23.23	-	-
18 to 19	16.96	14.86	-	-
19 to 20	7.77	5.67	-	-
20 to 21	6.77	4.67	-	-
21 to 22	8.26	6.16	4.48	1.59
22 to 23	12.18	10.08	8.30	5.41
23 to 24	17.23	15.13	28.39	25.50
24 to 25	28.13	26.03	48.16	45.27
25 to 26	93.95	91.85	53.53	50.64
26 to 27	-	-	62.56	59.67
27 to 28	-	-	22.32	19.43
	230.31	207.21	227.74	207.48

In summary, it can be observed that the temperature resolution for DSC tests depends on the amount of analyzed intervals, needed to measure the heat storage capacity, within the considered temperature range. Based on the chosen DSC method the “resolution” of the data, representing the heat supplied to the sample and the corresponding temperature range, can differ. In the stepwise method heating is applied in small intervals called “steps”. Thus, the resolution is equal to the height (or length) of the temperature steps, however it is required that the start and end of each step must be in an isothermal state. For dynamic DSC tests, the interval is continuously scanned by heating of the sample. There are no steps waiting for thermodynamic equilibrium. This means that the heating rate needs to be low enough to assure thermodynamic equilibrium within the entire sample. Theoretically, this will occur by employing a heating rate close to 0 K/min., which is practically not feasible. This means that the heat supplied to the sample, according to each data recording (equal to the enthalpy change), cannot be fully assigned to the measured temperature. Too high heating rates may cause significant errors (less “accuracy” of the results) in the data of the heat stored as a function of temperature. However, in DSC dynamic tests the resolution of the data itself is only restricted by the data recording system.

2.1.5 Conclusions

In this work, a detailed experimental program is reported for analyzing the Thermal Energy Storage (TES) capacity of three paraffin-based and one bio-based PCM, employable for construction and buildings applications. For this aim, the paraffin-based waxes, RT24, RT25 and RT26, and an eco-friendly bio-based PCM, PureTemp 25 were examined using DSC testing equipment. All selected PCMs have melting/ crystallization temperatures within the well-known comfort zone temperature for buildings, e.g., ranging between 19 and 26 °C. Heat storage capacities, melting/ crystallization responses, and enthalpies, under both sensible (solid and liquid) and latent TES responses, were investigated through DSC tests.

Two alternative methods were performed and compared, i.e., a dynamic DSC and a stepwise DSC method. Based on the results reported in this work, the following conclusions can be drawn:

- Dynamic DSC tests, performed for all 4 different PCMs and considering several heating rates (ranging from 10 K/min to 0.125 K/min), showed that the measurable melting peak temperatures T_m (indicated as that point at which the maximum peak of $c_p(T)$, or alternatively the inflection point of $h(T)$, can be registered), mainly depends on the heating rate. T_m can be shifted progressively to lower values as the heating rate decreases and vice versa.
- The $c_p(T)$ and $h(T)$ curves under dynamic DSC strongly depend on the selected heating rates. Only the related measure of the accumulated (total) specific (unitary) latent heat is independent to the heating rate. In general terms, the total achievable h is the same when different heating rates are assumed, even though the $h(T)$ curves and their slopes, $cp(T)$, are heating rate dependent.
- Dynamic DSC tests, performed by considering 2 different (low and high) sample masses, for RT25 and PureTemp 25, highlighted that the specimens with a lower mass are less affected by the heating rate. However, they suffer higher measurement noise and less representativity of the material under investigation.
- Dynamic DSC results of higher mass samples showed more stable measurements, especially in the sensible parts, and seemed to be more representative for the behavior of the investigated PCMs. However, they turned out to be more sensible to heating rate effects under latent heat storage.
- It can be concluded that the selection of the proper “heating rate” and “sample mass” (aimed at fulfilling the IEA requirements) arises from a compromise between accuracy of the measurements (i.e., enthalpy, specific heat capacities and melting point) and the mitigation of the heating/cooling rate effects.
- It can be stated that reliable and reproducible results can be achieved for characterizing the aforementioned (paraffin- and bio-based) PCMs by following the IEA standard procedure and adopting the dynamic DSC method.

- Results following the stepwise method demonstrated that both $\Delta q(T)$ and $h(T)$ results, obtained by considering several heating rates (2, 1, 0.5, 0.25 and 0.125 K/min), presented almost the same trend and similar values (with differences significantly less than 0.2 °C and/or in terms of enthalpy of max. 5 J/g between them). This means that with the stepwise method the heating rate influence, which classically affects the dynamic DSC, can be fully controlled.
- The main drawbacks of the stepwise method, however, are related to its enormously time-consuming character, imposed by the test procedure. The required length of the relaxation time (namely, isothermal step) is sometimes too high to achieve proper results, especially in the melting region.
- The temperature resolution of the stored heat is considerably higher, using the stepwise method, in comparison to the dynamic one. However, a maximum resolution of 1 K, as those employed in the stepwise method of this study, is not high enough to obtain the $c_p(T)$ curve of the material, which would require smaller discretized temperature steps, and does not allow describing the melting temperature of the material in a concise way.
- The results obtained following both dynamic and stepwise methods are dependent on the baseline construction, which allows separating the sensible from the latent heat part. In this regard, the baseline-construction can be more precisely built in the dynamic method than the stepwise one, because more valuable measurement data can be evaluated within very small temperature steps. For this reason, the stepwise method is more appropriate to measure the total enthalpy (both sensible and latent heat) in defined temperature steps and validating the melting peak reached from the dynamic procedure, while the dynamic measurements can ascertain the stored latent heat much more quickly and precisely. Then using the IEA Standard, dynamic measurements are less time-consuming and more precise to characterize the melting behavior of the material.

Further experimental characterizations of the TES capacity of several other types of bio-based PCM, to be employed as environmentally friendly substitute of petroleum-based PCM in cement-based systems, are currently under development.

References

[1] European Commission/. ec.europa.eu/energy/en/topics/energy-efficiency/heating-and-cooling.

[2] EU-EC https://ec.europa.eu/energy/sites/ener/files/documents/germany_de_version.pdf.

[3] Da Cunha, S. R. L., & de Aguiar, J. L. B. (2020). Phase change materials and energy efficiency of buildings: A review of knowledge. Journal of Energy Storage, 27, 101083.

[4] Casini, M. (2016). Smart buildings: Advanced materials and nanotechnology to improve energy-efficiency and environmental performance. Woodhead Publishing.

[5] Cárdenas-Ramírez, C., Gómez, M., & Jaramillo, F. (2019). Characterization of a porous mineral as a promising support for shape-stabilized phase change materials. Journal of Energy Storage, 26, 101041.

[6] He, M., Yang, L., Lin, W., Chen, J., Mao, X., & Ma, Z. (2019). Preparation, thermal characterization and examination of phase change materials (PCMs) enhanced by carbon-based nanoparticles for solar thermal energy storage. Journal of Energy Storage, 25, 100874.

[7] Goia, F., Perino, M., & Serra, V. (2013). Improving thermal comfort conditions by means of PCM glazing systems. Energy and Buildings, 60, 442-452.

[8] Stritih, U., Tyagi, V. V., Stropnik, R., Paksoy, H., Haghighat, F., & Joybari, M. M. (2018). Integration of passive PCM technologies for net-zero energy buildings. Sustainable cities and society, 41, 286-295.

[9] Cabeza, L. F., Castell, A., Barreneche, C. D., De Gracia, A., & Fernández, A. I. (2011). Materials used as PCM in thermal energy storage in buildings: a review. Renewable and Sustainable Energy Reviews, 15(3), 1675-1695.

[10] Dardir, M., Panchabikesan, K., Haghighat, F., El Mankibi, M., & Yuan, Y. (2019). Opportunities and challenges of PCM-to-air heat exchangers (PAHXs) for building free cooling applications—a comprehensive review. Journal of Energy Storage, 22, 157-175.

[11] Sardari, Pouyan Talebizadeh, et al. "Composite metal foam/PCM energy store design for dwelling space air heating." Energy Conversion and Management 201 (2019): 112151.

[12] Wang, Xu, et al. "Experimental assessment on the use of phase change materials (PCMs)-bricks in the exterior wall of a full-scale room." Energy Conversion and Management 120 (2016): 81-89.

[13] Ramakrishnan, S., Sanjayan, J., Wang, X., Alam, M., & Wilson, J. (2015). A novel paraffin/expanded perlite composite phase change material for prevention of PCM leakage in cementitious composites. Applied energy, 157, 85-94.

[14] Aditya, L., Mahlia, T. M. I., Rismanchi, B., Ng, H. M., Hasan, M. H., Metselaar, H. S. C., ... & Aditiya, H. B. (2017). A review on insulation materials for energy conservation in buildings. Renewable and sustainable energy reviews, 73, 1352-1365.

[15] Zhu, L., Yang, Y., Chen, S., & Sun, Y. (2019). Thermal performances study on a façade-built-in two-phase thermosyphon loop for passive thermo-activated building system. Energy Conversion and Management, 199, 112059.

[16] Mehling, H., & Cabeza, L. F. (2008). Heat and cold storage with PCM (Vol. 308). Berlin: Springer.

[17] Akeiber, Hussein J., et al. "Thermal performance and economic evaluation of a newly developed phase change material for effective building encapsulation." Energy conversion and management 150 (2017): 48-61.

[18] Castellón, C., Günther, E., Mehling, H., Hiebler, S., & Cabeza, L. F. (2008). Determination of the enthalpy of PCM as a function of temperature using a heat-flux DSC—A study of different measurement procedures and their accuracy. International Journal of Energy Research, 32(13), 1258-1265.

[19] Jin, X., Xu, X., Zhang, X., & Yin, Y. (2014). Determination of the PCM melting temperature range using DSC. Thermochimica acta, 595, 17-21.

[20] Barreneche, C., Solé, A., Miró, L., Martorell, I., Fernández, A. I., & Cabeza, L. F. (2013). Study on differential scanning calorimetry analysis with two operation modes and organic and inorganic phase change material (PCM). Thermochimica Acta, 553, 23-26.

[21] Gschwander, S., Haussmann, T., Hagelstein, G., Barreneche, C., Ferrer, G., Cabeza, L., ... & Hennemann, P. (2015, December). Standardization of PCM characterization via DSC. In Proceedings of SHC 2015 International Conference on Solar Heating and Cooling for Buildings and Industry (pp. 2-4).

[22] Feng, G., Huang, K., Xie, H., Li, H., Liu, X., Liu, S., and Cao, C. 2016. DSC test error of phase change material (PCM) and its influence on the simulation of the PCM floor. Renewable Energy 87, 1148–1153.

[23] Yinping, Z., & Yi, J. (1999). A simple method, the-history method, of determining the heat of fusion, specific heat and thermal conductivity of phase-change materials. Measurement Science and Technology, 10(3), 201.

[24] Badenhorst, H., & Cabeza, L. F. (2017). Critical analysis of the T-history method: A fundamental approach. Thermochimica Acta, 650, 95-105.

[25] Tan, P., Brütting, M., Vidi, S., Ebert, H. P., Johansson, P., & Kalagasidis, A. S. (2018). Characterizing phase change materials using the T-History method: On the factors influencing the accuracy and precision of the enthalpy-temperature curve. Thermochimica acta, 666, 212-228.

[26] Buttitta, G., Serale, G., & Cascone, Y. (2015). Enthalpy-temperature evaluation of slurry phase change materials with T-history method. Energy Procedia, 78, 1877-1882.

[27] Hong, H., Kim, S. K., & Kim, Y. S. (2004). Accuracy improvement of T-history method for measuring heat of fusion of various materials. International Journal of Refrigeration, 27(4), 360-366.

[28] Stanković, S. B., & Kyriacou, P. A. (2013). Improved measurement technique for the characterization of organic and inorganic phase change materials using the T-history method. Applied energy, 109, 433-440.

[29] Tan, P., Brütting, M., Vidi, S., Ebert, H. P., Johansson, P., Jansson, H., & Kalagasidis, A. S. (2017). Correction of the enthalpy–temperature curve of phase change materials obtained from the T-History method based on a transient heat conduction model. International Journal of Heat and Mass Transfer, 105, 573-588.

[30] Rathgeber, C., Miró, L., Cabeza, L. F., & Hiebler, S. (2014). Measurement of enthalpy curves of phase change materials via DSC and T-History: When are both methods needed to estimate the behaviour of the bulk material in applications? Thermochimica acta, 596, 79-88.

[31] Solé, A., Miró, L., Barreneche, C., Martorell, I., & Cabeza, L. F. (2013). Review of the T-history method to determine thermophysical properties of phase change materials (PCM). Renewable and Sustainable Energy Reviews, 26, 425-436.

[32] Abhat, A. (1983). Low temperature latent heat thermal energy storage: heat storage materials. Solar energy, 30(4), 313-332.

[33] Zhou, D., Zhao, C. Y., and Tian, Y. 2012. Review on thermal energy storage with phase change materials (PCMs) in building applications. Applied Energy 92, 593–605.

[34] DIN 51005. 2005. Thermal analysis (TA) - Terms.

[35] DIN 51007. 2019. Thermal analysis – Differential thermal analysis (DTA) and differential scanning calorimetry (DSC) –General Principles.

[36] IEA-SHC 42 / ECES Annex 29. 2015. Standard to determine the heat storage capacity of PCM using hf-DSC with constant heating/cooling rate (dynamic mode). A technical report of subtask A2.1.

[37] Mankel, C., Caggiano, A., & Koenders, E. (2019). Thermal energy storage characterization of cementitious composites made with Recycled Brick Aggregates containing PCM. Energy and Buildings, 109395.

[38] Caggiano, A., Mankel, C., & Koenders, E. (2019). Reviewing theoretical and numerical models for PCM-embedded cementitious composites. Buildings, 9(1), 3.

[39] Hiebler, S. (2007). Kalorimetrische Methoden zur Bestimmung der Enthalpie von Latentwärmespeichermaterialien während des Phasenübergangs, 90–92.

[40]RUBITHERM-RT®, Technical Datasheets of RT24-RT25-RT26, (09/2018).

[41] PURETEMP 25 Technical Information, (2019 PURETEMP LLC).

[42] ISO 11357-3:2018. Plastics — Differential scanning calorimetry (DSC) — Part 3: Determination of temperature and enthalpy of melting and crystallization.

2.2 Thermo-physical and Mechanical Investigation of Cementitious Composites enhanced with Microencapsulated Phase Change Materials for Thermal Energy Storage

This chapter is published in: Construction and Building Materials, 340, Sam, M., Caggiano, A., Dubyey, L., Dauvergne, J. L., & Koenders, E., Thermo-physical and mechanical investigation of cementitious composites enhanced with microencapsulated phase change materials for thermal energy storage, 127585,
Authorship contribution: Mona Nazari Sam: Conceptualization, Methodology, Validation, Formal analysis, Resources, Data curation, Writing – original draft, Writing – review & editing, Visualization, Funding acquisition. Antonio Caggiano: Conceptualization, Methodology, Formal analysis, Resources, Data curation, Writing – original draft, Writing – review & editing, Visualization, Supervision, Project administration, Funding acquisition. Liliya Dubyey: Methodology, Validation, Resources, Data curation. Jean-Luc Dauvergne: Methodology, Validation, Formal analysis, Resources, Data curation. Eddie Koenders: Conceptualization, Formal analysis, Data curation, Writing – review & editing, Supervision, Project administration, Funding acquisition.

2.2.1 Introduction

The energy consumption of the continuously growing building stock is one of the main reasons for the worldwide rise of anthropogenic CO_2 emissions [1]. Cutting back on this cause asks for a major contribution to the sustainable development goals of tomorrow with the aim to make our world carbon neutral. According to recent EU statistics, heating and cooling of buildings represents the biggest single end-use of the EU's building energy consumption (≈ 60% share), where 84% of this energy is still obtained from fossil resources [2]. Moreover, the building energy demand is envisioned to rise by 79% in residential buildings and 84% in commercial ones until 2050 [3]. This scenario is a clear "call-for-action" for the EU, which has committed itself to various ambitious programs to make renovations of residential and non-residential buildings more energy efficient [4].

A smart management of the thermal energy flows from and to a building can hugely contribute to minimize the annual energy consumption by levelling-out the daily and seasonal temperature fluctuations, while enhancing the energy efficiency of the construction as a whole [5][6][7][8]. A very promising technique, to improve the building energy performance in terms of thermal resistance, can be achieved through a smart use of sensible and/or latent TES components, such as Phase Change Materials (PCMs) embedded in cementitious materials [9][10][11].

PCM can be employed to store/release large amounts of thermal energy, predominantly via the latent branch, during melting or solidification at a nearly constant temperature. Ordinary construction materials, like concrete or mortar, only have an intrinsic sensible heat storage capacity, which varies between approximately 0.75 and 1.00 J/g×K [12][13]. In contrast with this, organic PCM can provide excellent latent heat storage

capacity of approximately 180-230 J/g [14]. Various researches [15][16][17] demonstrated that passive storage/release of latent heat through phase transformation of PCM from solid-to-liquid or vice versa, can contribute to save considerable amounts of primary energy.

The most appropriate and commercially available PCM for building construction materials are organic compounds since they are chemically stable, safe, non-reactive, do not loss their effectiveness with cycling, can be microencapsulated and have a wide temperature range [18]. Organic PCM are available in a wide range of materials, including paraffin and non-paraffin (bio-based). The bio-based ones can be (partly) made from renewable resources and have become very popular due to their eco-friendly image for substituting petroleum-based chemicals by bio-based materials [14].

One point of concern when adding PCM in building elements is to avoid (or at least mitigate) a potential leakage during a phase change [19]. Because of this, some techniques have been proposed to integrate PCM directly into the building materials using encapsulations. For example, microencapsulation is considered as one of the most suitable techniques [20] to integrate PCM directly into a composite material [21][22][23]. In this sense, PCM will be microencapsulated (i.e., MPCM) and they mimic a powder-like material, which size typically ranges between 1 μm to 50 μm [24]. They can be easily mixed with the basic cementitious components and have various advantages like a large surface area for heat transfer, are not sensitive to leakage, have a negligible reactivity towards the external environment and allow a clear control of the phase change process [25]. However, although the implementation of MPCM in building composites has been regarded as a good solution to overcome leakage during a phase change, the low thermal conductivity of the encapsulation material (mainly due to the shell thickness) has turned out to be a serious disadvantage for a rapid heat transfer throughout the MPCM and needs improvement [26][27].

Enhancing the energy efficiency of buildings through a successful incorporation of MPCM in cement-based composites requires more in-depth research [28][29][30][31][32]. Especially drawbacks like shrinkage, or the unsatisfying thermal conductivity of encapsulation material, needs to be comprehended before larger amounts of MPCM can be incorporated in a mixture [33]. Therefore, to produce stable MPCM-cementitious composites, it is of key importance to study mix designs with different MPCM dosages (especially high-volume percentages) and different (from low-to-high)) water to binder (w/b) ratios. In this regard, there is a clear need to further investigate the thermal and mechanical behaviour of cement pastes enriched with MPCM while varying a few factors, such as *core/shell* type and *core size/shell thickness ratio* of MPCM, type of fillers and supplementary components, as well as the mixing procedure. Available studies have already been addressed, which, from an experimental point of view, emphasized the hygro-thermo-chemo-mechanical properties of cement-based materials containing MPCM at several length-scales and applications [34][35]. In these studies, common techniques like Differential Scanning Calorimeter (DSC) [36], Differential Scanning Calorimetry (DSC) and Scanning Electron Microscopy (SEM) [37] have been employed, where the thermo-physical properties of MPCM-cementitious composited were investigated.

Only a few studies available in literature address the importance of MPCM properties once embedded in cementitious composites [38][39]. For instance, Cao et al. [40] pointed out that the early-stage viscosity is

much more affected by MPCM with a hydrophilic surface than those with a hydrophobic one. Furthermore, Coppola et al. [41] described that by increasing amount of MPCM, from 5% to 20% by weight of substituted binder, the workability of paste will be greatly affected, leading to an increased water demand of a mixture. In addition, Sanfelix et al. [42] compared the polarity effect of MPCM shells on the flowability of cement paste and concluded that a Melamine-Formaldehyde (MF) based shell had most suitable rheological properties. It may be worth to mention that the majority of studies showed only limited additions of MPCM, viz. up-to 20 wt% [43][44][45]. Therefore, the main novelty of this paper is on the impact of high amounts of MPCM (up-to 40 %) on the properties of cementitious composites by examining the influence of hydrophobic MF shells on the porosity, strength, and thermal-energy storage, i.e., heat capacity and conductivity.

Energy efficiency in buildings is strongly affected by the ability of insulation materials to (partly) block the outer heat flux. High performance insulation materials are nowadays under development showing a high energy-efficiency while covering all weather and climates. New research directions are dealing with dynamic temperature-adaptable building envelopes, which are applicable in either cold or hot climates. From this, cement-based composites made with MPCMs having melting/solidification temperatures beyond the standard thermal comfort range (i.e., 19 °C and 26 °C) have to be investigated on their potential to be used in TES applications of construction and building materials. For this reason, in this manuscript MPCM-composites with a melting/solidification temperature of 37 °C have been investigated while representing hot temperature climates.

In the present work, results of a detailed experimental program are reported, investigating the thermal behavior of cementitious composites containing MPCM. The thermal analyses were performed by considering DSC measurements and Hot-Disk conductivity tests. The tests were aimed at quantifying the sensible and latent heat storage for cement pastes, MPCM and MPCM-paste systems. Three water-to-binder ratios and three MPCM volume fractions, for a total of nine mixtures, were analyzed. The thermal energy storage study is accompanied by mechanical and other physical tests (including SEM analyses, MPCM contact angle tests, MPCM particle size distribution analysis, MIP and EDS/elemental analysis) to completely investigate the considered MPCM cement paste systems.

2.2.2 Materials and Methods

This section is reporting the Materials and Methods adopted for investigating the properties of components and composites of the experimental study. Samples for thermal, mechanical, and physical analyses were cast and tested for investigating both plain and MPCM-cement pastes.

2.2.2.1 Materials and Mixtures

A Portland cement CEM I 52.5R [46] with a density of 3.10 g/cm^3 was used. To reduce the environmental impact of the cement, an eco-friendly metakaolin binder (namely Centrilit NC II made of reactive

aluminosilicate pozzolan [47]) was also used as partial substitute of the CEM I 52.5R. The chemical composition of both binders is listed in Table 5.

Table 5. Overview chemical composition of cement (CEM I 52.5 R) and Metakaolin (Centrilit NC II).

Chemical composition [% weight]	**SiO2**	**Al2O3**	**Fe2O3**	**CaO**	**MgO**	**Na2O+K2O**
Cement CEM I 52.5 R	20.10	4.50	3.30	64.90	1.40	0.93
Metakaolin	52.1	41.0	4.32	0.07	0.19	0.89

Paraffin-based MPCM were evaluated, namely Nextek 37D® (labelled as N-MPCM) provided by Microtek Laboratories [48]. N-MPCM is composed of a paraffin-mixture core and a melamine-formaldehyde polymer shell (MF) and its main properties are outlined inTable 6.

Table 6. Thermo-physical properties of Nextek 37D® N-MPCM [48].

Properties	**N-MPCM**
Core	Paraffin mix
Shell	Melamine Formaldehyde (MF)
Tm, peak [ºC]	37
Density [g/cm3]	0.76
Latent heat capacity [J/g]	190-200
Mean particle size [µm]	15-30

Nine N-MPCM-cement mixtures were considered which were made with three different water-to-binder (w/b) ratios and 3 amounts (0, 20% and 40%) of N-MPCM volume fractions. All mixtures have been prepared following the casting procedure of EN 196-1 [49] and the recipes of Table 7. The table's first row indicates the label of the mixture highlighting the necessary information on the considered w/b ratio along with the amount of N-MPCM (expressed in % of paste substitution, see Figure 23). For example, ''S-45-20'' refers to a mixture having a w/b=0.45 and 20% of N-MPCM volume fraction.

After making different trials of mixing procedures, the order of component addition and mixing conditions were optimized as follows. First, cement and metakaolin were hand-mixed until a homogeneous appearance was achieved. Then, the binder was mixed with water for 120 s followed by a superplasticizer and mixed for another 60 s until the appropriate workability of the mixture was reached. The stabilizer was added to the mixture for further 30 s. At this point, for the reference pastes (without N-MPCM) the hardening agent was added and mixed for another 30 s, after which the paste was immediately poured into the moulds. For mixtures with N-MPCM, the procedure was optimized by considering again the workability of the paste,

mixing the N-MPCM with the cement paste for an additional 90 s, during which mostly extra superplasticizer was added. The procedure was finished by adding the hardening agent and mixing it for a final 30 s.

Table 7. Mix overview of the nine paste systems.

Labels	S-45-ref [kg/m^3]	S-45-20 [kg/m^3]	S-45-40 [kg/m^3]	S-40-ref [kg/m^3]	S-40-20 [kg/m^3]	S-40-40 [kg/m^3]	S-33-ref [kg/m^3]	S-33-20 [kg/m^3]	S-33-40 [kg/m^3]
w/b ratio	0.45			0.40			0.33		
Cement	983.4	786.7	590.0	1043.1	834.5	625.8	1140.0	912.0	684.0
Metakaolin	161.8	129.4	97.1	171.6	137.3	103.0	187.6	150.1	112.5
Water	515.3	412.3	309.2	485.9	388.7	291.5	438.1	350.5	262.8
Superplasticizer	5.7	4.6	3.4	6.0	4.8	3.6	6.6	5.3	3.9
Stabilizer	33.1	26.5	19.8	35.1	28.0	21.0	38.3	30.7	23.0
MPMC [V.-%]	-	20	40	-	20	40	-	20	40
Hardening accl.	22.9	18.3	13.7	24.3	19.4	14.5	26.5	21.2	15.9

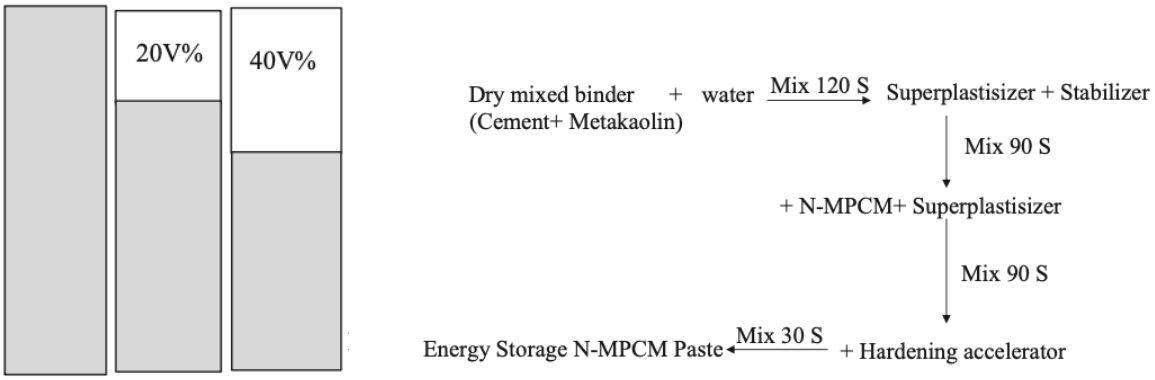

(a) (b)

Figure 23. Cement pastes: (a) N-MPCM volume fractions and (b) mixing procedures.

The batch volume was calculated to produce at least 3 prisms of 40 mm × 40 mm × 160 mm (employed for mechanical testing and microstructure/porosity measurements), two cylindrical samples of 20 mm high and 56 mm of diameter, needed for the hot-disk measurements, and three crucibles for DSC analyses. One day after casting, all the specimens were demoulded and stored in a water bath at 20° C, until 28 days. Subsequently, mechanical tests were performed. DSC and thermal conductivity measurements were also conducted with specimens that were stepwise dried at 30° C, 40° C and 50° C until they reached a constant mass.

2.2.2.2 Methods

N-MPCM

Characterization of N-MPCM was performed by evaluating the particle size distribution, shell polarity with contact angle measurements, as well as morphology with SEM analyses.

Particle size distribution

To determine the mean particle size of the N-MPCM, laser granulometry (Partica LA-950 Laser Diffraction Particle Size Distribution Analyzer) was used. It works according to the following principle: a laser is scattered by a group of particles. The angle of light scattering is inversely proportional to particle size. The diffraction patterns of different particle diameters are well known. So, a mathematical algorithm based on the Mie theory is used to compute the portion of the theoretical spectra of all particle size classes from the experimentally determined total spectrum. The complex refractive index of the particle is needed by employing the Mie theory. With the knowledge about the N-MPCM shell material, it is possible to know the refractive index and to perform this measurement. Considering that N-MPCM is essentially made of melamine-formaldehyde, the refractive index value taken from the literature was 1.68 [50].

Contact angle measurement

One of the aims of this work is also to investigate the influence of the N-MPCM shells on the surrounding microstructure of the cementitious composite. Therefore, the measurement of the contact angle is of key importance in this sense because it is one of the most practical parameters to effectively characterize the hydrophilic/hydrophobic nature of a material surface.

The contact angle is a measure between the liquid-solid and the vapor-liquid interfaces (namely, where the vapor-liquid interface tangent line from the point of intersection of the liquid, solid, and vapor phases meet, "three phase contact point", along with the vapor-liquid interface of the droplet).

This is a balance of three equilibrium interfacial tensions that follows equation [51]:

$$\gamma_{LG} \cos\theta = \gamma_{SG} - \gamma_{sL} \quad (1)$$

where θ is the contact angle and γ_{LG}, γ_{SG} and γ_{SL} represent the liquid-vapor, solid-vapor, and solid-liquid interfacial tensions, respectively. Surfaces with a higher tendency to absorb water molecules possess a contact angle lower than 90˚ and are defined as "hydrophilic". On the contrary, surfaces with less affinity towards water are so-called "hydrophobic", showing a contact angle higher than 90˚ and they tend to reject water molecules. To determine the water affinity of N-MPCM, the contact angle was measured using the Contact Angle (CA) goniometer (OCA instrument: *DataPhysics Instruments, Filderstadt, Germany*). A static Milli-Q water droplet with a volume of 3 ul was placed on the sample. The CA was determined via Young–Laplace alignment 1 s after drop generation.

N-MPCM-cementitious pastes

The characterization methods employed to investigate the mechanical, thermal, and physical properties of the designed pastes are presented in this section.

Differential Scanning Calorimeter (DSC)

The DSC 214 Polyma equipment was used to perform the DSC studies on the either with or without N-MPCM cementitious pastes. DSC is a thermo-analytical technique that measures released (exothermic) and absorbed (endothermic) heat with varying temperatures. It is a commonly used technique to determine heat

capacities, melting peaks, and enthalpies of PCM, N-MPCM, as well as N-MPCM-enhanced composites. The samples were prepared in aluminum DSC crucibles (Figure 24 a), cured until 28 days, and oven-dried at 50 ºC until a constant weight was achieved. The crucibles have a diameter of 6 mm and a maximum volume capacity of 40 µl. A small hole (Figure 24b) was made in their lid to enable isobaric measurements. The German Standards DIN 51005 and DIN 51007 [52][53] were considered as a reference to perform the DSC tests, while the IEA standard procedure [54] was followed to determine the latent heat storage capacity of N-MPCM-composites. The thermal program used included a temperature interval from 15 ºC to 45 ºC (for heating and cooling), considering that the melting temperature of the N-MPCM is around 37 ºC. Each measurement included three cycles of heating and cooling, with an isothermal 10-minute section to ensure that the thermodynamic equilibrium is attained. All measurements were done under an inert nitrogen environment at a flow of 60 ml/min. The measurements for the paste with N-MPCM were done at a rate of 0.5 K/min and for reference pastes at a rate of 10 K/min.

(a) (b)

Figure 24. (a) aluminum sample holders (maximum volume capacity of 40 µL) and (b) prepared sample inside crucible with a small hole on top.

Mechanical tests

To characterize the mechanical response of the N-MPCM cement pastes prismatic samples were tested following the procedures described in EN 196-1 [49]. For each mixture with the commercial N-MPCM, 9 prisms (40 mm × 40 mm × 160 mm) were prepared and tested after 3, 7, and 28 days. Three identical samples per each mixture/maturation were considered which were firstly tested under a three-point bending scheme. The distance between the bending supports was 100 mm (± 0.5 mm) and the vertical load was imposed with a loading rate of 50 N/s until failure. Then, compression tests were performed by employing one half of a broken beam. The bending strength R_f of all mixtures was calculated by means of the following expression [49]:

$$R_f = \frac{1.5 \cdot F_f \cdot l}{b^3} \tag{2}$$

where b *[mm]* is the rib size of the beam cross-section, F_f *[N]* the applied load and l *[mm]* the distance between the end supports. The compressive strength was determined according to the following formula:

$$R_c = \frac{F_c}{A_c} \tag{3}$$

being F_c *[N]* the failure load and A_c the area of the auxiliary plates (40×40 mm^2).

Mercury intrusion porosimeter (MIP)

MIP tests (as shown in Figure 25) were executed to better understand the changes in the pore structure of the considered composites. Pore structure plays a major role in both mechanical and thermal properties of cement pastes.

(a) (b)

Figure 25. a) Sample holder together with Specimen Fractures tested under MIP and b) Mercury intrusion porosimeter Thermo Scientific Pascal 140 and 440.

Mixtures with higher w/b ratios are expected, not only to have lower compressive strengths, but also to have higher pore volumes and larger critical pore diameters. Moreover, the addition of N-MPCM might also affect the pore structure by reducing the hydration degree and rate, which keeps pores larger and free of hydration products.

The Washburn equation, which assumes a cylindrical pore shape, is used to analyze MIP results [55]. The pore size detected is influenced by two factors: the surface tension of mercury (γ) and the contact angle between the mercury and the pore surface (θ). The latter evaluates the pore size as follows:

$$D = \frac{4\gamma cos\theta}{P} \tag{4}$$

Morphological and elemental analysis via SEM

Scanning Electron Microscopy (SEM) analyses were performed for N-MPCM cement pastes to investigate microscopic properties of composites in terms of geometry, shape, particle size, and particle distribution. For this purpose, the analysis can shed information on the following characteristics:

- Homogeneous distribution of N-MPCM;
- Integrity of shell structures of N-MPCM;
- Particle size and uniformity of N-MPCM;
- Thermal and mechanical stability of microcapsules;
- Effect N-MPCM have on the microstructure of the cementitious composite.

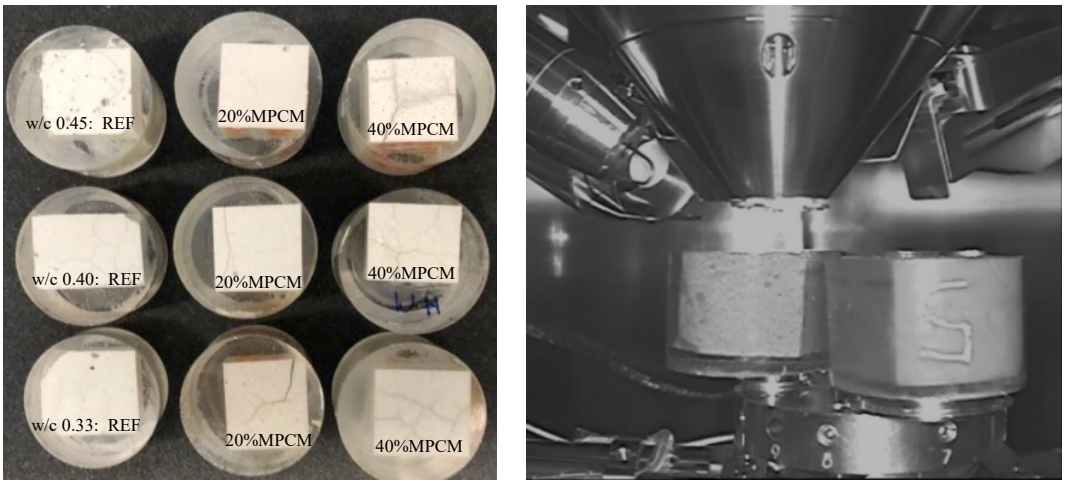

(a) (b)

Figure 26. a) 2×2×2 cm^3 cement paste samples being impregnated and polished and b) samples inside the vacuum chamber being tested under SEM.

The microstructure of the cementitious samples was observed through an Atmospheric scanning electron microscope (Zeiss EVO LS25) after 28 days of curing. The samples were cut into approximately 2×2×2 cm^3 and placed in cylindrical molds as shown in Figure 26. For sample preparation, vacuum impregnation was used to embed the samples in an epoxy mixture (i.e., 25 g of epoxy to 3 g of hardening accelerator).

Afterward, the surface was polished with a Lab polishing device. All samples were visualized at an accelerating voltage of 15 kV. Back-scattered-electrons (BSE) mode and Second Electron (SE) mode were used to obtain good contrast between the microcapsules and the cementitious matrix, as well as the topographic analysis, respectively.

Elemental analyses of samples were accomplished by using Energy-Dispersive X-ray spectroscopy (EDX) while elemental mappings were performed in low vacuum mode (at 10 Pa) with a voltage of 15 kV, beam current of 2.0 nA and an EDX detector (EDAX, Ametek, Berwyn, PA, US).

Hot Disk TPS Thermal conductivity

The assessment of the effective thermal conductivity was performed by means of the Transient Plane Source (TPS) method, known as Hot-disk following the norm Hot Disk ISO 22007-2:2015. Upon 28 days of curing, two cylindrical samples (56±1 mm diameter and 25±1 mm thickness) (see Figure 27 a) of each mixture were analyzed.

This method is based on the use of a transiently heated plane sensor sandwiched between two samples of the material to be characterized (see Figure 27 b). The measurements were done with a Kapton 5501 sensor (6.403 mm) (see Figure 27 c), inside of a climatic chamber at 10 ºC below and above the melting point of the incorporated N-MPCM during 40 s, and for reference samples at 20 °C during 80 s, both with a heating power of 80 mW.

(a) (b) (c)

Figure 27. a) Test set-up for the TC measurement b) Cured sample prepared for the TC measurement and c) and Hot Disk Kapton 5501 sensor.

Relative humidity was fixed at 60 % RH for all the experiments. At least 3 measurements were carried out for each sample by moving it between each test, and the recorded data were processed using the Hot Disk Software (version 7.4.0.10).

2.2.3 Results and Discussion: N-MPCM

2.2.3.1 Morphology of the N-MPCM

Particle size of N-MPCM was investigated through size diffractometer measurements, while their visual appearances were verified through SEM analyses. In this sense, Figure 28 (a) plots the cumulative and discrete size distribution of the N-MPCM, while Figure 28(b) shows the physical appearance of the capsules. The N-MPCM presents a mean particle size of 20.9 µm: this result is also confirmed by SEM visualization and diameter measurements of a single capsule. It is then observed that N-MPCM has a low tendency to agglomerate, confirmed by the almost absence of large, shaped spheres (Figure 28b) which is often caused by particle grouping.

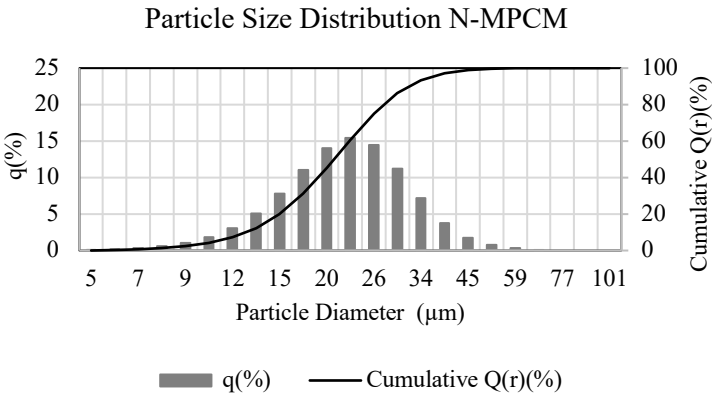

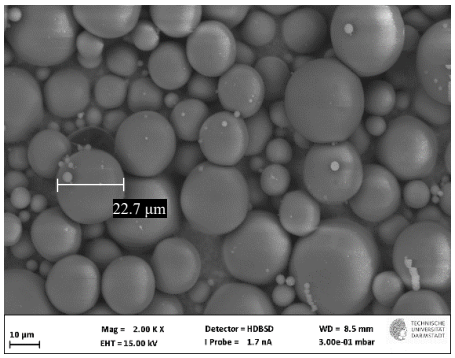

(a) (b)

Figure 28. (a) cumulative (solid line) and discrete (histogram bars) particle size distribution of N-MPCM and (b) SEM visualization of pure Nextek 37D® MPCM.

The wettability of the N-MPCM microcapsules was assessed with contact angle measurements which results are presented in Figure 29. The sub-Figure a) marked with a blue square box shows the moment in which the drop got attached to the base support where the angle is experimentally measured. The test was performed 10 times in different parts of the tape and the mean value was determined. It was experimentally observed that the droplet on N-MPCM capsules was relatively static, after being dropped, without being absorbed into the sample. This deals with the hydrophobic nature of the N-MPCM microcapsules.

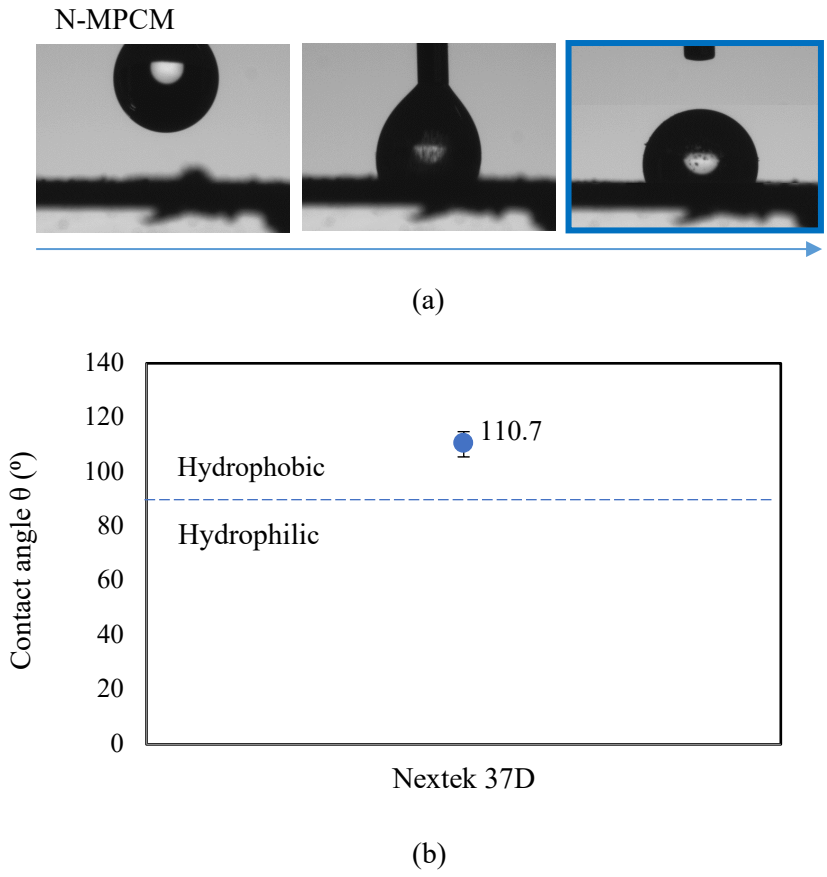

Figure 29. (a) Contact angle measurement of N-MPCM and (b) Average value among 10 measurements.

Particularly, the results show that the N-MPCM contact angle presents an average of 110.7 º. Hence, reminding that the higher the contact angle the more hydrophobic is the sample, it can be concluded that the N-MPCM is characterized by a clear hydrophobic microencapsulation. This is an important finding to take into consideration for the stability/performance of cementitious composites made of mixing pastes and N-MPCM microcapsules.

Thermal properties of the N-MPCM

To investigate the latent heat performance of the selected N-MPCM, DSC measurements were performed on the powder-like N-MPCM. Samples of around 10 mg were considered for the DSC-measurements, while three samples with three periodic cycles of heating/cooling by considering a heating/cooling rate of 0.5 K×min–1 were investigated. The chosen heating/cooling rate was experimentally determined to provide a negligible influence on the heating/cooling peak of the final DSC curves [14]. The record of the DSC curves

is expressed in terms of heat flow versus temperature. From these results, the specific heat capacity and latent enthalpy of the N-MPCM was subsequently calculated (see Figure 30 a and b, respectively).

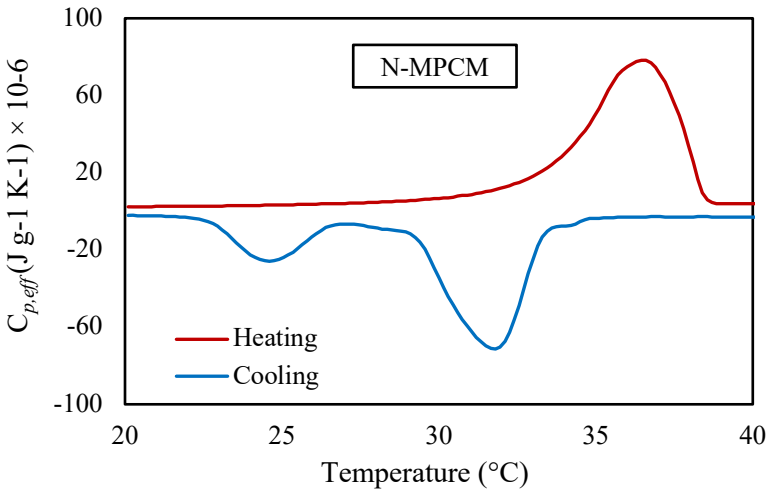

(a)

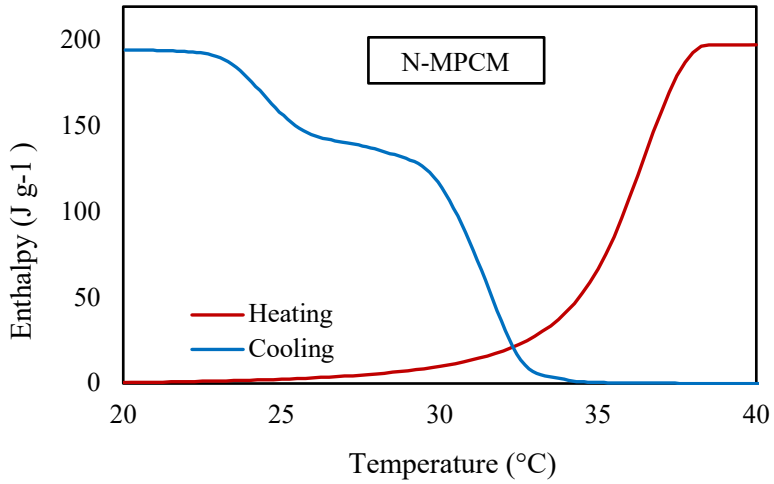

(b)

Figure 30. Results of DSC measurements of pure N-MPCM obtained with a heating/cooling rate of 0.5 K / min (a) $C_{p,eff}$ versus T for heating and cooling between 20 °C and 40 °C (b) latent heat storage (enthalpy) in the melting Temperature range of pure N-MPCM.

Figure 30 *a* shows the results of DSC measurements expressed as $C_{p,eff}$ versus T. The thermographs show that the shape of the curves is quite similar for heating and cooling where a clear one-peak response can be observed for heating, while two peaks characterize the cooling. This suggests that the N-MCPM has a tendency for subcooling. However, despite the differences in the heating/cooling peaks and shapes they did not have influence the total melting/freezing enthalpy.

The applicable melting temperature range (under heating) of the N-MPCM starts at 33.4 °C and reaches the peak at 36.5 °C. Under cooling cycle, the solidification starts at 33.3 °C and reaches its peak at 31.7 °C. The values of the latent heat obtained for N-MPCM is 197.3 J/g and 194.6 J/g, for heating and cooling,

respectively (see Table 8). The latter coincide within the range of 190-200 J/g as provided by the provider´s data sheet [48].

Table 8. Results from DSC measurements of N-MPCM, with a heating/cooling rate of 0.5 k/min.

		$T_{transition,\ onset}$ [°C]	$T_{transition,\ peak}$ [°C]	Latent heat [J/g]
Heating	N-MPCM	33.4	36.4	197.3
Cooling	N-MPCM	33.3	31.7	194.6

2.2.4 Results and Discussion: N-MPCM-Pastes

This section aims at providing an extensive characterization of the thermo-physical properties of the designed cementitious systems with and without N-MPCM incorporation.

2.2.4.1 DSC results

Reference pastes

DSC results of the three reference cement pastes, with a w/b ratio of 0.45, 0.40, and 0.33, were examined. The DSC measurements were carried out with a heating/cooling rate of 10 K/min and the effective heat capacities are shown in Figure 31. The thermal storage performance of the three different cement pastes, over the entire examined temperature range from 5 °C to 40 °C, is characterized by an exclusively sensible TES behavior. As it can be appreciated from the curves obtained, there is an almost identical behavior for all pastes. When comparing the heat capacity per unit of mass (Figure 31-a), the paste "REF w/b 0.45" has a slightly increased heat storage capacity compared to either "REF w/b 0.40" or "REF w/b 0.33". However, in terms of volumetric heat capacity (Figure 31-b), the order changes, having "REF 0.33" a slightly higher storage capacity than "REF 0.45" and "0.40".

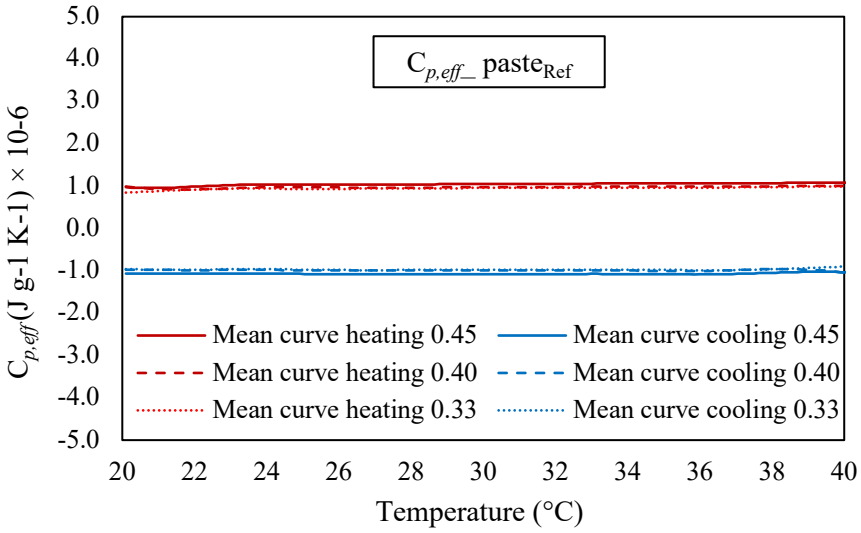

a)

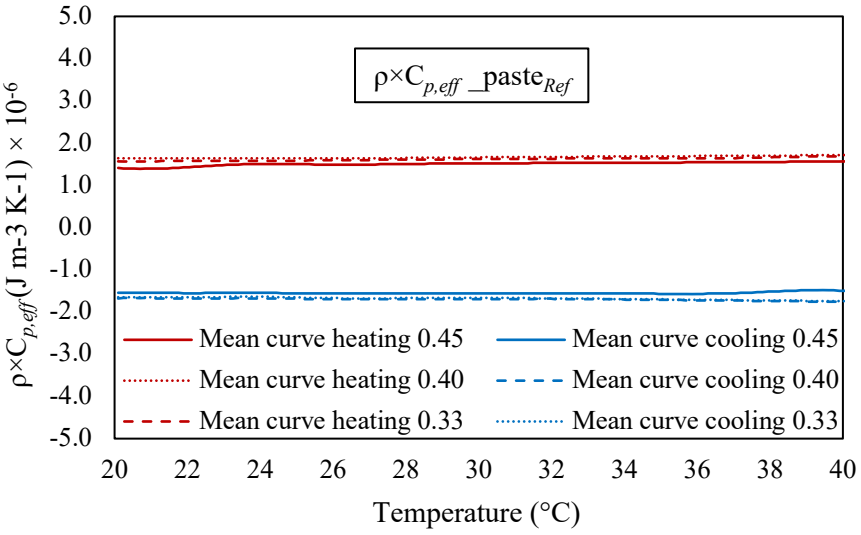

b)

Figure 31. DSC results of the pastes (w/b=0.45, 0.40 and 0.33): a) $C_{p,eff}$ vs T and b) $\rho \times C_{p,eff}$ vs T.

This fact is due to the higher bulk density of the REF 0.33 paste with the calculated dry density of 1824 kg/m³ and the measured dry density of 1702 kg/m³, in contrast to lower values for "REF 0.45" and "REF 0.40" (see Table 9). Furthermore, the results also show a typical temperature dependence of the heat storage capacity with a slightly increasing trend at higher temperatures.

Cement pastes with N-MPCM 20 vol.-% and 40 vol.-%

Analogous to the measurements of the pure N-MPCM, a heating rate test was carried out prior to the measurements for the N-MPCM-pastes. This was necessary to fulfill the requirements of the IEA-SHC 42 Standard (see [14] and [54]): the proper heating/cooling rate which ensured the required thermal equilibrium within the sample, during the measurements, was found to be 0.5 K/min. Therefore, all measurements were carried out under the heating/cooling rate of 0.5 K/min while three different samples for the same mixture design were tested, each within three identical heating/cooling cycles. Figure 32(a) and (b) show the average $C_{p,eff}$ curves obtained from the DSC-measurement results. To ease comparability of the results, and because of the volumetric substitution of N-MPCM in cement matrices, also the graphs regarding the volumetric heat capacity ($\rho \times C_{p,eff}$) are presented, see Figure 32(c) and (d) . In order to calculate the volumetric heat capacity ($\rho \times C_{p,eff}$), the paste densities ρ were taken from the conducted MIP results (more details are available in Section 2.2.4.4) and presented in Table 9.

Table 9. Paste densities with and without N-MPCM measured via Heliumpyknometer.

Sample labels	**S-45-ref**	**S-45-20**	**S-45-40**	**S-40-ref**	**S-40-20**	**S-40-40**	**S-33-ref**	**S-33-20**	**S-33-40**
ρ (g/cm3)	1.450	1.332	1.126	1.708	1.438	1.221	1.702	1.584	1.242

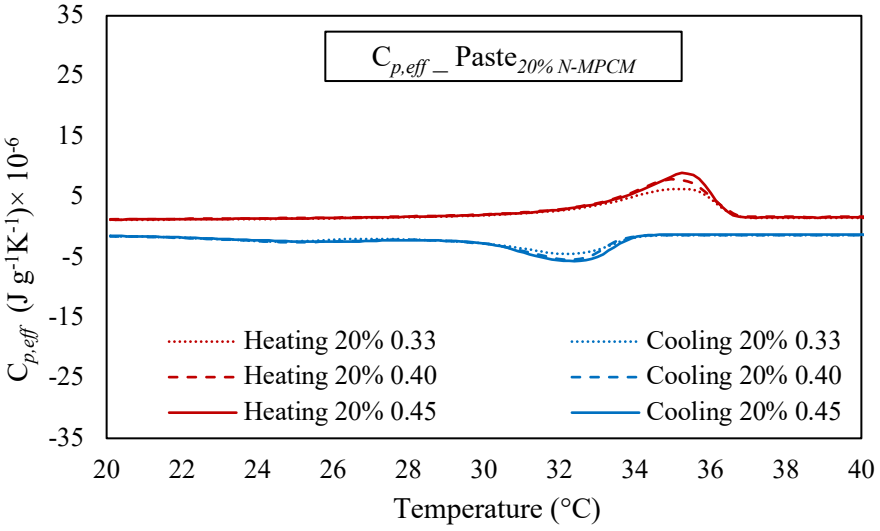
$C_{p,eff}$ _ Paste$_{20\%\ N\text{-}MPCM}$
$C_{p,eff}$ (J g^{-1}K^{-1})× 10^{-6}
Heating 20% 0.33
Heating 20% 0.40
Heating 20% 0.45
Cooling 20% 0.33
Cooling 20% 0.40
Cooling 20% 0.45
Temperature (°C)

(a)

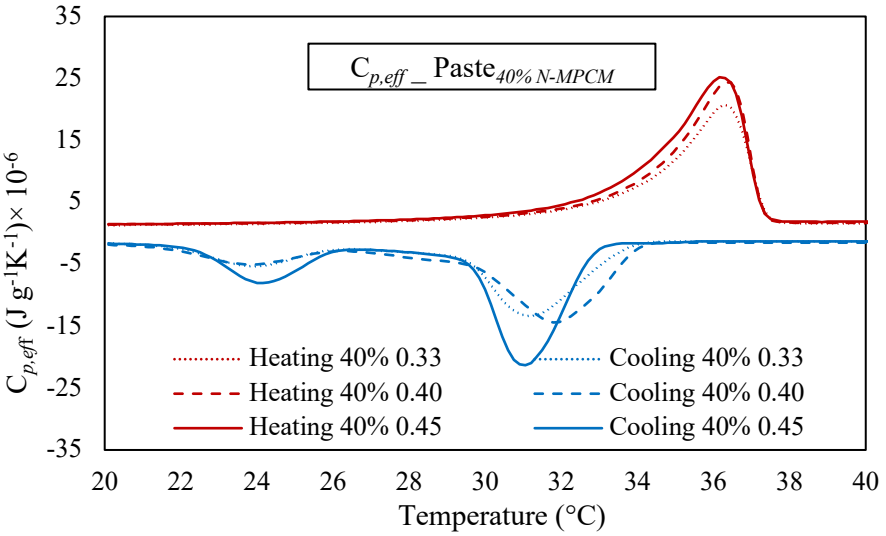
$C_{p,eff}$ _ Paste$_{40\%\ N\text{-}MPCM}$
$C_{p,eff}$ (J g^{-1}K^{-1})× 10^{-6}
Heating 40% 0.33
Heating 40% 0.40
Heating 40% 0.45
Cooling 40% 0.33
Cooling 40% 0.40
Cooling 40% 0.45
Temperature (°C)

(b)

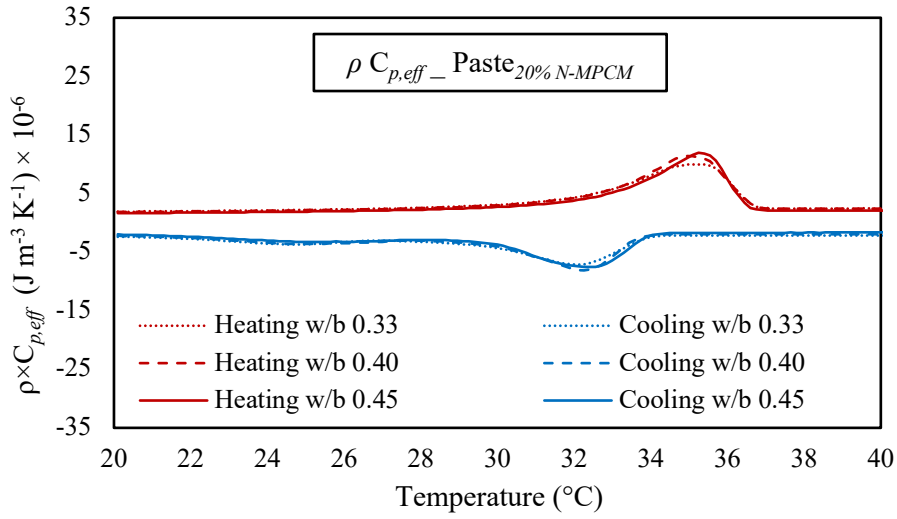
ρ $C_{p,eff}$ _ Paste$_{20\%\ N\text{-}MPCM}$
ρ×$C_{p,eff}$ (J m^{-3} K^{-1}) × 10^{-6}
Heating w/b 0.33
Heating w/b 0.40
Heating w/b 0.45
Cooling w/b 0.33
Cooling w/b 0.40
Cooling w/b 0.45
Temperature (°C)

(c)

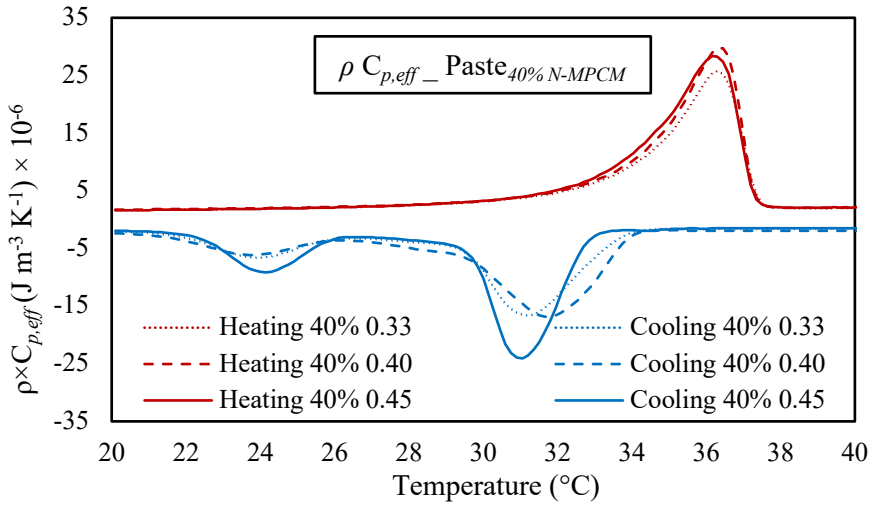

(d)

Figure 32. DSC results- (a) Cp,eff of 20% and (b) 40% N-MPCM pastes (w/b=0.45, 0.40 and 0.33). (c) ρ×Cp, eff of 20% and (d) 40% N-MPCM pastes (w/b=0.45, 0.40 and 0.33).

From the plotted graphs in Figure 32, the melting onset temperatures (i.e., Onset temp.), the peak temperatures (Peak temp.) and the latent heat capacities have also been listed in Table 10. The graphs of Figure 32 and the values of Table 10 show that the w/b ratio does not significantly influence the thermal behavior of the N-MPCM enhanced cementitious composites. The lowest onset temperature for heating was 32.2 °C while the highest one (upon cooling) was 34.4 °C. The peak temperature is achieved slightly later for 40% N-MPCM, being this peak reached at 36.6 °C by heating cycles.

Table 10. DSC summary for 20% and 40% N-MPCM pastes: melting/solidification onset, peak temperatures, and latent heat storage (average of 3 samples per 3 measurement cycles is reported).

Mode	N-MPCM Vol.-%	w/b	Onset temp. (°C)	Peak temp. (°C)	Latent heat (J/g)	Latent heat (MJ/m^{-3})
Heating	20	0.45	32.8	35.3	19.08	25.42
		0.40	32.6	35.0	18.12	26.06
		0.33	32.2	35.0	15.12	23.95
	40	0.45	33.6	36.1	57.12	64.10
		0.40	34.1	36.6	49.94	60.98
		0.33	34.0	36.4	45.76	56.80
Cooling	20	0.45	34.4	32.8	16.25	-21.65
		0.40	34.0	32.8	15.45	-22.22
		0.33	34.4	32.4	12.61	-19.97
	40	0.45	33.3	31.5	54.73	-61.63
		0.40	34.4	32.3	47.01	-57.40
		0.33	34.4	31.9	42.45	-52.72

Regarding the effect of the w/b ratio on the enthalpy of the mixtures, there is no big scatter between the conducted average values (Figure 33). This result is almost expected since the N-MPCM volume fraction substituted for either 20 Vol.-% or 40 Vol.-% is the same for the different mixtures, independently on the

w/b. Therefore, the measured enthalpy is expected to stay constant. These results are also certificating that the casting procedure used will not negatively affect the heat storage potential of the prepared samples. However, a small decreasing trend of mass-specific enthalpy with decreasing w/b ratio was observed (Figure 33), the volumetric amount of Enthalpy presents almost a constant average amount of 20-25 (MJ/m³) for samples with 20% N-MPCM and 55-60 (MJ/m³) for samples with 40% N-MPCM.

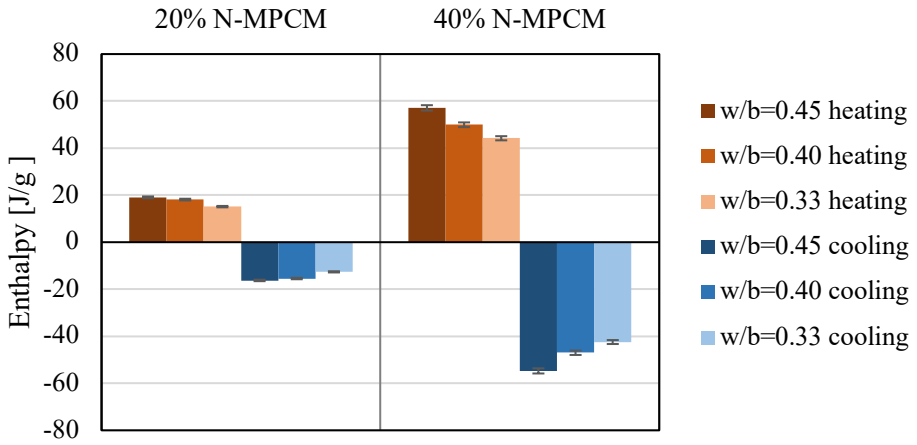

Figure 33. Mass-specific amount of Enthalpy among different paste samples with different w/b ratios for 20% and 40% volumetric amount of N-MPCM.

A higher mass-specific enthalpy was achieved for w/b = 0.45, which is because to achieve the same amount of mass between the three w/b ratios, there is a need for more material in the case of w/b=0.45, due to its lower density than w/b=0.33. In other words, there is a slightly higher amount of N-MPCM in 1 g of a sample with w/b = 0.45 than in 1 g of a sample with w/b = 0.33, which leads to a higher enthalpy for the w/b of 0.45.

2.2.4.2 Conductivity results

The thermal conductivity of cementitious pastes containing varying amounts of N-MPCM (i.e., 0%, 20% and 40%) was measured using the transient plane source method, commonly known as Hot-Disk.

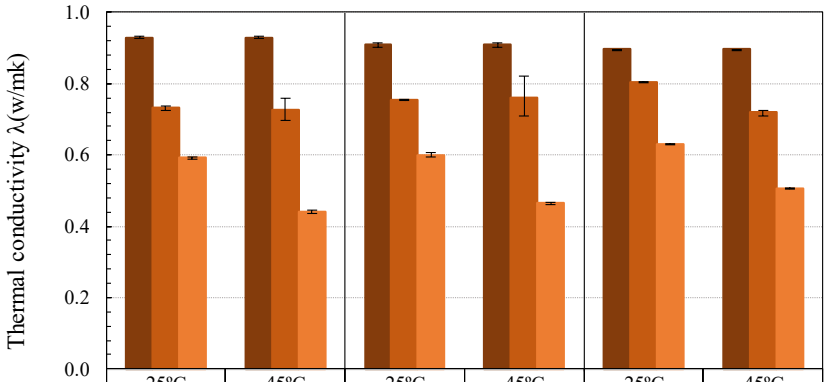

	25°C	45°C	25°C	45°C	25°C	45°C
	N-MPCM 0.45		N-MPCM 0.40		N-MPCM 0.33	
REF	0.9296	0.9296	0.9099	0.9099	0.8964	0.8964
20% - MPCM	0.7337	0.7276	0.7539	0.7596	0.8054	0.7202
40% - MPCM	0.5924	0.4414	0.6002	0.4642	0.6310	0.5066

Figure 34. Thermal conductivities among different w/b ratios for REF, 20% and 40% N-MPCM pastes.

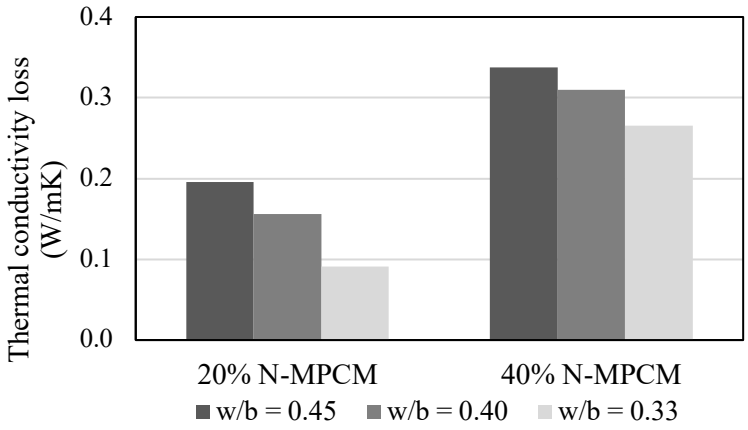

Figure 35. Thermal conductivity loss among different w/b ratios for 20% and 40% N-MPCM pastes.

Conductivity values were measured after 28 days of curing time with N-MPCM kept in solid-state (i.e., 10 ºC below and above the melting peak previously measured in DSC tests of the incorporated N-MPCM). The results are shown in Figure 34. In all samples with w/b=0.45, 0.40 and 0.33, increasing N-MPCM amounts resulted in a decrease of the thermal conductivity. This is because of the higher thermal conductivity of cement paste comparing to the N-MPCM which replacement contributes to an overall decrease in the mixture's thermal conductivity. In this sense, Figure 35 shows the thermal conductivity loss of N-MPCM pastes compared to the reference ones. As general observation, it can be concluded that the decrease of thermal conductivity (W/m×K) is less pronounced in the lower w/b of 0.33, in which the increase of N-MPCM from 20% to 40% contributes to further thermal conductivity decrease (of circa 22%).

2.2.4.3 Mechanical tests

Bending tests

Flexural tests were performed for characterizing the bending strengths of the considered N-MPCM pastes. Strength results of each paste, analyzed according to the specifications outlined in Section 2.2.4.3, are presented in Figure 36 and Figure 37. From the results it can be observed that the N-MPCM substitution plays a major role on the overall flexural strength reductions. Particularly, this effect is clear and much more dominant for those paste systems, casted with a w/b ratio of 0.33. A remarkable strength loss can be measured when 20% and 40% of N-MPCM volume fractions were substituted, leading to reductions of 23.91% and 48.55% (upon the mean bending strength). The cementitious pastes with a w/b=0.40 and 0.45 showed almost the same trend, but much less evident. The flexural strengths of the REF pastes 0.40 and 0.45 present surprisingly low resistances, probably due to the uncomplete hydration process of the binders (specially the metakaolin ones) and because of early age cracking due to shrinkage.

Figure 36 and Figure 37 show the same results, however the first one is aimed at emphasizing the comparative effects of the N-MPCM substitution on the flexural strength, the second on the different w/b ratios. From the latter, it can be observed that bending strengths were strongly influenced by the w/b ratio, meaning: the higher the w/b ratio the lower the corresponding flexural strength.

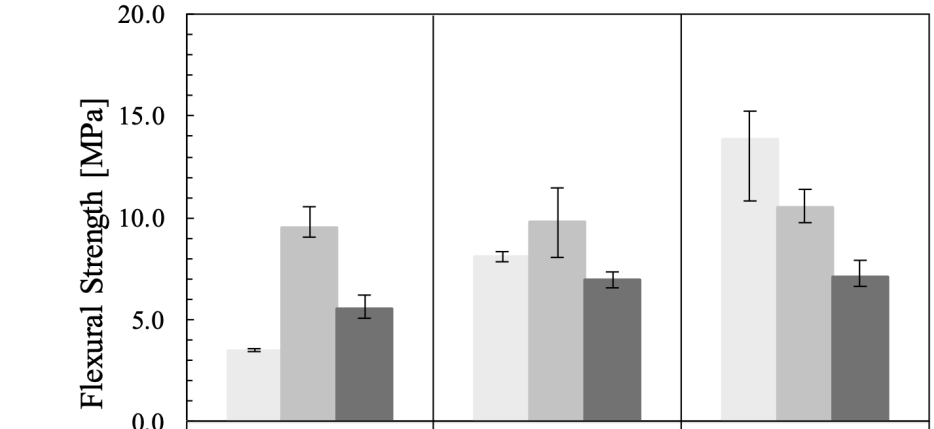

	w/b 0.45	w/b 0.4	w/b 0.33
REF	3.5	8.1	13.8
20% - MPCM	9.5	9.8	10.5
40% - MPCM	5.5	6.9	7.1

Figure 36. 28-days flexural strength values among different w/b ratios and comparing REF, 20% and 40% N-MPCM volume fraction in pastes.

As a matter of fact, this conclusion is quite common for cement-based materials, and the same trend is also followed when the N-MPCM substitutions are considered (see Figure 37). However, when higher volumes of N-MPCM are substituted in the cement paste, the flexural strength rise turned out to be much less evident among the mixtures with different w/b ratio.

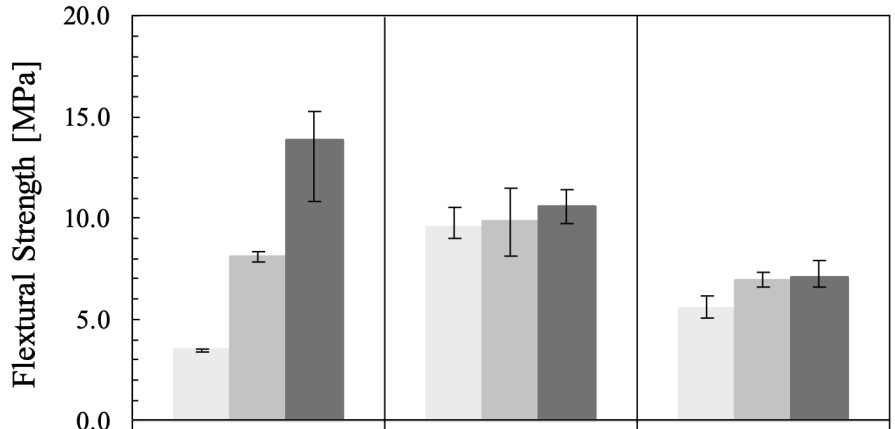

	REF	20% - MPCM	40% - MPCM
w/b 0.45	3.5	9.5	5.5
w/b 0.4	8.1	9.8	6.9
w/b 0.33	13.8	10.5	7.1

Figure 37. 28-days flexural strength values among different N-MPCM volume fractions and comparing w/b 0.45, w/b 0.40, and w/b 0.33 of pastes.

This response can be explained by analyzing the volumetric ratio between the amount of binder and the relative increase of the amount of N-MPCM, which leads to a system that behaves similarly because of the comparable amount of binder. Similar observations were done for the variable w/b ratios and N-MPCM

volume substitutions at different maturation times of testing (i.e., 3 days, 7 days, and 28 days), as shown in Figure 38.

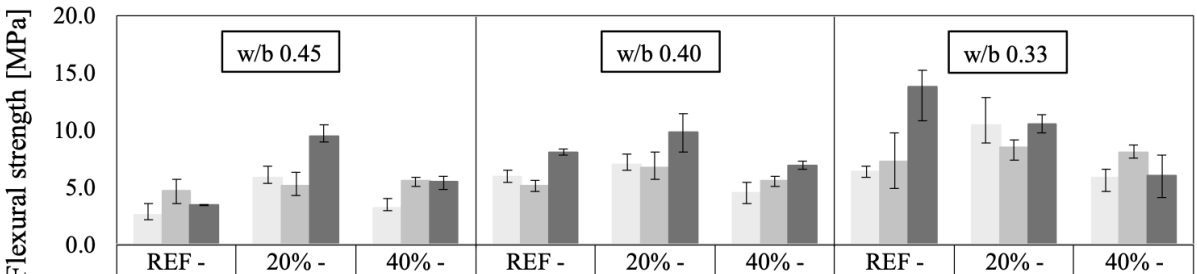

	REF - 0.45	20% - MPCM	40% - MPCM	REF - 0.40	20% - MPCM	40% - MPCM	REF - 0.33	20% - MPCM	40% - MPCM
3 days	2.57	5.87	3.25	5.99	6.98	4.54	6.40	10.46	5.84
7 days	4.69	5.19	5.56	5.19	6.72	5.60	7.24	8.50	8.11
28 days	3.48	9.52	5.51	8.11	9.81	6.93	13.84	10.55	6.04

Figure 38. Flexural strength values among different w/b ratios, for REF, 20% and 40% N-MPCM pastes and comparing 3, 7 and 28 days of curing time.

Compressive tests

Compressive strength tests were also performed to investigate the influence of N-MPCM on the mechanical properties of the designed mixtures. The tests were conducted for reference samples, as well as for the samples with volumetric fractions of 20% and 40% N-MPCM. The comparison of the measured compressive strength results at 28 days of curing are presented in Figure 39 and Figure 40, while a full impression of the results, that also considers 3 and 7 days of curing time, are shown in the histograms of Figure 41. A first impression reveals that the compressive strength data shows a much more stable and consistent behavior than the bending ones (Figure 36 to Figure 38), while they are also characterized by a much lower scatter. Moreover, the general trend of the compressive strength results shows a consistent strength reduction with either enhancing volume substitution of N-MPCM employed in the system or increasing w/b ratios.

Furthermore, results for the reference pastes show higher compressive strength values for lower w/b ratios. Particularly, the strength increases from REF-0.45 to REF-0.40 is much more pronounced than from REF-0.40 to REF-0.33. In the first case, the rise is +25%, while in the second case, the strength increase is 2.5% only. Moreover, the incorporation of N-MPCM in the cementitious matrix mainly generates a decrease of the compressive strength, independently of the w/b ratio. For example, the substitution of N-MPCM with 20% to 40% generated a further strength loss of approximately 50% for each mixture.

The results in Figure 39 show for a 20% N-MPCM substitution nearly similar results for the w/b ratios of 0.45 and 0.40, while for the w/b ratio of 0.33 a +22% increase in average compressive strength was observed. Moreover, for a 40% N-MPCM substitution, the order of magnitude of the compressive strength values, independently of the w/b ratio, are within the same range, i.e., between 26.3 and 30.5 MPa. When comparing these results with the reference values fromFigure 39, it can be observed that a 20% N-MPCM substitution leads generally to a reduction of compressive strength: 33% for pastes with a w/b ratio of 0.45, 49% for pastes with a w/b ratio of 0.40 and 36% for pastes with a w/b ratio of 0.33, respectively.

Furthermore, the 40% N-MPCM substitution results in an additional 50% strength reduction when compared to the 20% N-MPCM substitution. By analysing Figure 39 and Figure 40, it can be also be observed that the replacement of cement paste by N-MPCM affects the compressive strength considerably more than the change of the w/b ratio.

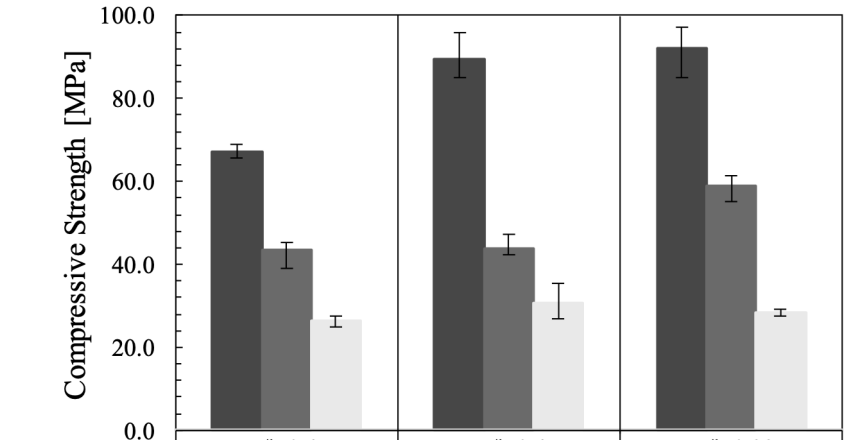

	w/b 0.45	w/b 0.4	w/b 0.33
REF	67.2	89.6	92.2
20% - MPCM	43.4	43.7	58.8
40% - MPCM	26.3	30.5	28.4

Figure 39. 28-days compressive strength values among different w/b ratios and comparing REF, 20% and 40% N-MPCM volume fraction in pastes.

The inherent impact of N-MPCM addition on the mechanical resistance has also been confirmed by various other authors in literature (see the critical review of [58]).

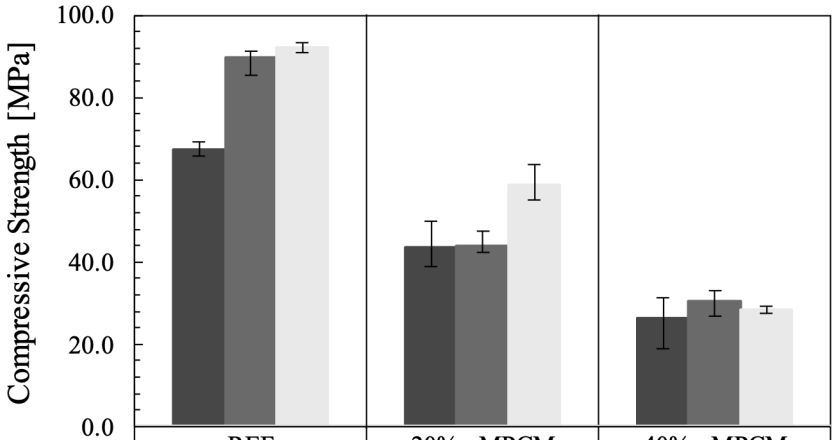

	REF	20% - MPCM	40% - MPCM
w/b 0.45	67.2	43.4	26.3
w/b 0.4	89.6	43.7	30.5
w/b 0.33	92.2	58.8	28.4

Figure 40. 28-days compressive strength values among different N-MPCM volume fractions and comparing w/b 0.45, w/b 0.40, and w/b 0.33 of pastes.

One of the potential reasons for the reduced compressive strength is the increase in porosity due to the N-MPCM addition. This was also stated for instance by Aguayo et al. [59] and was confirmed in this work as well (see Section 2.2.4.4). A complete overview of the measured compressive strength data, also considering the different maturation times of testing (i.e., 3 days, 7 days and 28 days), and the three different w/b ratios and N-MPCM volume substitutions, are reported in Figure 41.

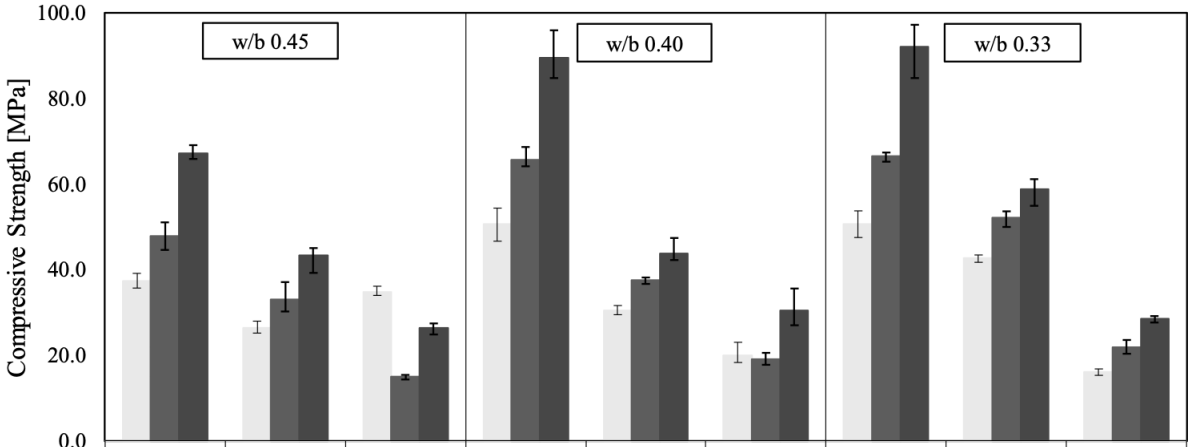

	REF - 0.45	20% - MPCM	40% - MPCM	REF - 0.40	20% - MPCM	40% - MPCM	REF - 0.33	20% - MPCM	40% - MPCM
3 days	37.3	26.4	34.7	50.6	30.5	19.9	50.7	42.7	16.0
7 days	47.8	32.9	14.8	65.8	37.4	19.0	66.5	52.2	21.9
28 days	67.2	43.4	26.3	89.6	43.7	30.5	92.2	58.8	28.4

Figure 41. Compressive strength values among different w/b ratios, for REF, 20% and 40% N-MPCM pastes and comparing 3, 7 and 28 days of curing time.

2.2.4.4 MIP porosity and pore structure

MIP results

The pore volume of the various cement pastes was determined by MIP tests on samples with a hydration time of 28 days. The effect of w/b ratio on the pore structure with and without N-MPCM addition is measured by means of the change in intruded volume and related pore size distributions. Figure 42 provides an overview of the results that have been obtained for various mixtures.

A detailed analysis of the data provided in Figure 42 reveals that increasing N-MPCM substitutions mainly leads to a higher porosity in the paste structure, indicating that the addition of microcapsules has a significant impact on the pore size/structure of cementitious systems. The latter results in lower mechanical strength and considerably affects heat/moisture transport mechanism through the cementitious system. Furthermore, when w/b decreases, the porosity tends to decrease for all pastes. It is interesting to note that the addition of 40% N-MPCM leads to a more stable pore structure regardless of the w/b ratio. In contrast, a much wider pore size distribution is seen for 20% N-MPCM. The critical pore size is clear for the case of 40% N-MPCM; however, the w/b appears to have a significant effect on the pore size of the system with w/b of 0.45 and 0.40, being very similar to each other and 0.33 being much lower.

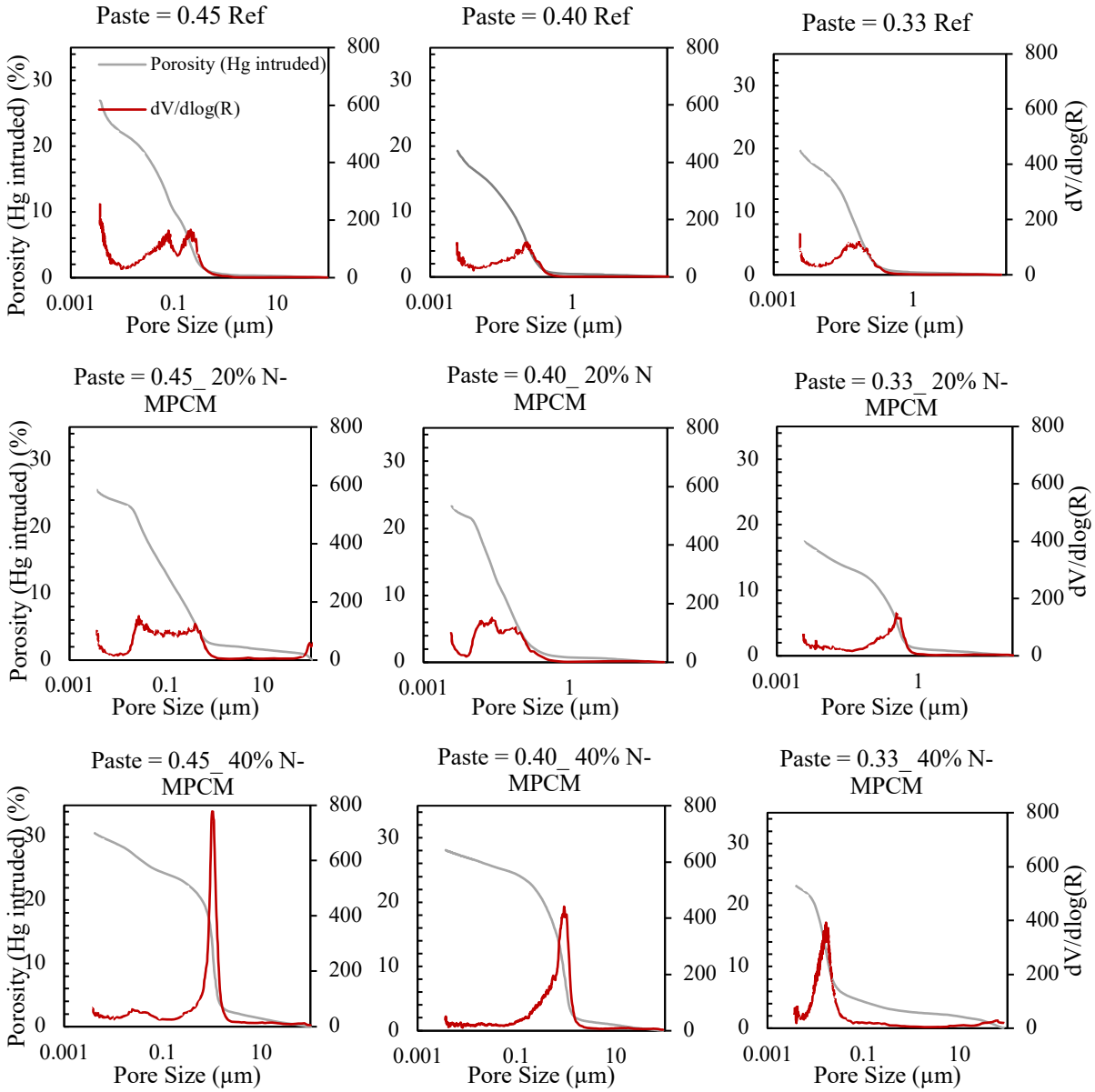

Figure 42. MIP results for REF, 20% and 40% N-MPCM pastes, and for different w/b ratios.

This is mainly because of the poor interface bond between the N-MPCM-shell and the cementitious matrix, especially for higher w/b ratios and because of the hydrophobic nature of the N-MPCM capsules, which will repel the water and cause air gaps between shell surface and cementitious matrix. An overview of the achieved results is given in Table 11.

Table 11. Overview of the sample porosities and critical pore diameter measurements via MIP.

	w/b = 0.45			w/b = 0.40			w/b = 0.33		
	Ref	20%	40%	Ref	20%	40%	Ref	20%	40%
Critical pore diameter (µm)	0.236	0.029	1.050	0.105	0.025	0.912	0.076	0.359	0.018
Intrudable porosity (%)	24.22	25.62	30.97	20.40	23.54	28.11	18.84	17.73	23.36

Among all prepared samples, the highest porosity (30.97 %) is measured for the mixtures with 40% N-MPCM and w/b=0.45, and the lowest porosity (17.73 %) for the samples with 20% N-MPCM and a w/b ratio of 0.33. The results indicate that the phenomena that may affect the porosity of cement paste with N-MPCM included, can be various. Firstly, the size of single microcapsules which might fill the cavities between the hydrating cementitious particles, leading to improved particle packing density and a decreasing porosity (see also [57]). This effect can also explain the lower porosity for samples with 20% N-MPCM and a w/b ratio of 0.33, when compared with the Ref-0.33. On the contrary, the hydrophobic nature of N-MPCM may contribute to a higher porosity as well. When microcapsules are added to a mixture, they tend to repel water, so air bubbles may adhere to a microcapsule, resulting in higher porosity in the cement paste mixtures. A third possible effect is the agglomeration of microcapsules in the cementitious system, which avoids an optimum packing density, and finally results in a higher porosity. The porosity of N-MPCM-enhanced cementitious systems can be explained and evaluated by a combined effect of these three possible causes.

Dependency between porosity, strength, and thermal properties

The dependency between the compressive strength (Section 2.2.4.3) and the porosity is elaborated in Figure 43-a for the various cement based mixtures with different w/b ratios and N-MPCM volumetric amounts.

The results show a clear linear trend with the porosity dominated by either the w/b ratio or the volumetric amount of N-MPCM. In this sense, it can be observed that the lowest compressive strength belongs to samples with 40% volumetric amount of N-MPCM which are clearly dominated by the highest porosity, and mainly affected by the % of cement paste replaced by N-MPCM. From Figure 43-b, a clear relationship between the thermal conductivity and porosity of the various cementitious mixtures can be observed. This also implicitly indicates a dependency between the compressive strength and the thermal conductivity.

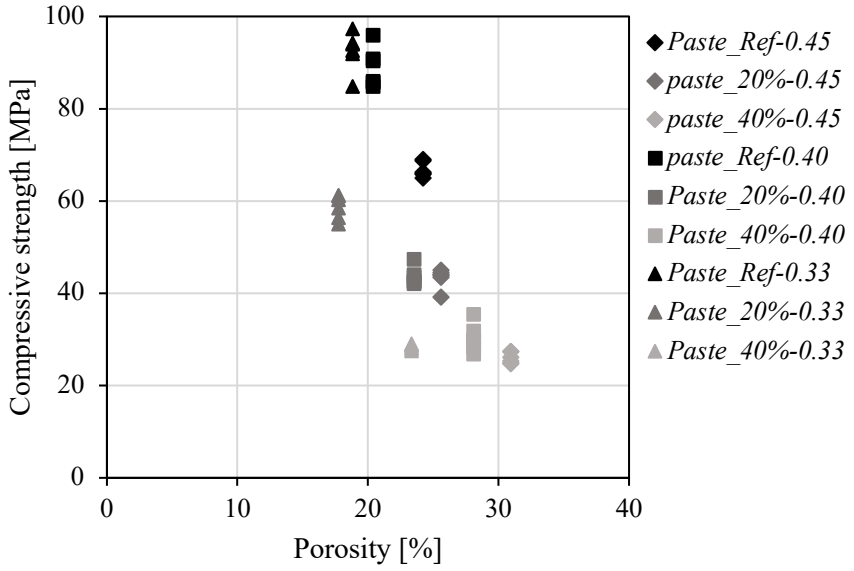

(a)

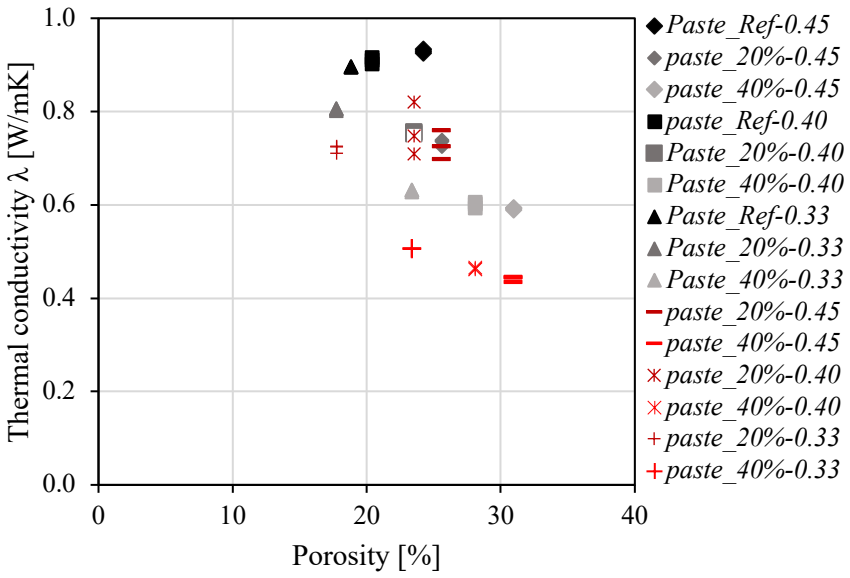

(b)

Figure 43. a) Compressive strength vs porosity and b) Thermal Conductivity vs porosity of REF, 20% and 40% N-MPCM-cement pastes. Black/grey points show the measured conductivity by 25 °C and red points show the measured conductivity by 45°C.

The change in porous microstructure of N-MPCM-cementitious systems is thus directly linked to a change in thermal conductivity, or to a change of the compressive strength. These results reveal the important role that the inner pores (amount and structure) play especially when optimum thermal, mechanical and/or TES properties are considered. From the results shown in Figure 43, it is evident that the pastes with the same % of N-MPCM are characterized to have a very similar thermal conductivity, independently of the w/b ratio.

2.2.4.5 Morphological and elemental analysis via SEM

The morphological analysis of the sample surfaces was investigated with a SEM characterization technique with the aim to study the N-MPCM microcapsules and their integrity in cement paste microstructures. The results are presented in this section.

Reference pastes

Figure 44 provides the microstructure of the various cementitious paste samples without N-MPCM, indicating the effect of the employed w/b ratios on the microstructure morphology. The presence of micro cracks caused by hardening shrinkage is evident for all samples. In all mixtures, the dispersion of a lighter phase (blue arrow) and a slightly darker phase (yellow arrow), indicate the various binder material in the cementitious system. To identify the composition of these phases, an elemental analysis with EDS was performed as shown in Figure 45.

With consideration of the chemical composition of cement and metakaolin provided in Section 2.2.2.1, the obtained EDS maps can be employed to characterize the individual elements. Firstly, the lighter phases are associated with anhydrous cement elements, represented by higher concentrations of calcium (Ca) and silica

(Si). Secondly, the concentration of iron (Fe) confirms further anhydrous hydration products (more precisely, ferrite), indicated by a slightly brighter color. Lastly, the presence of both silica (Si) and aluminum (Al), indicate the presence of metakaolin that contains both these elements. The rest of the paste contains various hydration products among which C-S-H and CH.

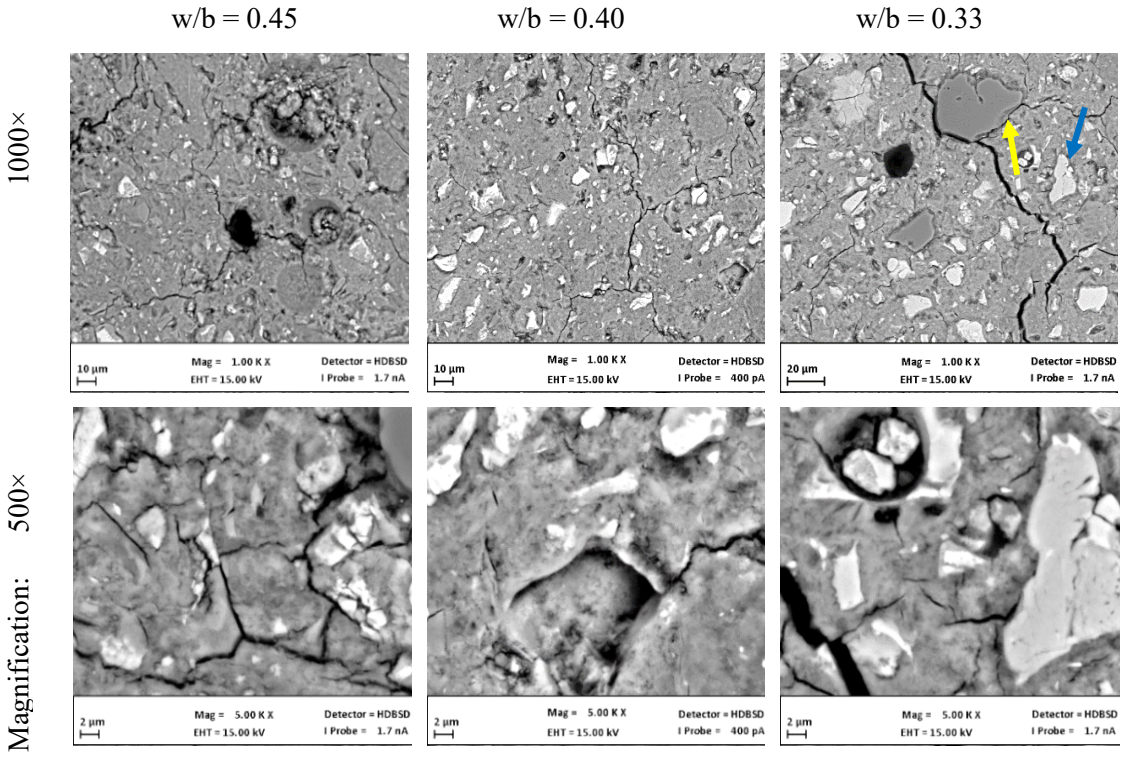

Figure 44. SEM micrographs of the reference pastes and considering different w/b ratios.

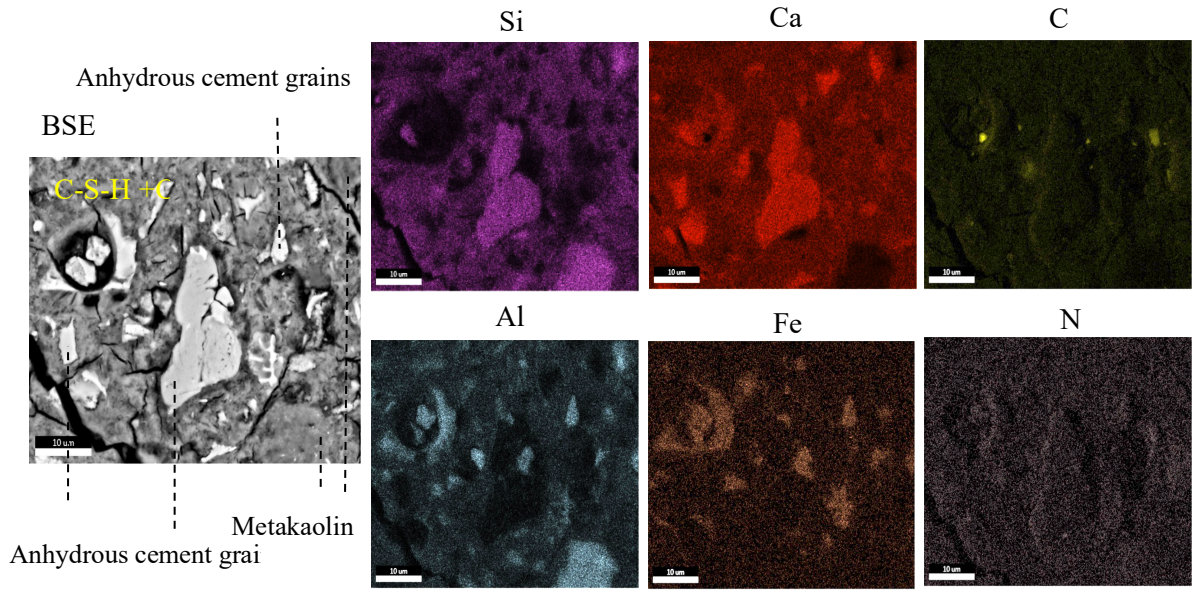

Figure 45. SEM-EDS mapping of the w/b=0.33 reference pastes providing the distribution of chemical components available in the composite.

Elemental analysis of N-MPCM in the cementitious matrix

When considering the expected chemical composition of N-MPCM with a polymeric shell (made from the polymerization of formaldehyde, with the chemical formula CH2O, and melamine with the chemical formula C3H6N6), the presence of carbon (C) and nitrogen (N) was also examined.

Since the N-MPCM contains carbon in its shell composition, it is not recommended to treat the surface of N-MPCM-composite with the epoxy impregnation technique to simplify N-MPCM detection. Finally, small amounts of distributed nitrogen were also observed that can most likely be attributed to the SEM N-filled vacuum chamber. An EDS analysis was carried out for the N-MPCM pastes, where Figure 46 shows the evaluation of the N-MPCM distribution in the cement paste. The Figure only shows the micrographs for a w/b ratio of 0.33 and 0.45, both with a 40% N-MPCM content. The full elementary analysis confirmed a similar distribution for all cases.

The SEM micrographs show an equally distribution of the N-MPCM in the cement-paste matrix (indicated in Figure 46). It can also be observed that the microcracks propagate mostly across the spherical voids without harming N-MPCM microcapsules. The soft organic polymer shell of the N-MPCM microcapsule clearly presents the weakest element among the inorganic constituents inside the cement-paste matrices. In this sense, these N-MPCM particles act as a crack initiator.

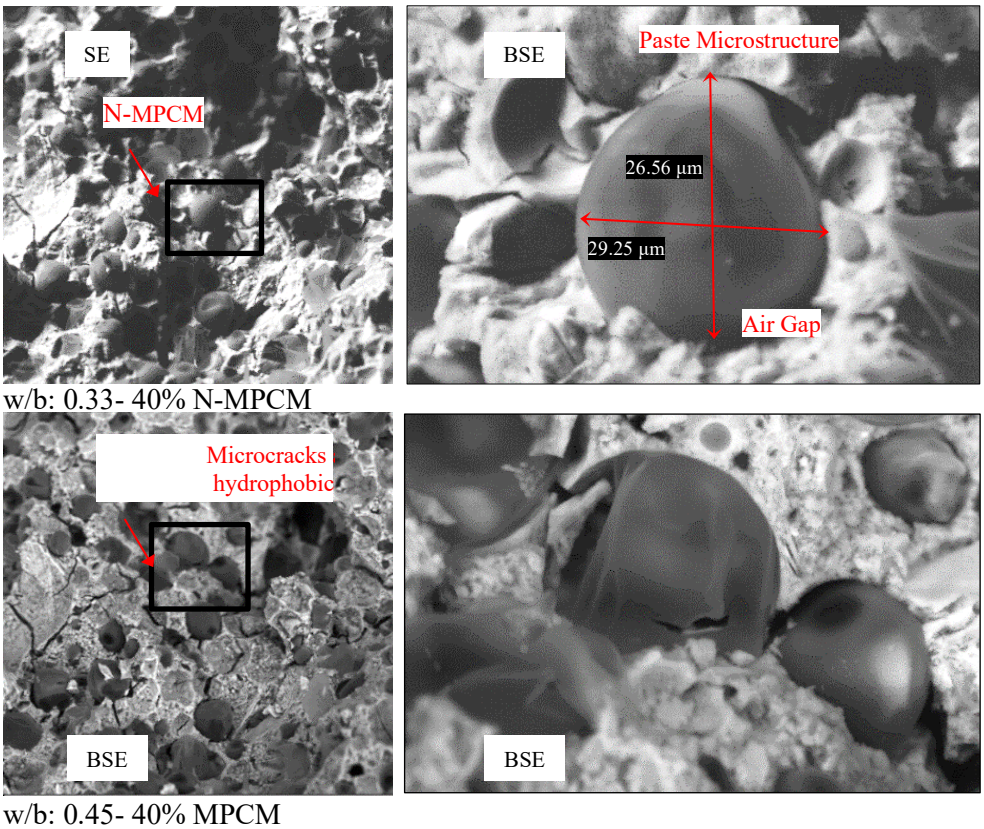

Figure 46. SEM micrograph of N-MPCM for a w/b ratio of 0.33 and 0.45, both with a 40% N-MPCM content in the paste. The amplification shows detailed views of the N-MPCM distribution in the cement paste matrix.

A closer look on the compatibility of the cement matrix with N-MPCM reveals the presence of possible gaps between the shell interface and the cement-paste matrices. The hydrophobic nature of N-MPCM shell, which repels water, cause the air entrapment between the capsules and the cement paste. By using the BSE detector for the same spot and magnification as the SE detector, more information on the presence of N-MPCM could be obtained for unpolished samples. As one of the goals was to determine the state of the capsule, the BSE detector was used to take a closer look at 5000× of magnification.

N-MPCM appearance was partly affected by the polishing treatment to prepare samples for SEM-EDS analysis. In contrast, the shape and adhesion of the N-MPCM to the matrix, as well as the presence of a crack in a shell, were easier to identify in unpolished samples. As a result, the SEM-EDS study on the N-MPCM-composites was conducted on unpolished samples as shown in Figure 46.

The evaluation of the element composition for a N-MPCM capsule was also performed. Figure 47 shows the element mapping of N-MPCM, which provides a back-scattered image (BSE) and a graphical distribution of the analyzed chemical elements i.e., Carbon (C) and Nitrogen (N). The SEM analysis of the N-MPCM particles, embedded in the cement paste matrix, confirms the presence of a single capsule by its high concentration of both carbon (C) and nitrogen (N).

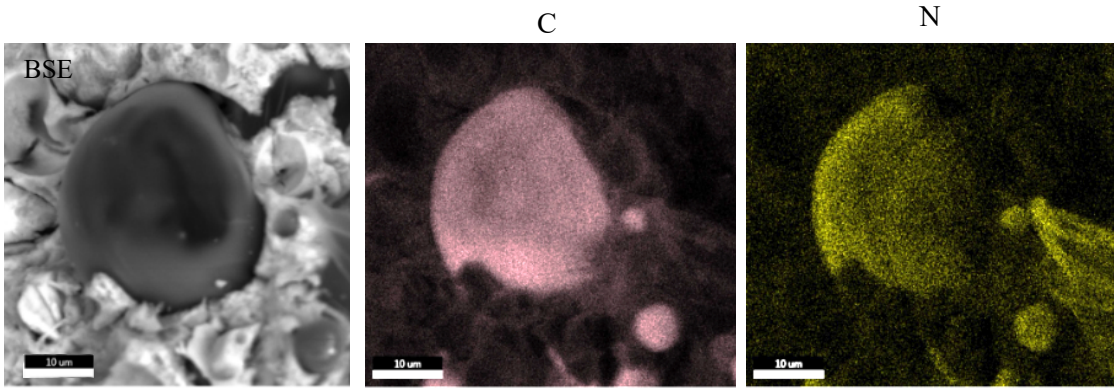

Figure 47. SEM-EDS mapping of the N-MPCM providing a detailed back-scattered image (BSE), a distribution of carbon (C) and nitrogen (N).

The relationship between the amounts of each compound can be compared and evaluated based on the amount of oxides present. Therefore, the calculated chemical composition for the polymer shell based on the C/O ratio is 0.847, compared to the ratio of 0.179 for N/O. This reveals that the shell is mainly composed of carbon with a smaller amount of nitrogen, which complies with the basic formulation of melamine-formaldehyde ($C_3H_6N_6$).

2.2.5 Conclusions

This work is reporting the results and analysis of an extensive experimental study on cement paste enhanced with Nextek 37D®-Microencapsulated Phase Change Materials (N-MPCM) for Thermal Energy Storage (TES) purposes. Three different water-to-binder ratios (0.45, 0.40 and 0.33) and two N-MPCM volume fractions (20% and 40%, plus a 0% reference mix) were investigated.

Based on the experimental results, the following conclusions can be drawn:

- Particle size of N-MPCM was investigated through size diffractometer measurements which indicated a mean particle size of 20.9 μm, with a low tendency to agglomerate.
- The wettability of the N-MPCM was assessed via contact angle measurements. The test was performed with 10 times repetitions and results showed an average contact angle of 110.7 º, confirming the hydrophobic nature of the considered microcapsules.
- DSC-measurements on N-MPCM were conducted with a heating/cooling rate of 0.5 $K \times min^{-1}$. The experimental data showed a melting peak temperature of 36.5 °C, and 31.7 °C for the solidification one. The latent heat was 197.3 J/g and 194.6 J/g for heating and cooling, respectively.
- DSC results of the composites (i.e., REF pastes and MPMC pastes) showed an almost similar sensible heat capacity for the cement pastes with different w/b ratios and without N-MPCM. For the pastes enhanced with N-MPCM substitutions, evident latent peaks were recorded in the temperature region where the phase change occurred (either in melting or solidification stage). The volumetric latent enthalpies showed an almost constant average of 20-25 (MJ/m^3) for samples with 20% N-MPCM and 55-60 (MJ/m^3) for samples with 40% N-MPCM, independent of the w/b ratio.
- Thermal conductivities were studied by Hot-Disk measurements to assess the influence of the w/b ratio and the amount of MPMC substituted. The experimental results showed a decreasing thermal conductivity for higher w/b ratios and/or when the N-MPCM volume fractions are higher. Thermal conductivity values were measured at 25 and 45 °C which values ranged between 0.93 to 0.44 W/m×K: N-MPCM amounts and w/b ratios play the major roles in the conductivity loss.
- Compressive and bending tests, conducted at different times of hydration, showed a strength loss trend which can be due to either increasing w/b ratio and/or increasing amount of N-MPCM substitution. Strength loss due to N-MPCM addition could be explained by several concurring factors such as the low mechanical strength of N-MPCM shells, the weak interface bond strength between the cement matrix and N-MPCM, and the increase of the porosity of the N-MPCM-cement paste matrix.
- MIP tests were performed to characterize the pore structure after 28 days of hydration. Pore size distribution and total intruded porosity, for different w/b ratios and volumetric amount of N-MPCM, were investigated. The results showed that an increase of the N-MPCM substitutions lead to a higher porosity in the cement paste. Moreover, the w/b ratio also showed a significant effect on the pore size distribution of all tested cement paste systems. The highest porosity (30.97 %) was measured for the mixture with 40% N-MPCM and a w/b=0.45, while the lowest porosity (17.73 %) was measured on samples with 20% N-MPCM and a w/b of 0.33.
- Scanning Electron Microscopy (SEM) analyses was performed to investigate the microscopic properties and to examine the distribution of chemical components (via SEM-EDS) present in the cement paste matrix. Chemical compositions, geometry, shape, particle size, and particle distribution were investigated for both plain cement paste and N-MPCM-paste systems. The results showed a

homogeneous distribution of N-MPCM, a proper shell integrity, envisioned various particle sizes and uniformity of microcapsules, confirmed mechanical stability and gave a clear impression N-MPCM have on the microstructure morphology and chemistry of the cementitious composites.

References

[1] Tian, C., Feng, G., Li, S., & Xu, F. (2019). Scenario analysis on energy consumption and CO2 emissions reduction potential in building heating sector at community level. Sustainability, 11(19), 5392.

[2] Heating and cooling | EASME, https://ec.europa.eu/easme/en/section/horizon-2020-energy-efficiency/heating-and cooling#inline-nav-1, last accessed 28/04/2021.

[3] Ürge-Vorsatz, D., Cabeza, L. F., Serrano, S., Barreneche, C., & Petrichenko, K. (2015). Heating and cooling energy trends and drivers in buildings. Renewable and Sustainable Energy Reviews, 41, 85-98.

[4] https://ec.europa.eu/info/strategy/priorities-2019-2024/european-green-deal_en

[5] Baniasadi, A., Habibi, D., Al-Saedi, W., Masoum, M. A., Das, C. K., & Mousavi, N. (2020). Optimal sizing design and operation of electrical and thermal energy storage systems in smart buildings. Journal of Energy Storage, 28, 101186.

[6] Tang, R., & Wang, S. (2019). Model predictive control for thermal energy storage and thermal comfort optimization of building demand response in smart grids. Applied Energy, 242, 873-882.

[7] Zavrl, E., & Stritih, U. (2019). Improved thermal energy storage for nearly zero energy buildings with PCM integration. Solar energy, 190, 420-426.

[8] Tyagi, V. V., Chopra, K., Kalidasan, B., Chauhan, A., Stritih, U., Anand, S., ... & Kothari, R. (2021). Phase change material based advance solar thermal energy storage systems for building heating and cooling applications: A prospective research approach. Sustainable Energy Technologies and Assessments, 47, 101318.

[9] Gholamibozanjani, G., & Farid, M. (2020). A comparison between passive and active PCM systems applied to buildings. Renewable Energy, 162, 112-123.

[10] Saxena, R., Rakshit, D., & Kaushik, S. C. (2020). Experimental assessment of Phase Change Material (PCM) embedded bricks for passive conditioning in buildings. Renewable Energy, 149, 587-599.

[11] Maleki, B., Khadang, A., Maddah, H., Alizadeh, M., Kazemian, A., & Ali, H. M. (2020). Development and thermal performance of nanoencapsulated PCM/plaster wallboard for thermal energy storage in buildings. Journal of Building Engineering, 32, 101727.

[12] Bentz, D. P., Peltz, M. A., Duran-Herrera, A., Valdez, P., & Juarez, C. A. (2011). Thermal properties of high-volume fly ash mortars and concretes. Journal of Building Physics, 34(3), 263-275.

[13] Srinivasaraonaik, B., Sinha, S., & Singh, L. P. (2021). Synthesis of encapsulation of binary mixture by silica and its performance in pure cementitious system. Energy Storage, 3(3), e229.

[14] Nazari Sam, M., Caggiano, A., Mankel, C., & Koenders, E. (2020). A comparative study on the thermal energy storage performance of bio-based and paraffin-based PCMs using DSC procedures. Materials, 13(7), 1705.

[15] Stritih, U., Tyagi, V. V., Stropnik, R., Paksoy, H., Haghighat, F., & Joybari, M. M. (2018). Integration of passive PCM technologies for net-zero energy buildings. Sustainable cities and society, 41, 286-295.

[16] Lin, Y., Jia, Y., Alva, G., & Fang, G. (2018). Review on thermal conductivity enhancement, thermal properties and applications of phase change materials in thermal energy storage. Renewable and sustainable energy reviews, 82, 2730-2742.

[17] Pandey, A. K., Hossain, M. S., Tyagi, V. V., Abd Rahim, N., Jeyraj, A., Selvaraj, L., & Sari, A. (2018). Novel approaches and recent developments on potential applications of phase change materials in solar energy. Renewable and Sustainable Energy Reviews, 82, 281-323.^

[18] Tyagi, V. V., Chopra, K., Sharma, R. K., Pandey, A. K., Tyagi, S. K., Ahmad, M. S., ... & Kothari, R. (2022). A comprehensive review on phase change materials for heat storage applications: Development, characterization, thermal and chemical stability. Solar Energy Materials and Solar Cells, 234, 111392.

[19] Ramakrishnan, S., Sanjayan, J., Wang, X., Alam, M., & Wilson, J. (2015). A novel paraffin/expanded perlite composite phase change material for prevention of PCM leakage in cementitious composites. Applied Energy, 157, 85-94.

[20] Hawlader, M. N. A., Uddin, M. S., & Khin, M. M. (2003). Microencapsulated PCM thermal-energy storage system. Applied energy, 74(1-2), 195-202.

[21] Konuklu, Y., Ostry, M., Paksoy, H. O., & Charvat, P. (2015). Review on using microencapsulated phase change materials (PCM) in building applications. Energy and Buildings, 106, 134-155.

[22] Regin, A. F., Solanki, S. C., & Saini, J. S. (2009). An analysis of a packed bed latent heat thermal energy storage system using PCM capsules: Numerical investigation. Renewable energy, 34(7), 1765-1773.

[23] Adesina, A. (2019). Use of phase change materials in concrete: current challenges. Renewable Energy and Environmental Sustainability, 4, 9.

[24] Hawlader, M. N. A., Uddin, M. S., & Khin, M. M. (2003). Microencapsulated PCM thermal-energy storage system. Applied energy, 74(1-2), 195-202.

[25] Farid, M. M., Khudhair, A. M., Razack, S. A. K., & Al-Hallaj, S. (2004). A review on phase change energy storage: materials and applications. Energy conversion and management, 45(9-10), 1597-1615.

[26] Ren, M., Wen, X., Gao, X., & Liu, Y. (2021). Thermal and mechanical properties of ultra-high performance concrete incorporated with microencapsulated phase change material. Construction and Building Materials, 273, 121714.

[27] Ricklefs, A., Thiele, A. M., Falzone, G., Sant, G., & Pilon, L. (2017). Thermal conductivity of cementitious composites containing microencapsulated phase change materials. International journal of heat and mass transfer, 104, 71-82.

[28] Mankel, C., Caggiano, A., Ukrainczyk, N., & Koenders, E. (2019). Thermal energy storage characterization of cement-based systems containing microencapsulated-PCMs. Construction and Building Materials, 199, 307-320.

[29] Gencel, O., Yaras, A., Hekimoğlu, G., Ustaoglu, A., Erdogmus, E., Sutcu, M., & Sarı, A. (2022). Cement based-thermal energy storage mortar including blast furnace slag/capric acid shape-stabilized phase change material: Physical, mechanical, thermal properties and solar thermoregulation performance. Energy and Buildings, 111849.

[30] Hekimoğlu, G., Nas, M., Ouikhalfan, M., Sarı, A., Kurbetci, Ş., Tyagi, V. V., ... & Saleh, T. A. (2021). Thermal management performance and mechanical properties of a novel cementitious composite containing fly ash/lauric acid-myristic acid as form-stable phase change material. Construction and Building Materials, 274, 122105.

[31] Sarı, A., Hekimoğlu, G., Tyagi, V. V., & Sharma, R. K. (2020). Evaluation of pumice for development of low-cost and energy-efficient composite phase change materials and lab-scale thermoregulation performances of its cementitious plasters. Energy, 207, 118242.

[32] Sarı, A., Bicer, A., Karaipekli, A., & Al-Sulaiman, F. A. (2018). Preparation, characterization and thermal regulation performance of cement based-composite phase change material. Solar energy materials and solar cells, 174, 523-529.

[33] Amran, Y. M., Farzadnia, N., & Ali, A. A. (2015). Properties and applications of foamed concrete; a review. Construction and Building Materials, 101, 990-1005.

[34] Xu, B., & Li, Z. (2013). Paraffin/diatomite composite phase change material incorporated cement-based composite for thermal energy storage. Applied energy, 105, 229-237.

[35] Ramakrishnan, S., Sanjayan, J., Wang, X., Alam, M., & Wilson, J. (2015). A novel paraffin/expanded perlite composite phase change material for prevention of PCM leakage in cementitious composites. Applied Energy, 157, 85-94.

[36] Rathore, P. K. S., Shukla, S. K., & Gupta, N. K. (2020). Potential of microencapsulated PCM for energy savings in buildings: A critical review. Sustainable Cities and Society, 53, 101884.

[37] Lu, S., Li, Y., Kong, X., Pang, B., Chen, Y., Zheng, S., & Sun, L. (2017). A review of PCM energy storage technology used in buildings for the global warming solution. Energy Solutions to Combat Global Warming, 611-644.

[38] Snoeck, D., Priem, B., Dubruel, P., & De Belie, N. (2016). Encapsulated Phase-Change Materials as additives in cementitious materials to promote thermal comfort in concrete constructions. Materials and structures, 49(1), 225-239.

[39] Aguado, A., Fernández, A. I., Cabeza, L. F., & Chimenos, J. M. (2014). Review of the use of phase change materials (PCMs) in buildings with reinforced concrete structures. Mater. Construcc, 64(315), e031.

[40] Cao, V. D., Pilehvar, S., Salas-Bringas, C., Szczotok, A. M., Do, N. B. D., Le, H. T., ... & Kjøniksen, A. L. (2018). Influence of microcapsule size and shell polarity on the time-dependent viscosity of geopolymer paste. Industrial & Engineering Chemistry Research, 57(29), 9457-9464.

[41] Coppola, L., Coffetti, D., & Lorenzi, S. (2016). Cement-based renders manufactured with phase-change materials: applications and feasibility. Advances in Materials Science and Engineering, 2016.

[42] Sanfelix, S. G., Santacruz, I., Szczotok, A. M., Belloc, L. M. O., Angeles, G., & Kjøniksen, A. L. (2019). Effect of microencapsulated phase change materials on the flow behavior of cement composites. Construction and Building Materials, 202, 353-362.

[43] Meshgin, P., & Xi, Y. (2012). Effect of Phase-Change Materials on Properties of Concrete. ACI Materials Journal, 109(1).

[44] Dehdezi, P. K., Hall, M. R., Dawson, A. R., & Casey, S. P. (2013). Thermal, mechanical and microstructural analysis of concrete containing microencapsulated phase change materials. International Journal of Pavement Engineering, 14(5), 449-462.

[45] Fernandes, F., Manari, S., Aguayo, M., Santos, K., Oey, T., Wei, Z., ... & Sant, G. (2014). On the feasibility of using phase change materials (PCMs) to mitigate thermal cracking in cementitious materials. Cement and Concrete Composites, 51, 14-26.

[46] PN-EN 197-1 “Cement. Part 1. Composition, specifications and conformity criteria for common cements”.

[47] Centrilit NC II Concrete Additive Based on Pozzolanic Alumosilicate, https://www.mc-bauchemie.hr/docs/technical/Centrilit_NC_II.pdf

[48] Microtech Laborathories, 2019. [Online]. Available: https://www.microteklabs.com-/nextek-37d.

[49] EN 196-1, 'Methods of Testing Cement – Part 1: Determination of Strength', (2005).

[50] Liu, X., Hu, S., Tang, Y., Xie, Z., Liu, J., & He, Y. (2020). Selecting a proper microsphere to combine optical trapping with microsphere-assisted microscopy. Applied Sciences, 10(9), 3127.

[51] Hebbar, R. S., Isloor, A. M., & Ismail, A. F. (2017). Contact angle measurements. In Membrane characterization (pp. 219-255). Elsevier.

[52] DIN 51005. 2005. Thermal analysis (TA) - Terms.

[53] DIN 51007. 2019. Thermal analysis – Differential thermal analysis (DTA) and differential scanning calorimetry (DSC) –General Principles.

[54] IEA-SHC 42 / ECES Annex 29. 2015. Standard to determine the heat storage capacity of PCM using hf-DSC with constant heating/cooling rate (dynamic mode). A technical report of subtask A2.1.

[55] International Standard, “Pore size distribution and porosity of solid materials by mercury porosimetry and gas adsorption. Mercury Porosimetry (ISO 15901),” ISO 15901, 2006.

[56] Anovitz, L. M., & Cole, D. R. (2015). Characterization and analysis of porosity and pore structures. Reviews in Mineralogy and geochemistry, 80(1), 61-164.

[57] Cao, V. D., Pilehvar, S., Salas-Bringas, C., Szczotok, A. M., Rodriguez, J. F., Carmona, M., ... & Kjøniksen, A. L. (2017). Microencapsulated phase change materials for enhancing the thermal performance of Portland cement concrete and geopolymer concrete for passive building applications. Energy Conversion and Management, 133, 56-66.

[58] Marani, A., & Nehdi, M. L. (2019). Integrating phase change materials in construction materials: Critical review. Construction and Building Materials, 217, 36-49.

[59] Aguayo, M., Das, S., Maroli, A., Kabay, N., Mertens, J. C., Rajan, S. D., ... & Neithalath, N. (2016). The influence of microencapsulated phase change material (PCM) characteristics on the microstructure and strength of cementitious composites: Experiments and finite element simulations. Cement and Concrete Composites, 73, 29-41.

2.3 Modelling porous cementitious media with/without integrated latent heat storage: application scenario

This chapter is published in: Energies, 16(18), 6687, Nazari Sam, M., Schneider, J., & Lutze, H. V. (2023). Modelling Porous Cementitious Media with/without Integrated Latent Heat Storage: Application Scenario. Author Contributions: Conceptualization, M.N.S.; Methodology, M.N.S.; Validation, M.N.S.; Formal analysis, M.N.S.; Investigation, M.N.S.; Data curation, M.N.S.; Writing—original draft, M.N.S.; Writing—review & editing, M.N.S., J.S. and H.L.; Visualization, M.N.S.; Supervision, J.S. and H.L.; Funding acquisition, J.S. and H.L. All authors have read and agreed to the published version of the manuscript.

2.3.1 Introduction

The built environment is responsible for over 30% of global energy consumption and contributes nearly 40% of total direct and indirect greenhouse gas emissions [1–3]. In this context, the use of thermal energy storage (TES) technologies and latent-heat thermal energy storage (LHTES) systems has an enormous potential for novel applications in buildings [4–6]. Utilizing phase-change materials (PCMs), one of the most effective methods for increasing the latent heat storage in buildings, offers viable solutions for improving energy efficiency, enhancing the performance of HVAC and on-site renewable energy systems, i.e., reducing peak loads, maintaining indoor comfort levels, regulating temperature excursions, and attenuating extreme thermal values [7–11].

Over the past few years, numerous articles have been dedicated to exploring the use of PCMs in construction and building materials [12–14]. More specifically, the ability to store and release large amounts of heat into PCMs mixed within insulating envelopes can effectively reduce the thermal conditioning load of the building [15–24]. In this context, a significant proportion of the research on PCMs focuses on their incorporation into porous cementitious or other binder-based composites (i.e., having a density <800 kg/m^3) to be used for thermal insulation in nearly-zero-energy buildings (NZEBs) [25–28]. These composites can provide excellent heat blocks and are non-flammable [29,30]. However, the thermophysical properties of cementitious foams largely depend on the microstructural parameters, including air content as well as inner pore morphology and the amount/type of binders, aggregates, and, eventually, additional components like fillers, fibers, or rubber particles [31–38]. The correlation between microstructural parameters and related thermophysical properties of porous cementitious composites has been the object of extensive study for many decades due to its wide applicability in engineering problems and applications.

From the modelling point of view, on one hand, several theoretical and empirical models have been proposed in the literature to deal with describing the conductivity (either thermal or electrical) of composites. In this context, the most popular expressions are those due to the proposals by Maxwell [39–42] and Bruggeman [43–46]. They are often based on expressions providing the effective conductivity of a homogenized composite, and built up by combining the conductivity of the multi-phase components, such as the matrix, fillers, air-voids, fibers, etc. The weighting parameters in these formulas are commonly determined by either

the volumetric or the weight fraction of each individual phase. However, the influence of the pores (i.e., amounts, sizes, and distributions) on the heat-transfer properties of porous materials represents the key factor in this field [47]. Specifically, the thermal conductivity of two-phase porous systems has been reported to be strongly influenced by their pore nature and structure [48,49]. In this field, it is worth mentioning the proposal by Lewis and Nielsen [50,51], which most closely matches the transport parameters in two-phase porous systems in different cases [52–56].

On the other hand, modelling the heat storage capacity of porous cementitious systems enhanced with LHTES components has been largely explored in the literature. Most of the models arise from solving the so-called Stefan problem for phase transformation problems [57–59]. However, in construction and building materials applications, the problem can be highly simplified, and the so-called enthalpy-based method, employable for conduction-only mechanisms, represents the most used and simplified approach followed by many authors [60–65].

This study aims to propose a simplified analytical approach for predicting the homogenized thermal conductivity of porous cementitious media. A wide range of experimental data from the literature regarding the microstructure parameters of cement-based foams influencing thermal conductivity has been compiled. The links between air inclusions and fractions, geometrical classification of the pores, and the overall homogenized thermal conductivity k_{eff} of porous cementitious foams are established. The proposed analytical model concerns the stochastic characteristic of the pore structure and allows the prediction of the homogenized thermal conductivity of cementitious foams considering the shape and packing of the pores. The methodology can be further applied to solve the energy transport equations through the complex structure of mineral foams, with/without LHTES components, without the need for costly experimental designs or expensive computer analysis for ascertaining k_{eff} [66].

The present paper is structured as follows. Section 2 provides a summary of the available experimental data in the recent literature related to low-, medium-, and high-porosity cementitious media. In Section 3, the theoretical background of the Lewis–Nielsen model is discussed, including its assumptions, applicability, and further extension of the law. Section 4 presents the analytical predictions and comparisons relative to the experimental data to assess the soundness and capabilities of the methodology. Section 5 analyzes the TES (latent and sensible) performance of the studied composites, e.g., in 1D wall systems, while also examining the direct impacts of dynamic insulation parameters and the variable effusivity and diffusivity of the media. Finally, Section 6 concludes with the main remarks and provides future research directions.

2.3.2 Experimental Database

Experimental tests on variable porous cementitious systems have been employed as a reference database to show the potential and capability of the proposed modelling procedure described within Sections 2.3.3 and 2.3.4. This section reviews and analyzes a series of data available in the literature; the data cover the entire density (porosity) range, from low densities (porosities) up to high densities (porosities). The data are those tested by Batool (2015) [67], Awang et al. (2012) [68], Wei et al. (2013) [69], Mydin (2011) [70], Davraz et

al. (2016) [71], Oren et al. (2020) [72], and Jiang et al. (2017) [73] & (2016) [74]; see Supplementary Material S1 for more details.

All data collected in Table 12 are highlighting the types of binders used, possible additives/fillers, target densities ρ, water-to-binder ratios, dry densities ρ, measured conductivity values of cementitious matrices/skeleton (either pastes or mortars), dispersed air content (porosity), type of foaming agent employed, methods of foaming, and measurement methods for the foam conductivity, as well as how all of these factors are affecting the overall conductivity of the foam system (last column of the table). The review of these data, as listed in Table 12, reveals that the use of different pozzolanic additives/fillers into the matrix can affect the porosity and the related properties of the foam, and generally leads to a reduction of the thermal conductivity of the composite.

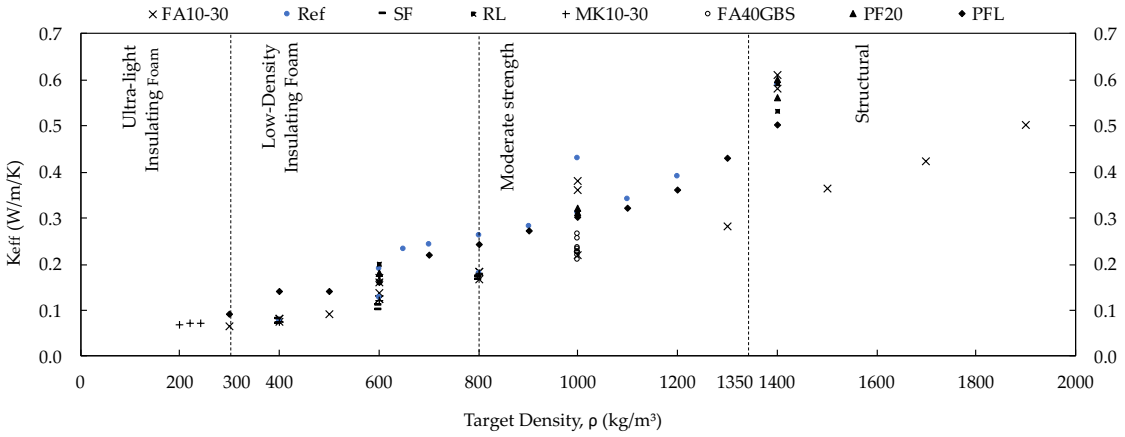

Figure 48. K_{eff} (W/m/K) vs. target density, ρ (kg/m^3) of concrete foams by [67–74]. Ref: Reference foam, FA: Fly ash, SF: Silica fume, RL/L: Limestone, MK: Metakaolin, GBS: Granulated blast furnace slag, PF: Polypropylene fiber.

Figure 48 provides a plot of the effective conductivity, k_{eff} (W/m/K), as a function of target density (kg/m^3), thus summarizing the foams' results with different concentrations of additives and fillers, as collected from experimental datasets. Besides the different types of components and materials employed, Figure 48 depicts a clear increase in the overall thermal conductivity, with an increase in density in all the experiments. The results have been presented in four different foam classes, as described in [75,76]: insulating ultra-lightweight (UL) foams having 0–300 kg/m^3 density; insulating low-density foams, with 300–800 kg/m^3 density; moderate strength foams with 800–1350 kg/m^3 density; and structural foams with densities higher than or equal to 1350 kg/m^3 density.

Table 12. Experimental database of foam concrete by [67–74].

Authors	Binder Type	Additive/ Filler	W/b Ratio	Target Density ρ (kg/m³)	Dry Density ρ (kg/m³)	Matrix Conductivity (k/W/m)	dispersed Air Content ε	Foaming Agent	Foaming Method	Conductivity Measurnment Method	Foam Conductivity (k/W/m)
Batool, F. (2015). [1]	HE portland cement	Ref	0,69	800	724	0,458	0,49	Synthetic	Physical air-entraining	Transient plane source (TPS)	0,180
				600	492	0,458	0,64				0,125
				400	303	0,458	0,78				0,076
		FA10		800	751	0,458	0,50				0,183
				600	549	0,458	0,62				0,136
				400	360	0,458	0,76				0,081
		FA20		800	710	0,407	0,50				0,182
				600	499	0,407	0,64				0,122
				400	273	0,407	0,81				0,074
		SF10		800	755	0,415	0,50				0,173
				600	499	0,415	0,65				0,111
				400	320	0,415	0,78				0,079
		SF20		800	750	0,416	0,53				0,166
				600	474	0,416	0,70				0,100
				400	270	0,416	0,83				0,071
		MK10		800	759	0,456	0,50				0,176
				600	529	0,456	0,65				0,119
				400	295	0,456	0,81				0,074
		MK20		800	756	0,461	0,51				0,179
				600	533	0,461	0,65				0,121
				400	276	0,461	0,82				0,074
Awang, H. et al. (2012).[2]	SEMI Portland cement/sand (1:1.5)	RefSa	0,45	600	n.a.	1,400	0,69	Protein-based	Physical air-entraining	Transient plane source (TPS)	0,190
				1000	n.a.	1,400	0,49				0,430
				1400	n.a.	1,400	0,36				0,590
		FA15		600	n.a.	n.a.	0,69				0,170
		FA30		600	n.a.	n.a.	0,70				0,160
		RL15		600	n.a.	n.a.	0,72				0,160
		RL30		600	n.a.	n.a.	0,70				0,200
		PF20		600	n.a.	n.a.	0,70				0,180
		PF40		600	n.a.	n.a.	0,71				0,180
		FA15		1000	n.a.	n.a.	0,50				0,380
		FA30		1000	n.a.	n.a.	0,51				0,360
		RL15		1000	n.a.	n.a.	0,56				0,310
		RL30		1000	n.a.	n.a.	0,55				0,310
		PF20		1000	n.a.	n.a.	0,54				0,310
		PF40		1000	n.a.	n.a.	0,55				0,320
		FA15		1400	n.a.	n.a.	0,35				0,580
		FA30		1400	n.a.	n.a.	0,35				0,610
		RL15		1400	n.a.	n.a.	0,36				0,590
		RL30		1400	n.a.	n.a.	0,37				0,530
		PF20		1400	n.a.	n.a.	0,36				0,600
		PF40		1400	n.a.	n.a.	0,35				0,560
Wei, S. et al. (2013). [3]	CEM I	FA20	0,40	1900	1870	0,500	0,00	Protein-based	Physical air-entraining	Rapid-K Thermal Conductivity test	0,500
				1700	1636	0,500	0,13				0,423
				1500	1461	0,500	0,22				0,363
				1300	1201	0,500	0,36				0,282
				1000	948	0,500	0,49				0,217
				800	757	0,500	0,60				0,165
				600	570	0,500	0,70				0,124
				500	453	0,500	0,76				0,091
				400	374	0,500	0,80				0,080
				300	252	0,500	0,87				0,065
Mydin, M. (2011). [4]	OPC cement/sand (2:1)	Ref	0,50	650	n.a.	n.a.	0,74	Protein-based	Physical air-entraining	Hot guarded plate test (HGP)	0,230
				700	n.a.	n.a.	0,71				0,240
				800	n.a.	n.a.	0,64				0,260
				900	n.a.	n.a.	0,57				0,280
				1000	n.a.	n.a.	0,51				0,310
				1100	n.a.	n.a.	0,47				0,340
				1200	n.a.	n.a.	0,44				0,390
Davraz, M. et al. (2016). [5]	CEM I 42.5 R Portland cement	PF/L	0,30	300	364	n.a.	0,77	Protein-based	Physical air-entraining	GHP/HFM-TS EN 12667	0,090
				400	510	n.a.	0,70				0,140
				500	563	n.a.	0,64				0,140
				600	715	n.a.	0,58				0,160
				700	837	n.a.	0,51				0,220
				800	851	n.a.	0,45				0,240
				900	965	n.a.	0,38				0,270
				1000	1100	n.a.	0,32				0,300
				1100	1272	n.a.	0,26				0,320
				1200	1321	n.a.	0,19				0,360
				1300	1429	n.a.	0,13				0,430
				1400	1531	n.a.	0,07				0,500
Oren, O. H. et al. (2020)	CEM II 42.5R/sand	FA40/Sa	0,91	1000	975	n.a.	0,53	Protein-based	Physical air-entraining	Transient plane source (TPS)	0,225
			0,68	1000	1029	n.a.	0,51				0,235
			0,55	1000	1033	n.a.	0,50				0,256
		FA40/Sa/GBS	0,91	1000	949	n.a.	0,53				0,220
			0,68	1000	1004	n.a.	0,52				0,226
			0,55	1000	1030	n.a.	0,51				0,230
		FA40/GBS	0,91	1000	926	n.a.	0,53				0,208
			0,68	1000	996	n.a.	0,50				0,226
			0,55	1000	1132	n.a.	0,49				0,264
Jiang, J. et al. (2017). [7] (2016). [8]	CEM I 42..5 R Portland cement	ER0%	0,60	n.a.	n.a.	n.a.	n.a.	Protein-based	Physical air-entraining	Heat Flow Meter (HFM)	0,059
		ER3%	0,60	n.a.	n.a.	n.a.	n.a.				0,064
		ER6%	0,60	n.a.	n.a.	n.a.	n.a.				0,063
		ER0%	0,80	n.a.	n.a.	n.a.	n.a.				0,060
		ER3%	0,80	n.a.	n.a.	n.a.	n.a.				0,063
		ER6%	0,80	n.a.	n.a.	n.a.	n.a.				0,064
		ER9%	0,80	n.a.	n.a.	n.a.	n.a.				0,065
		ER9%	0,60	n.a.	n.a.	n.a.	0,89				0,069
		Ref	0,80	n.a.	n.a.	n.a.	0,92				0,052
		C/SF6	0,80	n.a.	n.a.	n.a.	0,91				0,050
		C/MK20	0,80	n.a.	n.a.	n.a.	0,92				0,054
		C/MK20/SF6	0,80	n.a.	n.a.	n.a.	0,92				0,054
		Ref	1,00	n.a.	n.a.	n.a.	0,91				0,053
		C/SF6	1,00	n.a.	n.a.	n.a.	0,91				0,051
		C/MK20	1,00	n.a.	n.a.	n.a.	0,91				0,053
		C/MK20/SF6	1,00	n.a.	n.a.	n.a.	0,91				0,055

2.3.3 Heat Conduction in Two-Phase Porous System

This section presents a simplified approach for the determination of the homogenized thermal conductivity, k_{eff} (W/m/K) of cementitious foam composites. The model is based on stacked porous amounts (porosity), continuous- and dispersed-phase conductivities, and geometrical classification of pores according to the comprehensive study of the aqueous foam structures presented in [77–79]. The main objective is to propose pore geometrical-fitting parameters that can be employed in designing LHTES/TES-enhanced (two phases) cementitious foams with general low-to-high porosity.

2.3.3.1 Modified Lewis–Nielsen Model for Conductivity of Porous Cementitious Composites

Cementitious foam's microstructure, considered as a two-phase system, can be modelled as a continuous phase made of cement paste (skeleton) and a dispersed phase made of air-voids (Figure 49). The main thermophysical parameters of the two-phase system which govern the homogenized heat transport phenomena include: (i) the specific heat, (ii) the density, (iii) the thermal conductivity (being i., ii., and iii. of the single phases), and (iv) possible thermal lag, i.e., interfaces between these phases. Knowing these parameters, one can describe the thermal behavior of the two-phase porous media.

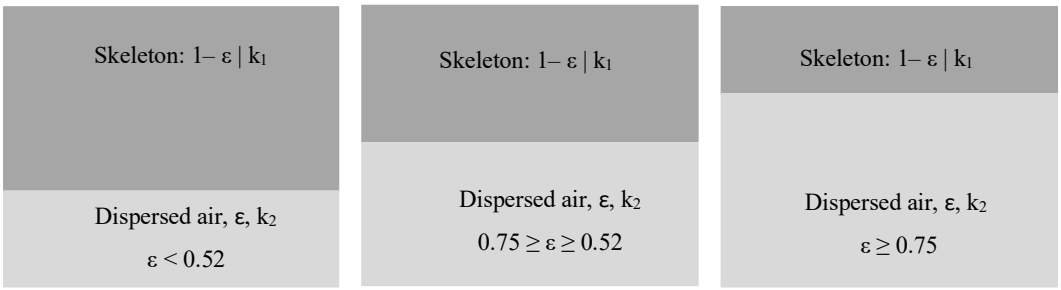

Figure 49. Schematic illustration of a two-phase cementitious foam without considering the meso-scale air-void distribution: (a) low- ($\varepsilon < 0.52$), (b) medium- ($0.75 \geq \varepsilon \geq 0.52$), and (c) high-porosity ($\varepsilon \geq 0.75$).

The thermal conductivity (k) in a two-phase porous system is significantly influenced by the conductivities of the continuous phase (k_1) and the dispersed phase (k_2), and by their concentrations (i.e., $1- \varepsilon$ for the skeleton and ε for the dispersed air, as in Figure 49). In this regard, numerous analytical equations have been proposed to solve the effective (i.e., homogenized) thermal conductivity of these two-phase systems. These models are capable of accurately predicting the effective heat transfer by considering and weighting the porosity and conductivity of each single component. However, these approaches become limited when the pore volume fraction increases and, at the same time, the isolated pores become connected [69]. Nevertheless, the study conducted by Lewis and Nielsen [50,51], while originally based on the theory of the elastic moduli of composite materials, has been found to be a very good approximation for thermal conduction**,** if enough information about the air content and the pore structure is available.

2.3.3.2 Fitting Parameters, A and ψ for Porous Cementitious Composites

In this work, the following expression by Lewis and Nielsen [50] has been used as homogenization rule for predicting the conductivity of cementitious foams:

$$\frac{K}{K_1} = \frac{1 + A\frac{K_2/K_1 - 1}{K_2/K_1 + A}\varepsilon}{1 - \frac{K_2/K_1 - 1}{K_2/K_1 + A}\psi\varepsilon} \quad (1)$$

where ε is the fraction of air inclusion, *A* the shape factor for the dispersed air-voids, and ψ considers the type of packing of the pores, as well as the presence of either predominantly closed or interconnected pores. In Equation (1), the accurate definition (and calibration) of A and ψ represents the key task, one which requires a fundamental knowledge and study of the pore structure of the cementitious foams. For the evolution of A and ψ, it is also important to consider the hydration process and aging time of the foam. Foam pore structures can change during the hardening process due to rheological changes of the cement matrix, with consequent volumetric reduction (shrinkage) of the paste due to drying processes. Also, local failure of individual lamellae at advanced stiffening/solidification time steps can lead to pore systems consisting of intersecting (coalescing) spherical pores. In addition to volume changes, additives with different surface characteristics (polarity) can also influence pore structure developments, leading to uncertainties in pore structure and deviation between the real (measured) and the theoretical (calculated) porosity of the composite.

In the fresh state of the foam, bubble coalescences and/or bubble coarsening are directly related to an increasing of the air inclusion amount, which leads to an increase in the mean pore diameter and a shift of the pore-size distribution towards larger pores. In this regard, pore systems with a predominance of connected pores are formed from polyhedral-shaped foams which have very high air contents ($\varepsilon \geq 0.75$) and exhibit extremely thin lamellae (ca. 20–30 µm). Due to this, highly irregular structures are associated with high-porosity foams with a dwindled cement matrix. In foams with a predominance of spherical bubbles, the minimum and maximum pore sizes, together with their distribution, can influence the maximum achievable porosity. Thus, assuming an ideal distribution of the pore sizes, a geometric maximum-possible porosity of 0.75 can be achieved for foams with spherical bubbles. A classification into polyhedral foams, spherical foams, and bubble systems can be adopted for the characterization of foamed cement pastes. This classification represents a correlation between geometry, fraction of air inclusion (porosity) and bulk density of a fictitious aqueous phase with a bulk density of 2.0 kg/dm^3 [78].

It follows that, by considering the correlation between fraction of air inclusion and void geometry, as sketched in Figure 50, the calibration factors A and ψ can be defined according to the literature. Particularly, the constant A, related to the generalized Einstein coefficient (Einstein, 1905, 1906), which represents primarily the shape of the air inclusions, for any direction of heat flow, can be calculated for aggregates of spheres as [51]:

$$A = \frac{2.5}{\Phi_m} - 1 \quad (2)$$

where Φ_m represents the maximum packing fraction of the randomly dispersed air voids, defined as the true volume of the air voids in cementitious foam divided by the volume they appear to occupy when packed to their maximum extent. In this sense, the three types of foam classes can be taken from Table 13.

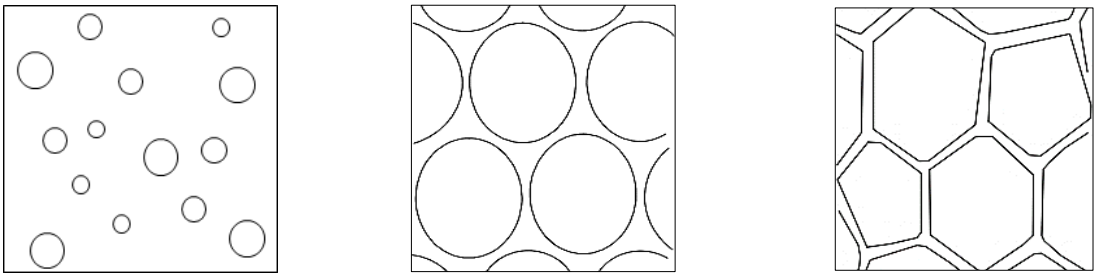

(a) Random closed-cell bubbles $\varepsilon < 0.52$ (b) Spherical bubbles $0.75 \geq \varepsilon \geq 0.52$ (c) Polyhedral bubbles $\varepsilon \geq 0.75$

Figure 50. Correlation between the fraction of air inclusion (ε) and air void geometry in cementitious foams of (a) low porosity, (b) medium porosity, and (**c**) high porosity, based on the findings of [77,79].

Table 13. Air-void shape/packing classifications of low-, medium-, and high-porosity cementitious foam; see Supplementary Material S2 for more details.

Air Fraction	Foam Class	Shape of Air Voids	Type of Packing	Maximum Packing Fraction (Φ_m)
$\varepsilon \geq 0.75$	I	Polyhedral	Hexagonal close	0.74
$0.75 \geq \varepsilon \geq 0.52$	II	Spherical	Random close	0.64
$\varepsilon < 0.52$	III	Bubbles	Random loose	0.60

In this study, Equations (1–3) are employed for predicting the homogenized (effective) conductivity of the analyzed low-to-high porous cementitious foams. The proposed methodological approach enables precise determination of Φ_m (refer to Table 13) for solving Equations (2) and (3) within each foam class, simplifying Equation (1) for enhanced practicality in engineering applications. Consequently, the only remaining unknown parameters are porosity and matrix conductivity. This represents a significant advancement in thermal conductivity assessment, particularly addressing the impact of pore geometry within the mid-to-high-porosity range of mineral foams.

The structural parameter ψ, needed for evaluating the conductivity of cementitious foam, can be estimated as [51]:

$$\psi = 1 + \left(\frac{1 - \Phi_m}{{\Phi_m}^2}\right)\varepsilon \quad (3)$$

This advancement greatly contributes to standardizing the thermal conductivity of mineral foams, enhancing their utility and efficiency in engineering design and applications.

It is important to emphasize that the proposed fitting parameters for mineral foams in this study are based on well-established mathematical principles and exclusively tied to the system's geometry; see Supplementary Material S2 for more details. Determining the correct parameters would be arbitrary and impractical without a comprehensive understanding of the factors influencing thermal conductivity and knowledge of mineral foam pore structures.

2.3.4 Analytical Predictions vs. Experimental Data

2.3.4.1 Classification of Test Data

In this section, the experimental data presented in Section 2 are analyzed to explore potential correlations between the fraction of air inclusion (ε), target density, and effective foam conductivity. The primary aim of this analysis is to classify the data into specific categories, such as low-, medium-, and high-porosity cementitious foams. Additionally, a categorization of the data based on air-void structure/geometry, such as random closed-cell bubbles, spherical bubbles, or polyhedral ones, is considered, as presented in Section 3.2. This information is crucial for the accurate determination of calibration parameters "A" and "f" in Equation (1).

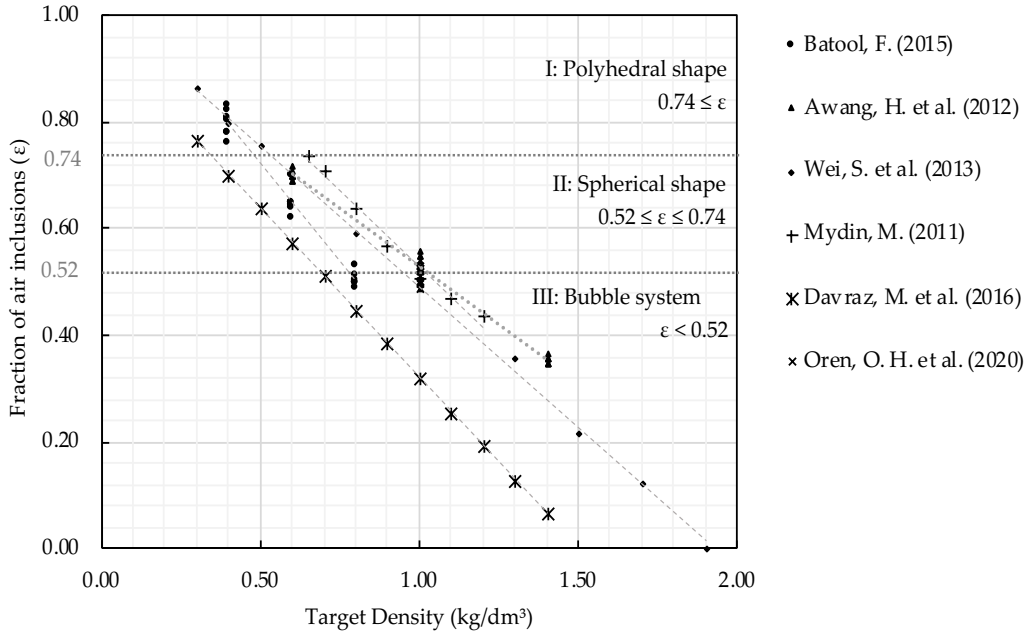

Figure 51. Fraction of air inclusion (ε) vs. target density (kg/dm^3); data by [67–74].

Figure 51 illustrates the relationship between the fraction of air inclusion (ε) and the target density for all datasets [67–74] considered in this study. It demonstrates a consistent linear decrease of porosity with increased density across all the data points. Furthermore, by employing the classification outlined in Section 3.2, the data can be categorized into three distinct foam classes: "Class I" for foams with polyhedral-shaped air voids (exhibiting hexagonal close packing) and a fraction of air inclusion (ε) greater than or equal to 0.75;

"Class II", consisting of foams with spherical-shaped bubbles, with random close packing and a fraction of air inclusion ranging from 0.75 to 0.52; lastly, "Class III" are foams with low porosity, with random loose packing and a fraction of air inclusion (ε) below 0.52.

Figure 52 displays the correlation between the foams' homogenized conductivity (k_{eff}) and target density for collected datasets [67–74]. It exhibits a clear linear increase of conductivity against increased density across all the data points. In this case, regarding the presented classification described in Section 2, the data can be categorized into four distinct subtypes: "ultra-light insulating foams", which possess a target density that is equal to or lower than 0.30 kg/dm^3; "low-density insulating foams", which includes foams with target densities ranging from 0.30 kg/dm^3 to 0.80 kg/dm^3; "moderate-strength foams", classifying foams having a target density ranging from 0.80 kg/dm^3 to 1.35 kg/dm^3; and finally, "structural foams", comprising foams with a target density higher than 1.35 kg/dm^3. It is worth noting that as the density increases, the insulation performance of the material decreases, as indicated by a higher level of foam conductivity.

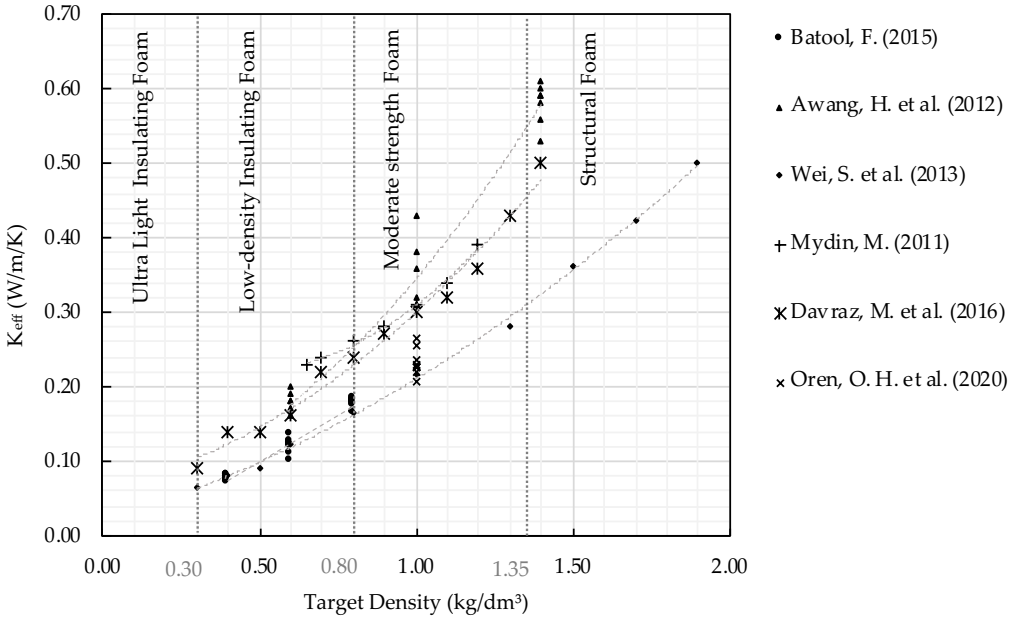

Figure 52. K_{eff} (W/m/K) vs. target density (kg/dm^3); data from [67–74].

Figure 53 combines the information from Figures 50 and 51, establishing a correlation between foam effective/homogenized conductivity (k_{eff}) and the fraction of air inclusion (ε) for the presented datasets. This graph clarifies the classification of the considered foams, based on air-void structure/geometry and packing characteristics, presenting the related conductivity range (upper and lower values) expected for each foam system class. The classification in Figure 53identifies three foam classes: the first one consists of foams with bubble types characterized by low porosity and random loose packing (ε < 0.52), with expected keff higher than 0.2 W/m/K; the second one comprises foams with predominantly non-connected spherical-shape voids, exhibiting random close packing, and having a fraction of air inclusion ranging from 0.52 to 0.75, with expected keff between 0.2 W/m/K and 0.1 W/m/K; lastly, the third class includes polyhedral-shaped foams, with hexagonal close packing and ε greater than or equal to 0.75 with expected keff less than 0.1 W/m/K.

An interesting observation arising from Figure 6 is that the type of internal structure in the foam is directly linked to the total air fraction and the target density of the system.

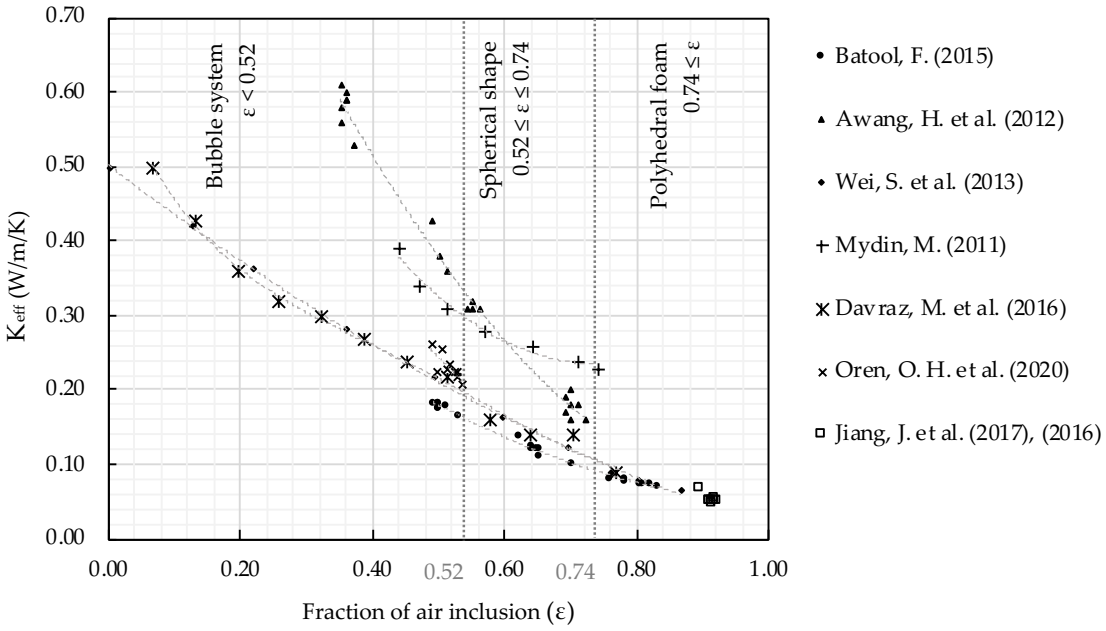

Figure 53. Keff (W/m/K) vs. fraction of air inclusion (ε): data by [67–74].

The classifications, as shown between Figures 50–52, are crucial for guiding the subsequent section, which presents a unified approach for modeling heat transfer conductivity in various types of foams. The approach considers a wide range of porosity levels, extending from low to high porosity cementitious foams, and points out the effects of the different types of air-void geometry and meso-structural types. Thus, by understanding the influence of these factors, this section provides valuable insights into the heat-transfer characteristics of mineral foams, enabling a comprehensive understanding of their homogenized thermal conductivity.

Analytical Description vs. Experimental Measurements of Thermal Conductivity Keff

In this section, the homogenized thermal conductivity of each foam is predicted and compared to the corresponding experimental data from Section 2, as also categorized in Section 4.1. A total of one hundred foam cases were analyzed, and all the data were unified and calibrated by fitting the parameters "A", "Φm", and "ψ", as listed in Table 14.

Table 14. Calibrated "A", "Φm", and "ψ" parameters for the foam concretes determined by [67–74].

Air Fraction	Foam Class	A	Φm	ψ
$\varepsilon \geq 0.75$	I	2.37	0.74	1.370
$0.75 \geq \varepsilon \geq 0.52$	II	2.90	0.64	1.563
$\varepsilon < 0.52$	III	3.10	0.60	1.546

The equation (Equation (1)) used for the analysis is modified, as:

$$\frac{K}{K_1} = \frac{1 + A\frac{K_2/K_1 - 1}{K_2/K_1 + A}\varepsilon}{1 - \frac{K_2/K_1 - 1}{K_2/K_1 + A}\left(1 + \left(\frac{1 - \Phi_m}{\Phi_m{}^2}\right)\varepsilon\right)\varepsilon} \quad (4)$$

Figure 54 illustrates all the data in terms of effective thermal conductivity (k_{eff}), based on the data from [67–74], and the predicted values obtained using the modified Lewis–Nielsen expression proposed in Equation (4).

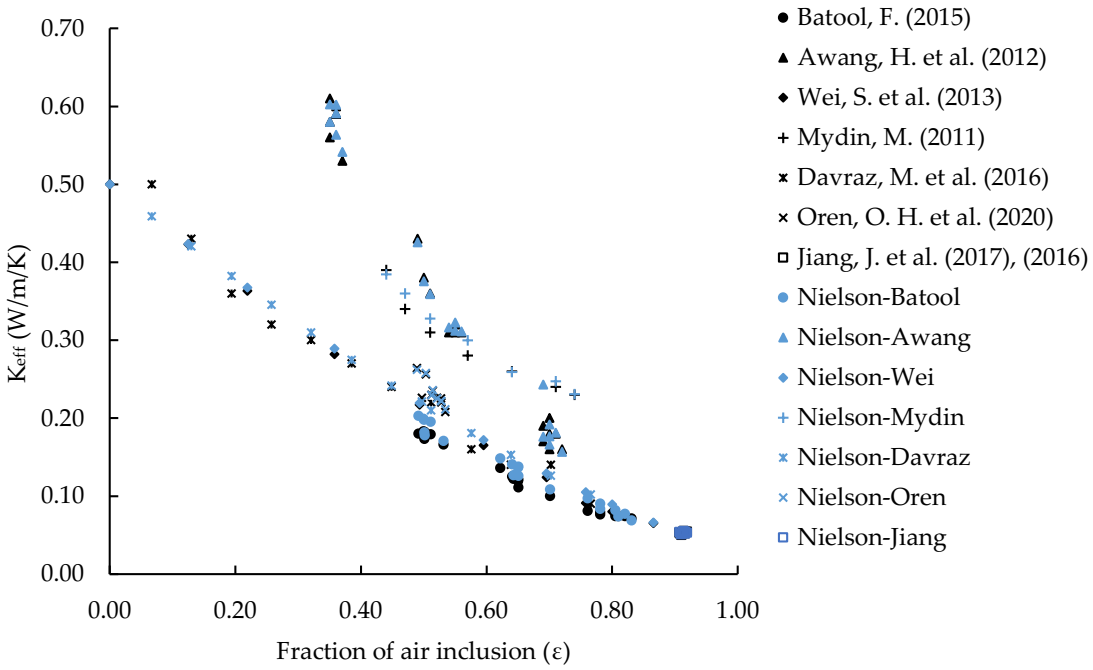

Figure 54. K_{eff} (W/m/K) [67–74] vs. fraction of air inclusion (ε); blue points indicate the predicted values and black points indicate the experimental findings.

Notably, the homogenized conductivity predictions can be achieved by solely calibrating "A" and "Φ_m" parameters, which are mainly influenced within the three distinct foam classes mentioned in Section 3.2. Specifically, the fundamental factors are the foam air-volume fraction and the dispersed air-geometry characteristics, while one can disregard other factors, such as binder variations, casting types, foaming agents, and other components/amounts. This aspect represents the significant contribution of this study, as the application of the modified Lewis–Nielsen expression to an extensive dataset of mineral foams with widely scattered formulations and thermal responses has not been attempted previously. This limitation arises from the lack of sufficient experimental data regarding the classification of pore geometry in mineral foams, a crucial factor for determining the appropriate values of parameters A and Φ_m in model implementation.

The presented results show that, by considering the shape of the dispersed air and their packing characteristics, a consistent stable response for each foam type can be achieved, i.e., class I (polyhedral-shaped air voids), class II (spherical-shaped), and class III foams (loosely packed bubble inclusion). There is substantial good agreement between the theory and the experimental data.

To demonstrate the effectiveness of this approach, Figure 55 shows the homogenized predicted conductivity values plotted against the employed data. The figure displays both the linear-regression curve and the square-root error, both of which help to identify the best-fit line that presents the relationship between the measured variables and the predicted ones.

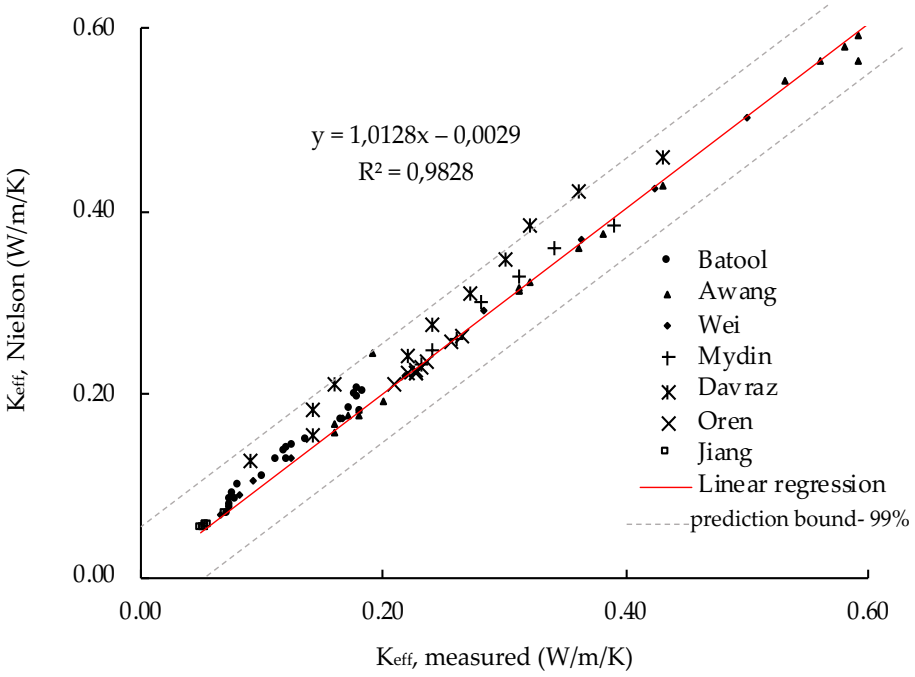

Figure 55. Lewis–Nielsen predictions: k_{eff}, Nielson (W/m/K) vs. measured conductivity k_{eff}, measured (W/m/K), for all collected data; comparison and linear regression + R^2, slope >1 model overestimates the conductivity data.

The prediction results reveal promising outcomes, with a high R^2 value of 0.9828 and a regression line slope of 1.0128. In Supplementary Material S3, Figures S2–S8 show the homogenized predicted conductivity values plotted against the employed data, analyzed author by author. The agreement between experimental values and predicted ones is remarkable; see Figure 55. A prediction interval, within which, with a probability of 99%, future observations are expected to fall, is presented in Figure 55. It provides an uncertainty of 0.02 W/m/K surrounding the predicted foam homogenized conductivity value by applying the proposed approach. The scatter in the data can potentially be attributed to the experimental errors due to sampling, measurement techniques, and measurement accuracy.

It is possible to further simplify and extend Equation (4) by incorporating the parameters from Table 14. However, the predictive results obtained demonstrated remarkable accuracy, closely matching the experimental data. At this point, there is no compelling reason to extend the equation further.

2.3.4.2 Extension of the Analytical Model for Porous LHTES-Systems (Mineral Foams)

The main objective of the analytical model proposed in Sections 4.1 and 4.2 was to predict the conductivity, or the homogenized one, of cementitious foams made of various types and amounts of components and

having variable properties. By knowing the conductivity of the matrix (or skeleton) and considering the amount of air inclusion (porosity), and by using the analytical formula based on air dispersion shape and packing, the conductivity of the homogenized porous system was well predicted.

Table 15. Data used in the proposed model to predict homogenized conductivity of thermal-energy-storage mineral foam composites; see Sam et al. [80].

	Vol.- %MPCM in Paste	K_{eff} Paste (w/b = 0.4) Solid Phase MPCM (W/m/K)	K_{eff} Paste (w/b = 0.4) Liquid Phase MPCM (W/m/K)
LHTES Paste	40	0.600	0.464
	20	0.754	0.759
K_{eff} Ref Paste (W/m/K)	0.89–0.93		
K Air (W/m/K)	0.025		

Based on this, now the model can be extended to predict the conductivity of latent-heat-storage-enhanced porous systems. The goal is to facilitate simulations through simple engineering calculations, without the need to perform expensive experimental tests. The estimation of the homogenized conductivity of LHTES-enhanced foams is thus considered by employing different optimization methods, such as embedding microencapsulated phase change material (MPCM) within the skeleton at various percentages (i.e., 10%, 20%, 30%, and 40%).

The investigation is limited to 40%, since higher percentages have been found to compromise foam stability. The proposed analytical formula (Equation (4)) has been employed by adopting the parameters of the LHTES-enhanced skeleton (MPCM pastes) by Sam et al. [80], including the thermal conductivity data for the MPCM paste, in both liquid and solid phases. The conductivity of the air is sourced from the literature. All these data are summarized in Table 15.

The graphs of Figures 56 and 57 illustrate the predicted homogenized conductivities of the LHTES/TES-enhanced foams, with and without considering 20% and 40% of MPCM pastes in comparison. More specifically, the skeleton of the foams consists of cement paste with a water-to-binder ratio of 0.40, which was mixed with a commercial MPCM having a melting/solidification temperature of 24 °C, with volume percentage substitutions of 0%, 20% and 40%, respectively. The experimental data were tested by the author in the previous work; see Sam et al. [80]. By analyzing the graphs, the conductivity range within each foam class and porosity level can be determined at any desired porosity. The effective homogenized values for 10% and 30% of MPCM substitutions in the paste can be smoothly interpolated from the data available in this section.

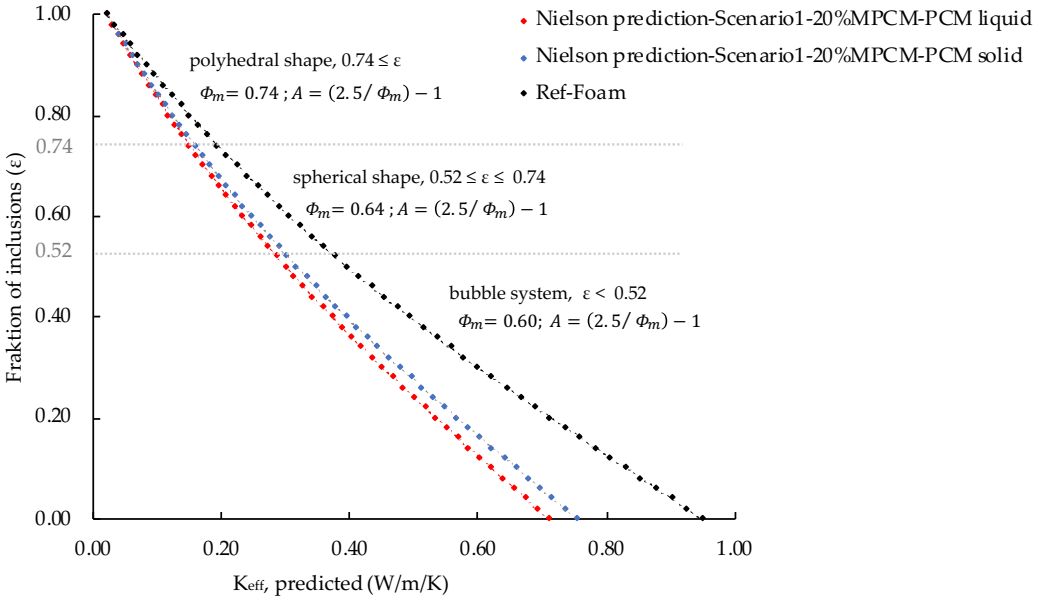

Figure 56. Foam with skeleton having 0% (Ref) and 20% MPCM: fraction of air inclusion (ε) vs. $k_{eff,}$ predicted (W/m/K).

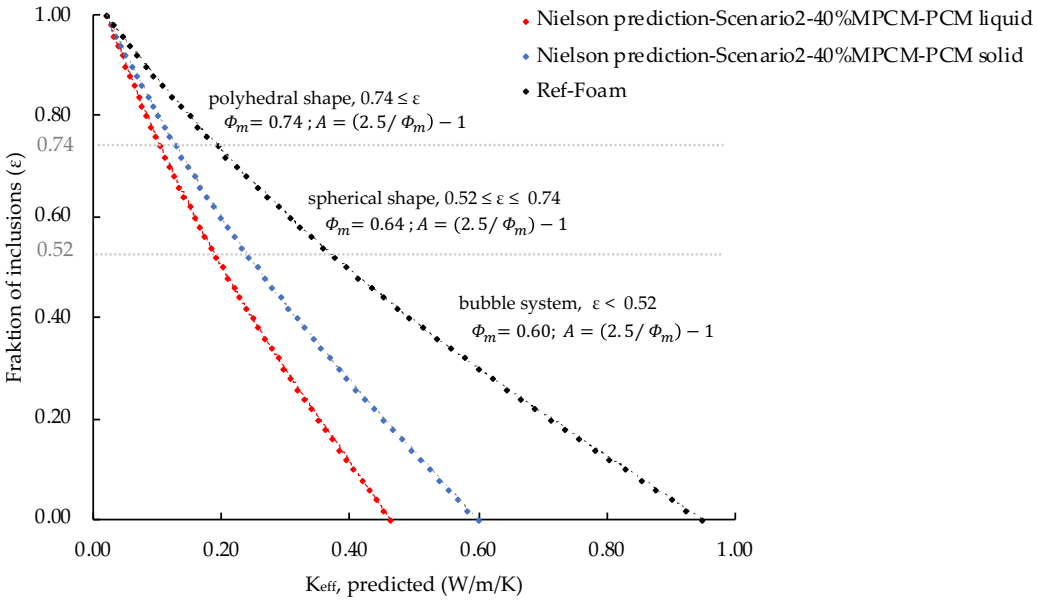

Figure 57. Foam with skeleton having 0% (Ref) and 40% MPCM: fraction of air inclusion (ε) vs. $k_{eff,}$ predicted (W/m/K).

In conclusion, Table 16 presents the predicted homogenized conductivity ranges for different foam classes and volumetric amounts of MPCM, offering insights into the conductivity of polyhedral and spherical foam systems (of both Class I and II) with porosities higher than 52%, which can be used for energy storage purposes.

Table 16. Proposed predicted conductivity range for further thermal analysis and numerical simulations. Values for specific porosity can be taken from Figures 55 and 56.

	Foam Class	Vol-. %MPCM in paste	k_{eff} foam solid phase PCM (W/m/K)	k_{eff} foam liquid phase PCM (W/m/K)
TES Polyhedral Foam	I	40	≤0.14	≤0.10
		20	≤0.17	≤0.15
TES Spherical Foam	II	40	≤0.24	≤0.20
		20	≤0.30	≤0.28
TES Polyhedral Foam	I	0	≤0.2	
TES Spherical Foam	II	0	≤0.39	

This information is utilized for a 1D-wall simulation presented next, in Section 5, by incorporating porosity and effective thermal conductivity of TES-Foam with and without MPCM.

2.3.5 Integration of LHTES and Dynamic Envelopes: Application Scenario-1D Model based on the First Law of Thermodynamics

In this section, the thermal performance of multi-layer enclosing structures consisting of expanded polystyrene (EPS) and TES-foam (foam having porosity higher than 52%) as external layers and reinforced concrete as main structural layer is assessed by using standard one-dimensional (1D) FEM simulation. More details about the applied theoretical background are presented in Supplementary Materials S4.

This chapter underscores the model's physical significance for a building envelope and illustrates how the model simplifies the intricate numerical calculations that were previously required to determine the thermal conductivity of mineral foams. These calculations include scenarios involving 20% MPCM in the skeleton and 90% porosity.

The analytical model implemented enables the straightforward representation of thermal behavior within building envelopes by the modification of input parameters such as matrix conductivity and/or porosity. This analytical capability extends to the calculation and implementation of conductivity while addressing concerns related to volumetric heat capacity through a simple one-dimensional FEM simulation.

Parametric Studies for Thermal Performance in Multi-Layer Structures (EPS vs. TES Foam Composites)

The heat flow via conduction through a two-layer enclosing structure is schematized in Figure 58: the x-axis denotes the direction of the one-dimensional heat flux, and considers a heat flow between the exterior layer, L1 (0.1 m thickness), and the interior one, L2 (0.2 m thickness), with total thickness of $\Delta x = 0.3$ m.

For one-dimensional heat flow, the temperature gradient through the structure is simulated. To solve the heat transfer problem (as shown in the Supplementary Materials), two nodes' truss finite elements (FEs) were adopted and the non-linear FEM problem was solved in MATLAB; the space discretization of the wallboard uses 100 FEs, while for the temporal one, an implicit backward Euler method with a time stepping of 5 min within 24 h was chosen.

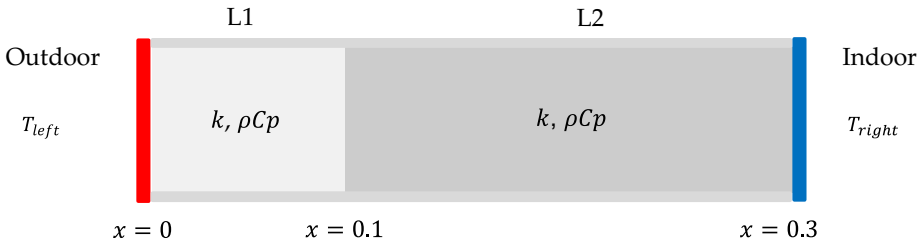

Figure 58. Schematized one-dimensional (1D) conduction model for a two-layer wall.

Initial boundary conditions considered an initial temperature $T_0 = 20$ °C (i.e., at t = 0), while essential (Dirichlet types) boundary conditions were fixed according to two case studies:

- "Summer" $T(x = 0, t) = T_{left} = 40\,°C \quad T(x = 0.3, t) = T_{right} = 20\,°C$;
- "Winter" $T(x = 0, t) = T_{left} = -5\,°C \quad T(x = 0.3, t) = T_{right} = 20\,°C$;

Two scenarios are simulated: wall section with TES-foam as insulating layer L1 containing 2% MPCM (T_m: 24); and wall section with EPS as insulating layer L1. Tables 17 and 18 provide the key thermophysical parameters of the considered EPS and TES foam with and without MPCM for the analysis of the thermal behavior of the two-layer wall sections.

Table 17. Thermophysical properties of single components relevant for calculating the volumetric heat capacity of TES foam, both with and without MPCM, using mixture theory.

	Paste [80]	Air	MPCM [80]
Density, ρ (kg/m^3)	1708	1.2	760
(Sensible) specific heat capacity, c_p (J/kg/K)	1300	1000	2100
Latent heat storage, h (kJ/kg)	0	0	195

Using the measured thermophysical properties of single components shown in Table 17, the volumetric heat capacity of TES-foam with and without MPCM can be simply ascertained by applying the mixture law [83]; see Table 18. Density and effective conductivity of TES-foams with 90% porosity are two parameters derived from the presented model in Sections 2.3.3 and 2.3.4.

Table 18. Thermophysical properties of composites: model input for simulating one-dimensional (1D) temperature profiles. 'TES-Foam' denotes foam with porosity higher than 52% and without integrated MPCM. * Foam with ε=0.90, MPCM in solid phase.

	TES-Foam 0% MPCM	TES-Foam 2% MPCM	RC-Wall	EPS [81,82]
Density, ρ (kg/m^3)	200	90	2000	30
Predicted effective conductivity, k_{eff} (W/m/K)	0.07 *	0.05 *	2.1	0.04
Volumetric heat capacity, ρ C_p, sensible (kJ/m^3/K)	223.120	210.632	1760	45
Latent heat storage, h (kJ)	0	2964	0	0

Figures 59 and 60 present the transient temperature distribution along the x direction across the two-layer structure, showing the differing responses of EPS and TES-Foam with 2% volumetric amount of MPCM to the heat and cold wave. The initial scenario involves both outside and inside temperatures equal to 20 °C at t_0. Subsequently, a sudden increase/decrease in the outside temperature to 40 °C/−5 °C occurs. The graphs depict the temperature distribution inside the wall at 5 min intervals. In both Figures 58 and 59, T_1 represents the temperature at location ×1, recorded 5 min after the initiation of a temperature increase or decrease, demonstrating a noticeably slower rate of temperature change in response to both heat (Figure 59) and cold (Figure 60) wave stimuli for TES-Foam. The simulation results shown in Figures 58 and 59 indicate that the volumetric heat capacities of the materials have a decisive impact on the capacity of heat storage and prolonging the heat/cold penetration, providing a balanced and energy-efficient means of maintaining indoor comfort.

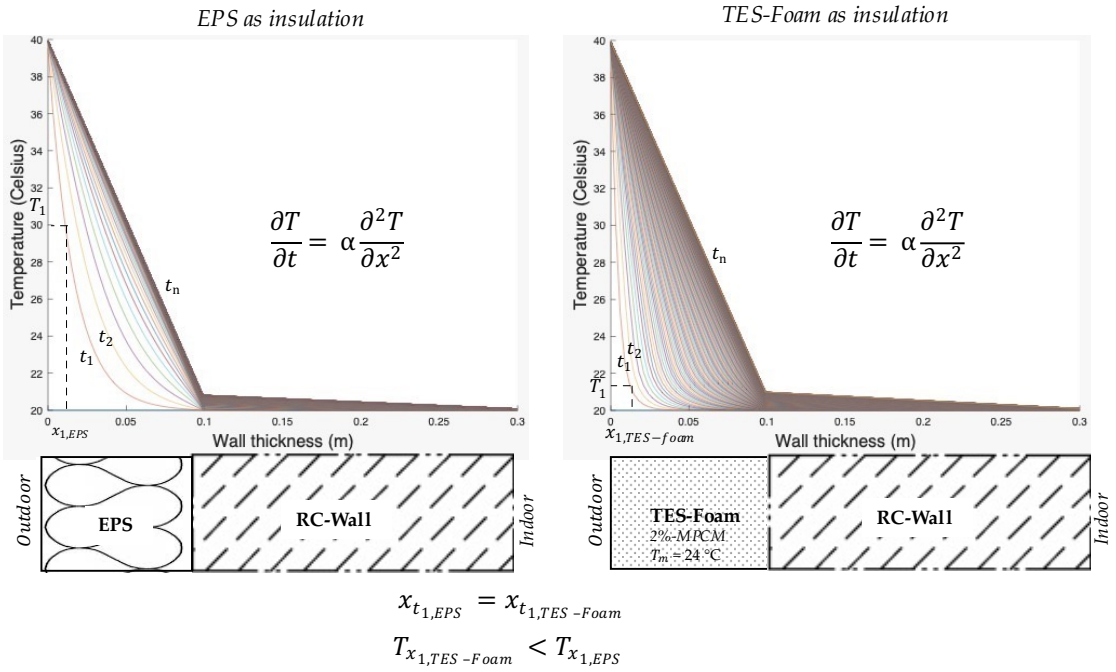

Figure 59. One-dimensional (1D) transient temperature field across the wall with thickness (Δx = 30 cm), at t0, the temperature difference ΔT = 0 (Tinside = Toutside =20); sudden outside temperature increases to Toutside = 40 to evaluate the wall response to heat wave at any fixed position along the x axis. The temperature profile for the wall section is depicted using lines of different colors at various time intervals: t1 = 5 min, t2 = 10 min, up to tn = 24 h.

A significantly higher volumetric heat capacity of TES/LHTES-Foam (223.120 kJ/m^3/K/210.632 kJ/m^3/K) in comparison to EPS (45 kJ/m^3/K) reduces the required storage volume and, at the same time, the structure thickness. TES-Foam functions as thermal mass or thermal battery, effectively moderating internal temperatures by mitigating day–night temperature fluctuations. When integrated as LHTES-Foam, TES-Foam significantly enhances its thermal capacity through the efficient latent heat storage and controlled

release of heat energy. During warmer periods, it adeptly absorbs and stores excess heat, while during cooler periods, it steadily releases the stored heat, contributing to the stabilization and regulation of indoor temperatures. This dual functionality of TES Foam as both a thermal mass and an advanced LHTES material provides a robust and energy-efficient solution for maintaining a consistently comfortable indoor environment, regardless of external weather variations.

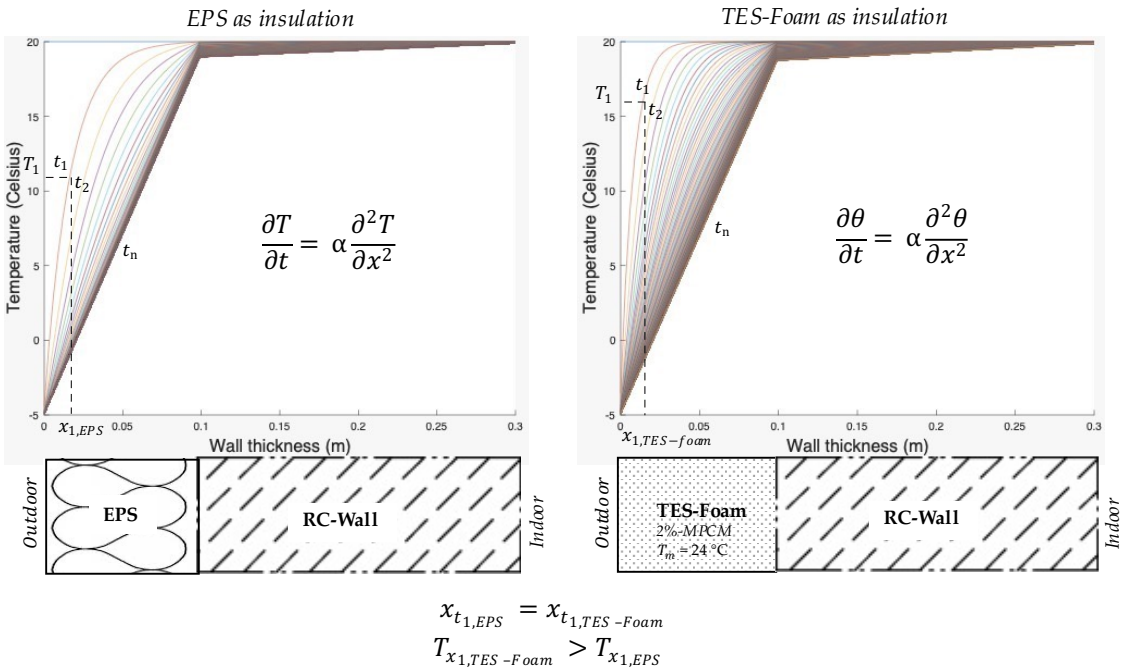

Figure 60. One-dimensional (1D) transient temperature field across the wall with thickness (Δx = 30 cm*)*, at t_0, the temperature difference ΔT = 0 ($T_{inside} = T_{outside} = 20$); sudden outside temperature decreases to $T_{outside} = -5$ to evaluate the wall's response to a cold wave at any fixed position along the x axis. The temperature profile in the wall section is depicted using lines of different colors at various time intervals: $t_1 = 5$ min, $t_2 = 10$ min, up to $t_n = 24$ h.

Table 19 summarizes the calculated thermal diffusivity (α) and thermal effusivity (b) variables of proposed structures to assess the thermal performance under transient boundary conditions and conducts an evaluation of the energy-saving capacities of both structures. Lower thermal diffusivity of LHTES/TES-Foam (0.0237 10^{-5} m^2/s/0.0314 m^2/s), compared to EPS (0.08 10^{-5} m^2/s), provides a much slower response to temperature differences, and decreases the transient heat transfer, or the progression of a temperature wave in the system, extending the time for charging and discharging of heat/cold load and turns, all in a more thermally inert system; also see Figures 58 and 59. This is especially beneficial for reducing over-temperature degree hours in indoor spaces. A much higher thermal effusivity value for LHTES/TES-Foam (102.6 $m^2/k/S^{0.5}$/124.9 $m^2/k/S^{0.5}$ vs. 42.5 $m^2/k/S^{0.5}$ for EPS) leads to a larger amount of heat being stored, which is significant for the effectiveness of internal storage masses.

Table 19. Calculated thermophysical properties relevant for dynamic envelope evaluation; thermal diffusivity α = k/ρcp and heat penetration coefficient b = $\sqrt{k\rho c_p}$.

	TES-Foam 0% MPCM	TES-Foam 2% MPCM	RC-Wall	EPS
Thermal diffusivity, α 10^{-5} (m^2/S)	0.0314	0.0237	0.15	0.08
Heat penetration coefficient, b (J/(m^2/k/$S^{0.5}$)	124.9	102.6	1922.5	42.5

2.3.6 Conclusions

This paper presents an analytically based approach which combines the effective thermal conductivity of the foam skeleton with dispersed air bubbles, creating a porous media system. The objective is to provide a comprehensive description and precise prediction of the thermal behavior of TES-mineral foams with/without LHTES (incorporation of MPCM), with varying porosity levels, ranging from low to high, with the final goal of facilitating simulations through simple engineering calculations, and without the need to perform expensive experimental tests.

Considering the correlation between porosity and geometry of the dispersed air, through the porous mineral systems, six fitting values of parameters "A" and "Φ_m" were proposed for use in the modified analytical expression proposed by Lewis and Nielsen (1940), based on three distinct foam classes: Class I foams, having polyhedral-shaped air voids and a fraction of air inclusion (ε) greater than or equal to 0.75; Class II foams, having spherical-shaped bubbles and a fraction of air inclusion ranging from 0.75 to 0.52; and lastly, Class III foams, with low porosity and a fraction of air inclusion (ε) below 0.52. The calculated homogenized conductivities were validated by using the proposed fitting parameters and upon the collected experimental data, resulting in a consistently stable response for all foam classes and datasets.

By determining the effective conductivity of TES-mineral foams, with and without latent heat integration, at high porosity of 90%, and by calculating the volumetric heat capacity of the composite using the mixture theory, the potential of LHTES/TES-enhanced mineral foams to be used for thermal energy storage purposes was discussed. In this regard, thermal diffusivity and the heat penetration coefficient of the LHTES/TES-enhanced mineral foams was calculated and compared with conventional EPS. The results showed a 3.5 to 4 times higher value for thermal storage capacity and an almost 70%/60% lower thermal diffusivity for LHTES/TES-enhanced mineral foams, respectively, compared to EPS layers, without considering the latent heat storage amount (h).

Future research directions might aim at exploring new building envelopes that incorporate dynamic thermal performance. This approach differs from conventional solutions, which are based on obsolete concepts of insulation and thermal resistance (R-value) parameters. The main goal will be to synergistically integrate both insulation materials and latent heat thermal storage (LHTS), thus opening new perspectives for prospective novel envelope designs. Research studies regarding their long-term stability, durability, and performance under different environmental conditions would contribute to a comprehensive understanding of their applicability in real-world scenarios.

References

[1] Miller, S.A.; Habert, G.; Myers, R.J.; Harvey, J.T. Achieving net zero greenhouse gas emissions in the cement industry via value chain mitigation strategies. One Earth 2021, 4, 1398–1411.

[2] Chen, X.-S.; Li, Y.-P.; Jiang, Y.-L.; Liu, Y.-X.; Zhang, T. Theoretical research on gas seepage in the formations surrounding bedded gas storage salt cavern. Pet. Sci. 2022, 19, 1766–1778.

[3] Xue, W.; Wang, Y.; Chen, Z.; Liu, H. An integrated model with stable numerical methods for fractured underground gas storage. J. Clean. Prod. 2023, 393, 136268.

[4] Yang, T.; King, W.P.; Miljkovic, N. Phase change material-based thermal energy storage. Cell Rep. Phys. Sci. 2021, 2.

[5] Lu, S.; Lin, Q.; Liu, Y.; Yue, L.; Wang, R. Study on thermal performance improvement technology of latent heat thermal energy storage for building heating. Appl. Energy 2022, 323, 119594.

[6] Hassan, F.; Jamil, F.; Hussain, A.; Ali, H.M.; Janjua, M.M.; Khushnood, S.; Farhan, M.; Altaf, K.; Said, Z.; Li, C. Recent advancements in latent heat phase change materials and their applications for thermal energy storage and buildings: A state of the art review. Sustain. Energy Technol. Assess. 2021, 49, 101646.

[7] Heim, D.; Pawłowski, M. The methodology of thermal energy management for nearly zero energy buildings. Period. Polytech. Civ. Eng. 2019, 63, 499–517.

[8] Al-Yasiri, Q.; Szabó, M. Experimental study of PCM-enhanced building envelope towards energy-saving and decarbonisation in a severe hot climate. Energy Build. 2023, 279, 112680.

[9] Piselli, C.; Prabhakar, M.; de Gracia, A.; Saffari, M.; Pisello, A.L.; Cabeza, L.F. Optimal control of natural ventilation as passive cooling strategy for improving the energy performance of building envelope with PCM integration. Renew. Energy 2020, 162, 171–181.

[10] Saffari, M.; de Gracia, A.; Fernández, C.; Cabeza, L.F. Simulation-based optimization of PCM melting temperature to improve the energy performance in buildings. Appl. Energy 2017, 202, 420–434.

[11] Park, J.H.; Berardi, U.; Chang, S.J.; Wi, S.; Kang, Y.; Kim, S. Energy retrofit of PCM-applied apartment buildings considering building orientation and height. Energy 2021, 222, 119877.

[12] Ryms, M.; Klugmann-Radziemska, E. Possibilities and benefits of a new method of modifying conventional building materials with phase-change materials (PCMs). Constr. Build. Mater. 2019, 211, 1013–1024.

[13] Marani, A.; Nehdi, M.L. Integrating phase change materials in construction materials: Critical review. Constr. Build. Mater. 2019, 217, 36–49.

[14] Chihab, Y.; Bouferra, R.; Garoum, M.; Essaleh, M.; Laaroussi, N. Thermal inertia and energy efficiency enhancements of hollow clay bricks integrated with phase change materials. J. Build. Eng. 2022, 53, 104569.

[15] Sawadogo, M.; Duquesne, M.; Belarbi, R.; Hamami, A.E.A.; Godin, A. Review on the integration of phase change materials in building envelopes for passive latent heat storage. Appl. Sci. 2021, 11, 9305.

[16] Ben Romdhane, S.; Amamou, A.; Ben Khalifa, R.; Saïd, N.M.; Younsi, Z.; Jemni, A. A review on thermal energy storage using phase change materials in passive building applications. J. Build. Eng. 2020, 32, 101563.

[17] Ascione, F.; Bianco, N.; De Masi, R.F.; de' Rossi, F.; Vanoli, G.P. Energy refurbishment of existing buildings through the use of phase change materials: Energy savings and indoor comfort in the cooling season. Appl. Energy 2014, 113, 990–1007.

[18] Du, K.; Calautit, J.; Wang, Z.; Wu, Y.; Liu, H. A review of the applications of phase change materials in cooling, heating and power generation in different temperature ranges. Appl. Energy 2018, 220, 242–273.

[19] Drissi, S.; Mo, K.H.; Falchetto, A.C.; Ling, T.-C. Understanding the compressive strength degradation mechanism of cement-paste incorporating phase change material. Cem. Concr. Compos. 2021, 124, 104249.

[20] Bao, X.; Tian, Y.; Yuan, L.; Cui, H.; Tang, W.; Fung, W.; Qi, H. Development of high performance PCM cement composites for passive solar buildings. Energy Build. 2019, 194, 33–45.

[21] Kishore, R.A.; Bianchi, M.V.; Booten, C.; Vidal, J.; Jackson, R. Optimizing PCM-integrated walls for potential energy savings in U.S. Buildings. Energy Build. 2020, 226, 110355.

[22] Yang, Y.K.; Kim, M.Y.; Chung, M.H.; Park, J.C. PCM cool roof systems for mitigating urban heat island—An experimental and numerical analysis. Energy Build. 2019, 205, 109537.

[23] Abouebeid, S.; Hany, N.; Mosaad, G. Towards enhancing indoor environmental quality: A case of smart adaptive building envelopes in a coastal city. F1000Research 2022, 11, 731.

[24] Marszal-Pomianowska, A.J.; Johra, H.; Madsen, H.; Kazmi, H.S.; Knotzer, A.; Salom, J.; Lopes, R. Principles of Energy Flexible Buildings: Energy in Buildings and Communities Programme. 2020. Available online: https://www.annex67.org/media/1918/principles-of-energy-flexible-buildings.pdf (accessed on 15 August 2023).

[25] Hekimog˘lu,G.;Nas,M.;Ouikhalfan,M.;Sarı,A.;Tyagi,V.;Sharma,R.;Kurbetci,S.;Saleh,T.A.Silicafume/capricacid-stearicacid PCM included-cementitious composite for thermal controlling of buildings: Thermal energy storage and mechanical properties. Energy 2020, 219, 119588.

[26] Cabeza, L.F.; Navarro, L.; Pisello, A.L.; Olivieri, L.; Bartolomé, C.; Sánchez, J.; Álvarez, S.; Tenorio, J.A. Behaviour of a concrete wall containing micro-encapsulated PCM after a decade of its construction. Sol. Energy 2020, 200, 108–113.

[27] Omrany, H.; Chang, R.; Soebarto, V.; Zhang, Y.; Ghaffarianhoseini, A.; Zuo, J. A bibliometric review of net zero energy building research 1995–2022. Energy Build. 2022, 262, 111996.

[28] Posani, M.; Veiga, M.D.R.; de Freitas, V.P. Towards resilience and sustainability for historic buildings: A review of envelope retrofit possibilities and a discussion on hygric compatibility of thermal insulations. Thermal Insulations. Int. J. Arch. Heritage 2019, 15, 807–823.

[29] Gilka-Bötzow, A.; Folino, P.; Maier, A.; Koenders, E.A.B.; Caggiano, A. Triaxial failure behavior of highly porous cementitious foams used as heat insulation. Processes 2021, 9, 1373.

[30] Vaou, V.; Panias, D. Thermal insulating foamy geopolymers from perlite. Miner. Eng. 2010, 23, 1146–1151.

[31] Modesti, M.; Lorenzetti, A.; Besco, S. Influence of nanofillers on thermal insulating properties of polyurethane nanocomposites foams. Polym. Eng. Sci. 2007, 47, 1351–1358.

[32] Gonçalves, M.C.; Margarido, F. Materials for Construction and Civil Engineering; Springer: Cham, Switzerland, 2015.

[33] Arzumanyan, A. Technological peculiarities of non autoclaved foam concrete production on the base of volcanic pumice aggregates. In Materials Science. Mater. Sci. Forum 2019, 974, 206–210.

[34] Puga, H.; Carneiro, V.; Jesus, C.; Pereira, J.; Lopes, V. Influence of particle diameter in mechanical performance of Al expanded clay syntactic foams. Compos. Struct. 2018, 184, 698-703.

[35] Gao, H.; Liu, H.; Liao, L.; Mei, L.; Lv, G.; Liang, L.; Zhu, G.; Wang, Z.; Huang, D. Improvement of performance of foam perlite thermal insulation material by the design of a triple-hierarchical porous structure. Energy Build. 2019, 200, 21-30.

[36] Rugele, K.; Lehmhus, D.; Hussainova, I.; Peculevica, J.; Lisnanskis, M.; Shishkin, A. Effect of fly-ash cenospheres on properties of clay-ceramic syntactic foams. Materials 2017, 10, 828.

[37] Shishkin, A.; Bumanis, G.; Irtiseva, K.; Ozolins, J.; Korjakins, A. Clay Ceramic Hollow Sphere-Cement Syntactic Foam Composite for Building Applications. Key Eng. Mater. 2019, 800, 228-234.

[38] Fernando, P.; Jayasinghe, M.; Jayasinghe, C. Structural feasibility of Expanded Polystyrene (EPS) based lightweight concrete sandwich wall panels. Constr. Build. Mater. 2017, 139, 45-51.

[39] Maxwell, J.C. A Treatise on Electricity and Magnetism Dover Publications, Unabriged 3rd ed.; Dover Publications, Inc.: New York, NY, USA, 1954; Volume 1.

[40] Wellander, N. Homogenization of the Maxwell Equations: Case II. Nonlinear Conductivity. Appl. Math. 2002, 47, 255-283.

[41] Angell, T.S.; Kirsch, A. The conductive boundary condition for Maxwell's equations. SIAM J. Appl. Math. 1992, 52, 1597-1610.

[42] Nemilov, S.V. The review of possible interrelations between ionic conductivity, internal friction and the viscosity of glasses and glass forming melts within the framework of Maxwell equations. J. Non-Crystalline Solids 2011, 357, 1243-1263.

[43] Goncharenko, A.V. Generalizations of the Bruggeman equation and a concept of shape-distributed particle composites. Phys. Rev. E 2003, 68, 041108.

[44] Tjaden, B.; Cooper, S.J.; Brett, D.J.; Kramer, D.; Shearing, P.R. On the origin and application of the Bruggeman correlation for analysing transport phenomena in electrochemical systems. Curr. Opin. Chem. Eng. 2016, 12, 44-51.

[45] Liu, H.; Zhang, G.; Li, D.; Wang, C.; Bai, S.; Li, G.; Wang, G. Three-dimensional multi-phase simulation of cooling patterns for proton exchange membrane fuel cell based on a modified Bruggeman equation. Appl. Therm. Eng. 2020, 174, 115313.

[46] Myers, M.T. Pore Modeling: Extending the Hanai-Bruggeman Equation. In Proceedings of the SPWLA 30th Annual Logging Symposium, Denver, CO, USA, 11-14 June 1989.

[47] Sanjaya, C.S. Pore Size Effect on Heat Transfer through Porous Medium. Ph.D. Thesis, National University of Singapore, Singapore, 2011.

[48] Skibinski, J.; Cwieka, K.; Ibrahim, S.H.; Wejrzanowski, T. Influence of pore size variation on thermal conductivity of open-porous foams. Materials 2019, 12, 2017.

[49] Chen, J.; Wang, H.; Xie, P.; Najm, H. Analysis of thermal conductivity of porous concrete using laboratory measurements and microstructure models. Constr. Build. Mater. 2019, 218, 90-98.

[50] Lewis, T.B.; Nielsen, L.E. Dynamic mechanical properties of particulate-filled composites. J. Appl. Polym. Sci. 1970, 14, 1449-1471.

[51] Nielsen, L.E. The thermal and electrical conductivity of two-phase systems. Ind. Eng. Chem. Fundamentals 1974, 13, 17-20.

[52] Pal, R. On the Lewis-Nielsen model for thermal/electrical conductivity of composites. Compos. Part A Appl. Sci. Manuf. 2008, 39, 718-726.

[53] Kochetov, R.; Korobko, A.V.; Andritsch, T.; Morshuis, P.H.F.; Picken, S.J.; Smit, J.J. Three-phase lewis-nielsen model for the thermal conductivity of polymer nanocomposites. In Proceedings of the 2011 Annual Report Conference on Electrical Insulation and Dielectric Phenomena, Cancun, Mexico, 16-19 October 2011; pp. 338-341.

[54] Montes-De-Oca, L.M.; Medina-Esquivel, R.; Zambrano-Arjona, M.; MartiÃÅnez-Torres, P. Thermal detection of second critical micelle concentration in SDS and CTAB aqueous solutions using a modified Lewis-Nielsen effective thermal model. J. Mol. Liq. 2022, 363, 119864.

[55] Pietrak, K.; Wis ÃÅniewski, T.S. A review of models for effective thermal conductivity of composite materials. J. Power Technol. 2015, 95, 14-24.

[56] Wang, X.J.; Niu, X.H.; Qiu, X.W.; Istikomah, N.; Wang, L.B. Thermal conductivity of porous polymer materials considering pore special-shape and anisotropy. Express Polym. Lett. 2021, 15, 319-328.

[57] Javierre, E.; Vuik, C.; Vermolen, F.; van der Zwaag, S. A comparison of numerical models for one-dimensional Stefan problems. J. Comput. Appl. Math. 2006, 192, 445-459.

[58] Visintin, A. Models of Phase Transitions; Springer Science & Business Media: Berlin/Heidelberg, Germany, 1996; Volume 26.

[59] Gupta, S.C. The Classical Stefan Problem: Basic Concepts, Modelling and Analysis with Quasi-Analytical Solutions and Methods; Elsevier: Amsterdam, The Netherlands, 2017; Volume 45.

[60] Caggiano, A.; Mankel, C.; Koenders, E. Reviewing theoretical and numerical models for PCM-embedded cementitious composites. Buildings 2018, 9, 3.

[61] Mankel, C.; Caggiano, A.; KoÃànig, A.; Schicchi, D.S.; Sam, M.N.; Koenders, E. Modelling the thermal energy storage of cementitious mortars made with PCM-recycled brick aggregates. Materials 2020, 13, 1064.

[62] Voller, V.R.; Swaminathan, C.R.; Thomas, B.G. Fixed grid techniques for phase change problems: A review. Int. J. Numer. Methods Eng. 1990, 30, 875-898.

[63] SÃåavija, B.; Zhang, H.; Schlangen, E. Influence of microencapsulated phase change material (PCM) addition on (micro) mechanical properties of cement paste. Materials 2017, 10, 863.

[64] Dobri, A.; Tsiantis, A.; Papathanasiou, T.; Wang, Y. Investigation of transient heat transfer in multi-scale PCM composites using a semi-analytical model. Int. J. Heat Mass Transf. 2021, 175, 121389.

[65] SÃåavija, B.; Schlangen, E. Use of phase change materials (PCMs) to mitigate early age thermal cracking in concrete: Theoretical considerations. Constr. Build. Mater. 2016, 126, 332-344.

[66] Fachinotti, V.; Peralta, I.; Toro, S.; Storti, B.; Caggiano, A. Automatic Generation of High-Fidelity Representative Volume Elements and Computational Homogenization for the Determination of Thermal Conductivity in Foamed Concretes. 2022. Available online: https://ssrn.com/abstract=4286262 (accessed on 15 August 2023).

[67] Batool, F. Effect of Microstructure on Thermal Conductivity of Cement-Based Foam. Ph.D. Thesis, University of Alberta Libraries, Edmonton, AB, Canada, 2015.

[68] Awang, H.; Mydin, M.A.O.; Roslan, A.F. Effect of additives on mechanical and thermal properties of lightweight foamed concrete. Adv. Appl. Sci. Res. 2012, 3, 3326-3338.

[69] Wei, S.; Yiqiang, C.; Yunsheng, Z.; Jones, M. Characterization and simulation of microstructure and thermal properties of foamed concrete. Constr. Build. Mater. 2013, 47, 1278-1291.

[70] Mydin, M.A.O. Effective thermal conductivity of foamcrete of different densities. Concr. Res. Lett. 2011, 2, 181-189.

[71] Davraz, M.; KilincÃßarslan, S Ãß.; Koru, M.; Tuzlak, F. Investigation of relationships between ultrasonic pulse velocity and thermal conductivity coefficient in foam concretes. Acta Phys. Pol. A 2016, 130, 469-470.

[72] Oren, O.H.; Gholampour, A.; Gencel, O.; Ozbakkaloglu, T. Physical and mechanical properties of foam concretes containing granulated blast furnace slag as fine aggregate. Constr. Build. Mater. 2019, 238, 117774.

[73] Jiang, J.; Lu, Z.; Niu, Y.; Li, J. Investigation of the properties of high-porosity cement foams containing epoxy resin. Constr. Build. Mater. 2017, 154, 115-122.

[74] Jiang, J.; Lu, Z.; Niu, Y.; Li, J.; Zhang, Y. Investigation of the properties of high-porosity cement foams based on ternary Portland cement-metakaolin-silica fume blends. Constr. Build. Mater. 2016, 107, 181-190.

[75] Neville, A.M.; Brooks, J.J. Concrete Technology; Longman Scientific & Technical: New York, NY, USA, 1987; Volume 438.

[76] Tran, N.P.; Nguyen, T.N.; Ngo, T.D.; Le, P.K.; Le, T.A. Strategic progress in foam Stabilization towards high-performance foam concrete for building sustainability: A state-of-the-art review. J. Clean. Prod. 2022, 375, 133939.

[77] Kern, T. Neuses Verfahren zur experimentellen Untersuchung waÃàssriger SchaÃàume. Ph.D Thesis, University of Paderborn, Paderborn, Germany, 2002.

[78] Lohaus, L.; Pott, J.U. Konstruktionsleichtbeton unter Verwendung VorgeschaÃàumter Luftporen; Forschungsbericht; Institut fuÃàr Baustoffe, UniversitaÃàt Hannover: Hanover, Germany, 2005; Available online: https://www.baustoff.uni-hannover.de/de/ forschung/forschungsprojekte/forschungsprojekte-detailansicht/projects/konstruktionsleichtbeton-unter-verwendung- vorgeschaeumter-luftporen/ (accessed on 15 August 2023).

[79] Pott, J.U. Entwicklungsstrategien fuÃàr zementgebundene SchaÃàume. IfB. 2006. Available online: https://www.baustoff.uni-hannover.de/fileadmin/baustoff/publications/Heft05-Pott-ZemSchaum.pdf (accessed on 15 August 2023).

[80] Sam, M.; Caggiano, A.; Dubyey, L.; Dauvergne, J.-L.; Koenders, E. Thermo-physical and mechanical investigation of cementitious composites enhanced with microencapsulated phase change materials for thermal energy storage. Constr. Build. Mater. 2022, 340, 127585.

[81] Available online: https://issuu.com/detail-magazine/docs/978-3-920034-18-8_bk_de_daemmstoffe (accessed on 15 August 2023).

[82] Schild, K. WaÃàrmeschutz: Grundlagen-Berechnung-Bewertung; Springer: Berlin/Heidelberg, Germany, 2013.

Supplementary Materials:

S1. Below, a concise explanation of the experimental data utilized for validating the model is presented:

-Batool (2015) [67] tested cement-based foams by considering three levels of densities range: 400, 600 and 800 kg/m^3. The work provided thermal conductivities in low, middle, and high-porosities foams. The effect of replacing fly-ash, silica fume, and metakaolin, up to 20% by weight was also investigated to examine their influences on the thermal conductivity. In the study, the prominent pore size for the three densities, 800, 600 and 400, was shown to be 0.03 to 0.07 mm.

-Awang et al. (2012) [68] investigated the effects of different percentages of fly ash, lime and hydrophobic polypropylene fibres on the microstructure formation and thermal properties of lightweight foamed concrete. Three different densities of 600, 1000 and 1400 kg/m^3 were considered.

-Wei et al. (2013) [69] provided a comprehensive experimental and numerical analysis of foamed concretes with a large range of densities (300-1700 kg/m^3). A microstructure-based numerical model was proposed to predict the effective thermal conductivity of the foams with different porosities. The effect of convection and radiation on heat transfer for high and low porosity foamed concretes were also evaluated. The author unveiled that heat transfer due to convection can be neglected, because of the presence of predominantly closed-cell pores (smaller than 4 mm), while the radiation heat transfer was found to be a non-negligible factor for porosities higher than 85%. Under standard air pressure conditions and at 293 K, radiation contributed to approximately 6% of the overall heat transfer in these high porosity concretes.

-Mydin (2011) [70] conducted an experimental study on the effect of porosity and pore size on the thermal conductivity of foam concretes with seven variable densities (650, 700, 800, 900, 1000, 1100 and 1200 kg/m^3). The dominant pore size for densities between 650 and 1200 kg/m^3 was reported to be between 0.72 and 0.48 mm respectively. It was also shown that a reduction in foam density by 100 kg/m^3 leads to a decrease of the thermal conductivity by 0.04 W/mK.

-Davraz et al (2016) [71] presented a study on the correlation between dry densities, running from 350 to 1500 kg/m^3, and thermal conductivity of foam concretes with fine limestone and polypropylene fibers.

-Oren et al. (2020) [72] evaluated the thermo-physical properties of nine different foam concretes containing different volumetric amount of fly ash (FA) as binder, and granulated blast furnace slag (GBS) as fine aggregate by increasing the w/b ratio from 0.55 to 0.91. The study provides an in-depth analysis of the foam microstructure to explain the obtained experimental results.

-Jiang et al. (2017) [73] & (2016) [74] studied the effects of waterborne epoxy resin, silica fume and metakaolin on air-void structure and thermal conductivity in high porosity (> 90%) foams. The results indicated the presence of pore diameters less than 2.5 mm in all tested samples. When fine particles of SF (≤1 μm) and MK (1.0-9.5 μm) were added to the high porosity foams, the interparticle spacing would be reduced. The latter increased the real viscosity of the cement paste, depressed the bleeding, and accelerated the overlapping of particles These effects play a crucial role in stabilizing foams for producing highly porous cementitious systems with smaller bubbles, and ultimately leading to a decrease in thermal conductivity.

	Ultra-light	Low-density	Moderate strength	Structural
Compressive strength (MPa)	< 1	1-12	2-27	4-60
Elastic modulus (GPa)	< 1	1-4	2-6	4-18
Shrinkage (%)	> 0.3	0.2-0.3	1.1-0.2	< 0.1

Figure S1. foam type vs. properties classification according to [73, 74].

S2. Air-void shape/packing is determined based on the pore shape structure of cementitious foam, as shown in Figure 49. The packing is chosen according to the corresponding shape from the table below.

Table S1. Maximum packing fractions Φm for disperse phase with different shape and type of packing [49].

Shape of Particle	Type of packing	Maximum Packing fractions Φm
Spheres	Hexagonal close	0.7405
Spheres	Face centered cubic	0.7405
Spheres	Body centered cubic	0.60
Spheres	Simple cubic	0.524
Spheres	Random close	0.637
Spheres	Random loose	0.601
Rods or fibers	Uniaxial hexagonal close	0.907
Rods or fibers	Uniaxial simple cubic	0.785
Rods or fibers	Uniaxial random	0.82
Rods or fibers	Three dimensional random	0.52

Table S2. Value of A for Various Two-Phase Systems according to [49].

Shape/Type of dispersed phase	Direction of heat flow	A
Spheres	Any	1.5
Aggregates of spheres	Any	2.5/ Φm -1
Randomly oriented rods, Aspect ratio = 2	Any	1.58
Randomly oriented rods, Aspect ratio = 4	Any	2.08
Randomly oriented rods, Aspect ratio = 6	Any	2.8
Randomly oriented rods, Aspect ratio = 10	Any	4.93
Randomly oriented rods, Aspect ratio = 15	Any	8.38
Uniaxially oriented fibers	Parallel to fibers	2L/D
Uniaxially oriented fibers	Perpendicular to fibers	0.5

S3. Figures S2–S8 show the homogenized predicted conductivity values plotted against the employed data, analyzed author by author. The figures display both the linear regression lines and the square root errors. The prediction results show promising outcomes, with high R^2 values: e.g., 0.9756 for the Batool dataset [67], 0.9937 for Awang et al. [68], 0.9994 for Wei et al. [69], 0.9673 for Mydin [70], 0.9787 for Davraz et al. [71], 0.9793 for Oren et al. [72] and 0.8957 for Jiang et al. [73][74].

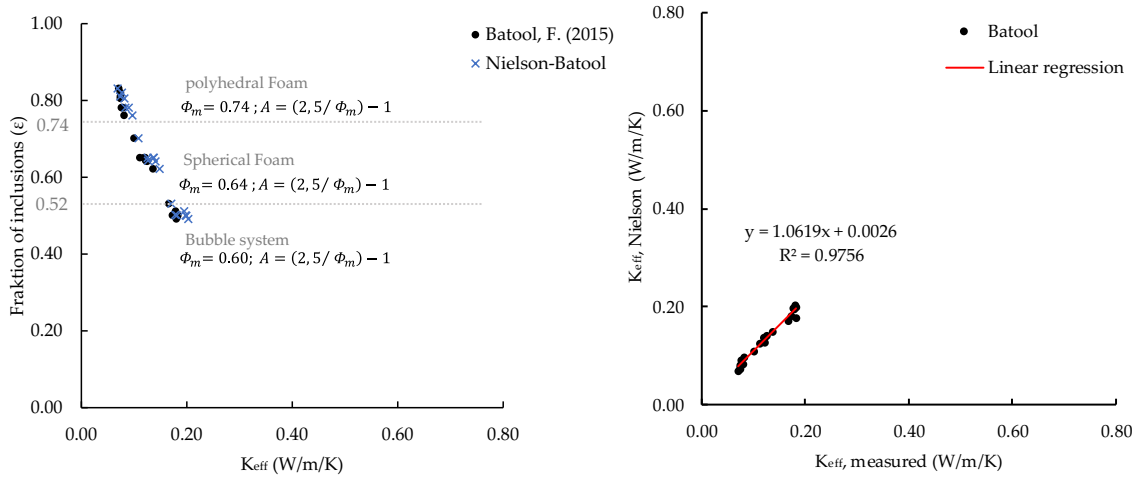

Figure S2. Lewis–Nielsen predictions vs. Batool data [67]: comparison and linear regression + R^2.

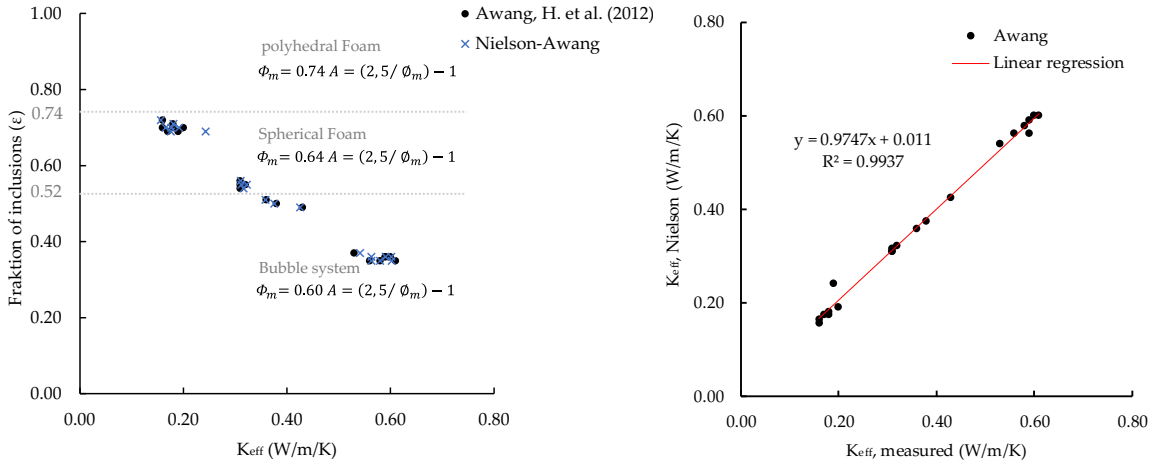

Figure S3. Lewis–Nielsen predictions vs. Awang data [68]: comparison and linear regression + R^2.

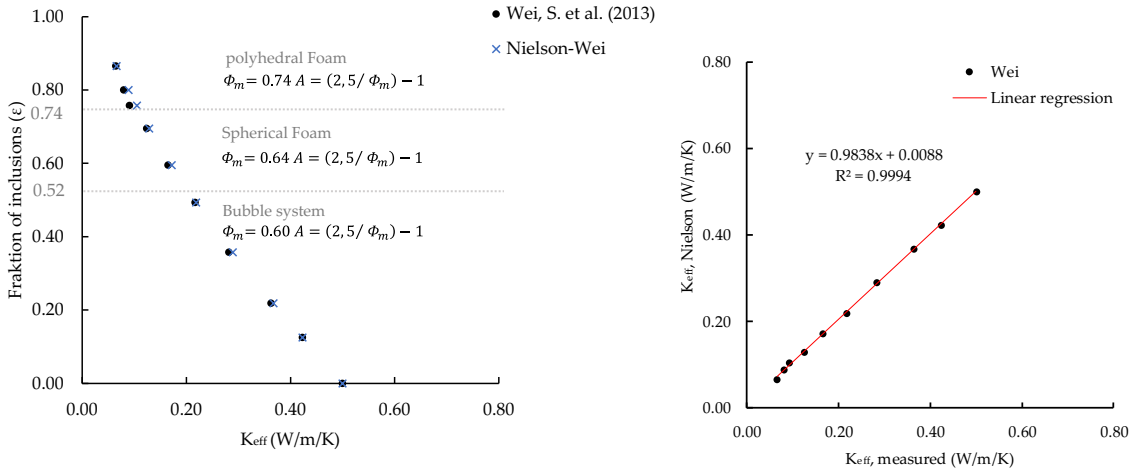

Figure S4. Lewis–Nielsen predictions vs. Wei data [69]: comparison and linear regression + R^2.

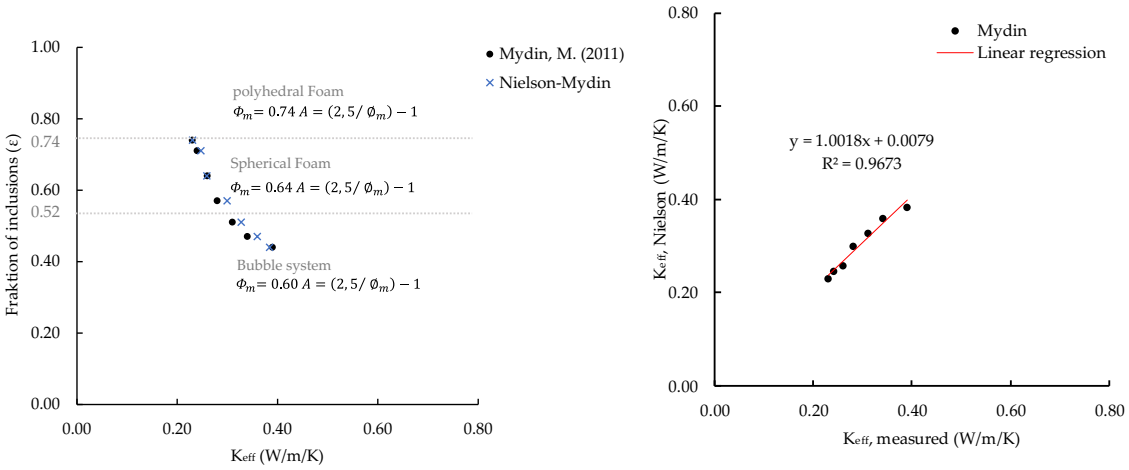

Figure S5. Lewis–Nielsen predictions vs. Mydin data [70]: comparison and linear regression + R^2.

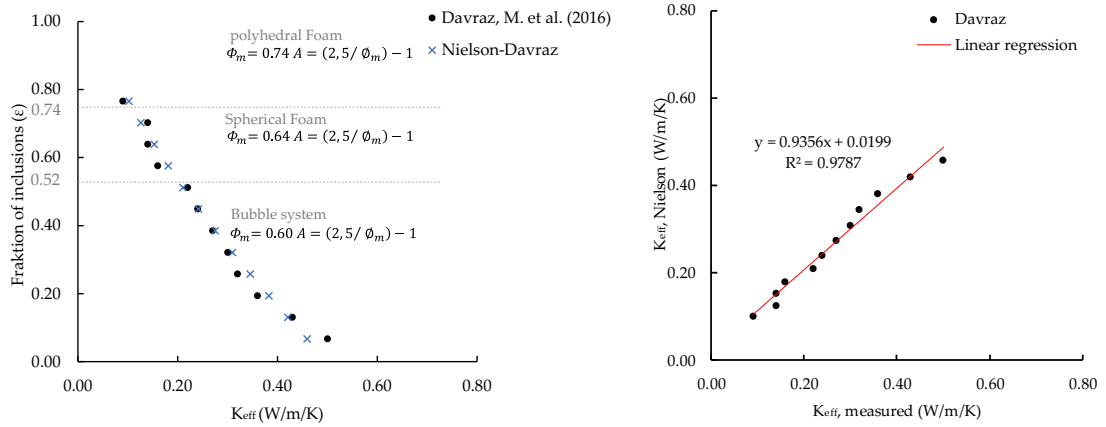

Figure S6. Lewis–Nielsen predictions vs. Davraz data [71]: comparison and linear regression + R^2.

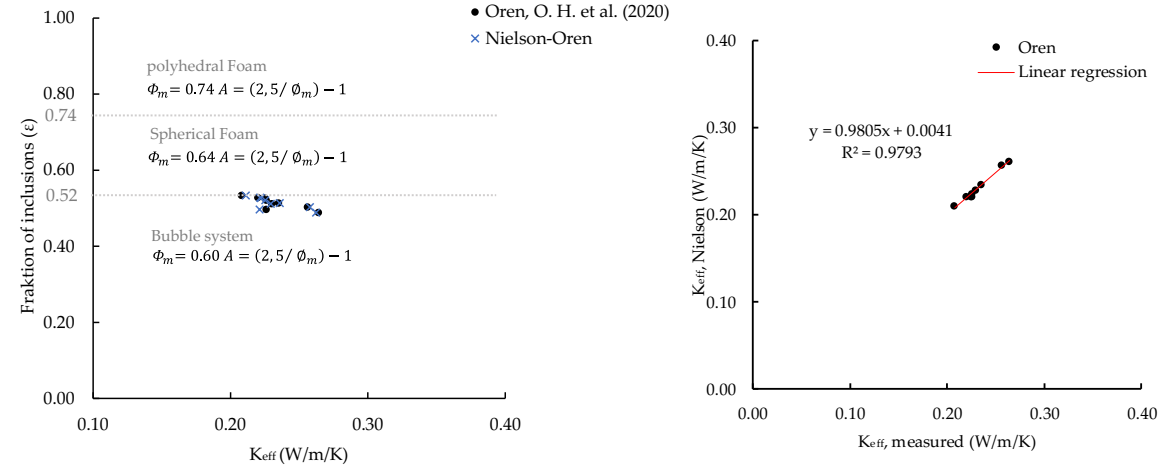

Figure S7. Lewis–Nielsen predictions vs. Oren data [72]: comparison and linear regression + R^2.

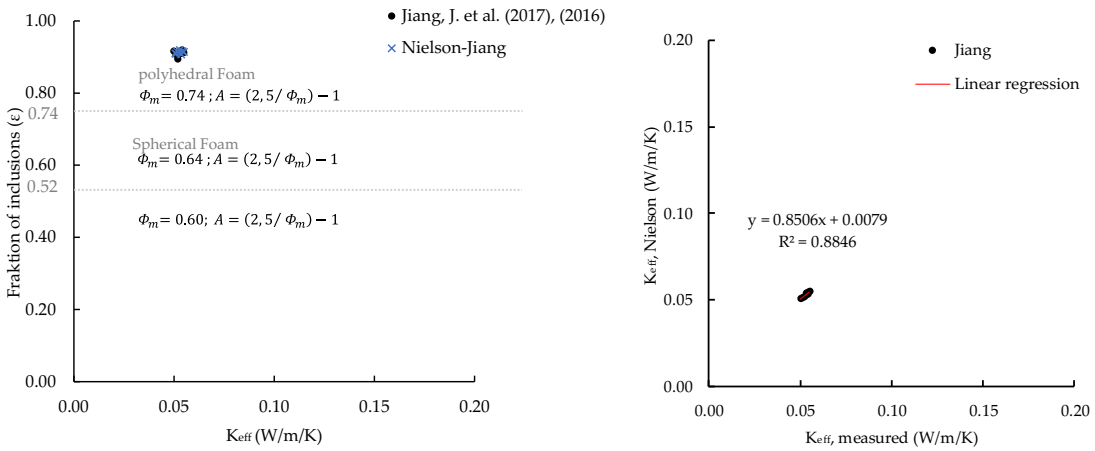

Figure S8. Lewis–Nielsen predictions vs. Jiang et al. (2017) [73] & (2016) [74]: comparison and linear regression + R^2.

S4. The overall heat transfer in foamed concretes, like in any porous media, is the result of three different mechanisms: conduction, convection, and radiation. The latter include both the heat conduction in cementitious matrix/skeleton together with the heat conduction, convection, and radiation within the air-fraction. In porous cementitious foam systems, heat transfer due to convection in air-voids can be neglected. Also, the effect of air radiation at low porosity is not relevant. The radiation contribution could only be an issue when the air volume fraction is over 85% [69].

Thermodynamics principles

The equation describing a heat transfer (conduction-only) problem can be written as:

$$\frac{\partial Q}{\partial t} = \nabla.(k\nabla T) + \dot{q}_v \forall \mathbf{x} \in \Omega \qquad (1)$$

being Q the heat of the system (time dependent, t), k is the thermal conductivity (which depends on temperature T and position x of the considered body Ω), $\dot{q}_v$ represents the possible source term, finally $\nabla.$ and ∇ are the divergence and gradient operators, respectively, of the Fourier's law of heat in Eq. (1).

To solve thermal problems involving phase changes, applicable for cementitious composites in building physics problems, the above equation of heat conduction can be written as follows:

$$\frac{\partial H}{\partial t} = \nabla.(k\nabla T) + \dot{q}_v \qquad \forall \boldsymbol{x} \in \Omega \qquad (2)$$

describing the heat conduction through a wall. Eq. (1) can be simplified and re-written in one dimensional format as:

$$q_x = -k\,A\frac{dT}{dx} \qquad (3)$$

being q_x the one dimensional heat flux (time dependent as well, t), A is the face area and dT/dx is the temperature gradient and measures how temperature changes with position x.

Enthalpy-based and Apparent Calorific Capacity Method

For simulating thermal storage phenomena in porous cementitious foam composites, the Apparent Calorific Capacity (ACCM) is a simple method, based on the assumption that the schematized material acts as a homogenous medium and can be applied to simulate phase change processes. The latter provides a description of the enthalpy evolution of a system in terms of an apparent heat capacity (including the latent heat in the specific heat) during thermal phase changes. Thus, starting from Eq. (2), commonly known as the enthalpy-based method, and adopting the following chain rule:

$$\frac{\partial H}{\partial t} = \frac{\partial H}{\partial T}\frac{\partial T}{\partial t} \tag{4}$$

and by introducing the so-called temperature-dependent apparent heat capacity, defined as:

$$\frac{\partial H}{\partial T} = \rho C_{p,eff}(T) \tag{5}$$

hence, Eq. (2) modifies into the following non-linear ACCM transient heat equation:

$$\rho C_{p,eff}(T)\frac{dT}{dt} = \nabla.(k\nabla T) \tag{6}$$

To complete the above problem statement of the ACCM approach, Initial (ICs) and Boundary Conditions (BCs) need to be employed, as defined here below:

$$T(x,t) = T_0 \qquad \text{when t=0}$$

$$T(x,t) = T_{left} \qquad \text{at } x = L$$

$$T(x,t) = T_{right} \qquad \text{at } x = 0$$

2.4 Synthesis

This synthesis highlights the collective contribution of papers in this chapter toward advancing the field of energy-efficient building materials and systems. The three individual papers presented in this PhD thesis share a common focus on the utilization of phase change materials (PCMs) for thermal energy storage, particularly within the context of blended cementitious composites. Each paper provides valuable results into different aspects and scales, highlighting various approaches, materials, and performance evaluations. When viewed collectively, all papers offer a comprehensive perspective on the potential of PCM-enhanced cementitious materials for sustainable thermal energy storage solutions.

The **first paper as first sub-research objective** aimed to assess the current properties of PCM materials, determined their characteristics, and evaluated their potential for implementation. Findings in this regard provide valuable Knowledge into how to conduct PCM characterization and integrate them into Thermal Energy Storage (TES) calculations, especially for building applications and simulations. A detailed and fundamental experimental procedure was reported for analyzing the TES capacity of paraffin-based and bio-based PCM. By considering multiple types of PCMs, the research provides a comprehensive and wide-ranging Understanding into the field. This variety in the studied materials increase the validity of the findings to a wider range of applications. The results demonstrate the feasibility of transitioning to environmentally friendly biobased PCMs as a substitution for paraffins, as exemplified by the remarkable TES capacity of 227.74 J/g (pureTemp25) in comparison to RT25 with a TES capacity of 230.31 J/g. The latter serves as a reference point for the sustainable development of Latent Heat Thermal Energy Storage (LHTES) composite materials, as presented in the two subsequent objectives.

Additionally, the study has taken initial steps towards the development of a new generation of storage materials derived from bio-waste recycling processes, as indicated by patented research in the framework of this PhD study[2] and within the context of first sub-research objective. This innovation holds significant importance for sustainable development across all three levels considered in this study.

In relation to the **second paper or second sub-research objective**, an extensive study on blended cementitious composites enhanced with Microencapsulated Phase Change Materials (MPCMs) demonstrated the remarkable potential of MPCMs in reducing thermal conductivity, increasing heat capacity, and improving heat flow control in mineral composites. In this context, the results and methods from the first research objective flow synergistically into the research to obtain the optimum thermal capacity and valuable, reliable results. Regarding rheological and mechanical properties, the optimized mixture design was suggested to achieve a balance between durability and thermal performance by incorporating environmentally friendly supplementary materials as substitutes for cement, with the maximum possible utilization recommended. Additionally, the achieved thermo-physical results, including specific heat

[2] https://patentscope.wipo.int/search/en/detail.jsf?docId=DE391896767&_cid=P10 LEPCLD

capacity, density, and conductivity, of blended cement paste, PCM, and MPCM were used for further analysis and the development of a model related to the third sub-research question.

With respect to the **third sub-research objective in the third paper**, an analytical approach was developed for blended cementitious composites with varying porosity. This approach provided a comprehensive description and highly precise prediction of the materials' thermal behavior, focusing on different porosity levels and matrix conductivity. As a result, a new classification of mineral foam composites into three classes, Class I, Class II, and Class III, each one characterized by unique characteristics, was established.

All three papers contribute to the advancement of sustainable building practices and thermal energy management. Furthermore, the significance of material selection and characterization is highlighted in the papers, considering factors such as thermal properties, sustainability, and compatibility with existing construction materials. Moreover, they emphasize the importance of comprehensive performance evaluations, which combine thermophysical, mechanical, and modeling aspects to provide a total understanding of PCM-enhanced composites. The papers support the integration of PCM technology into real-world applications, underlining the potential for energy savings in buildings and other infrastructures.

3 Conclusion and Outlook on Future Research

This PhD study aimed to achieve its **primary research objective** outlined in chapter 1.2 “Empirical and Theoretical demonstration of the Influence of Sensible and Latent Heat Storage on the Insulation Capacity of Porous blended cement-based Composites” and evaluate the choice between insulation and (or versus) thermal energy storage based on three sub-research questions. Through this comprehensive investigation into the dynamics of thermal energy storage and insulation, along with their synergy, this work achieved observations for enhancing energy efficiency and thermal comfort in building applications. Main findings related to the primary research objective can be summarized as follows:

- Highly porous mineral composites (i.e., $\varepsilon > 0.74$), as a standalone solution, demonstrates remarkable promise in sustainable building design and energy management. These materials exhibit high thermal mass ($\rho\, C_{p,\varepsilon\, 0.9}$=223.120 kJ/m^3/K compared to EPS=45 kJ/m^3/K) and can serve as the foundation for the integration of an effective thermal storage system. They significantly reduce the heat transfer by acting as a thermal barrier, with an almost 59-65% lower thermal diffusivity (α) compared to EPS layers (α_{foam}= 0.03 x 10^{-5} m^2/s vs. α_{EPS}= 0.08 x 10^{-5} m^2/s). In essence, a lower thermal diffusivity effectively mitigates the impact of thermal bridges, reducing heat loss and/or gain, and thereby improving the overall energy efficiency by reducing indoor heat and electricity demand.
- The incorporation of microencapsulated Phase Change Materials (MPCMs) in highly Porous mineral composites significantly enhances energy performance. For instance, a 30% increase in insulation/thermal performance of thermal energy storage foam (TESS) material is achieved by adding 2 vol.% MPCMs to blended cementitious composite with 90% porosity, as shown in Figure 61. These materials perform by undergoing phase transitions at specific temperature ranges, absorbing, or releasing excessive environmental/indoor heat in the process. When integrated into building envelopes, they act as a buffer against defined temperature fluctuations, effectively stabilizing indoor conditions within the designed temperature range and reducing overall energy consumption.

- A higher thermal effusivity (b) indicates a greater capacity for both material thermal conductivity (namely, the ability to conduct heat) and volumetric heat capacity (i.e., the ability to store heat). When the surrounding material of the (MPCMs) exhibits a higher thermal effusivity, it can transfer heat more efficiently to and from the MPCM. This facilitates the activation of the PCM, resulting in a more efficient thermal energy storage process.

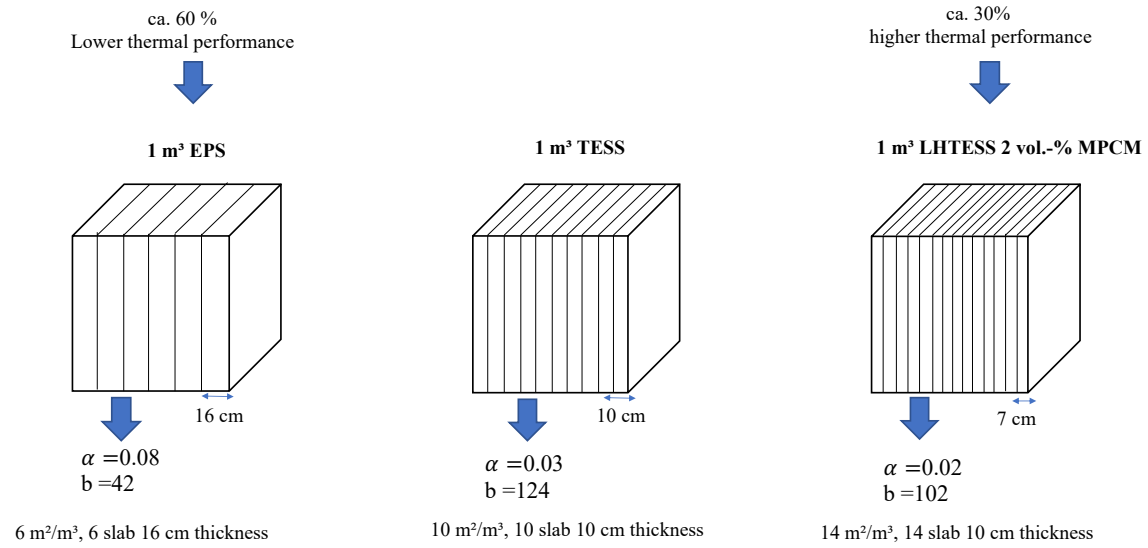

Figure 61: Evaluating the thermal performance of EPS and LHTESS in Comparison to TESS: illustration of resource consumption to achieve consistent thermal performance in m^2.

Three additional important aspects, arising from the comparisons of TESS and LHTESS with commercial materials, include:

- Resource Consumption: With the phase change and associated heat storage, the innovative TESS insulation material can save up to 75% of the material compared to commercial insulation materials. This enables a significant increase in insulation performance with the same material thickness while optimizing the indoor climate of buildings and reducing CO_2 emissions. The latter highlights its remarkable resource efficiency, making the materials a more sustainable choice.
- Recycling: Mineral foam can be recycled more effectively due to their composition and high market demand.

Considering the findings in this study and the conclusions drawn in line with the main research objective, the **main research question** addressed in Chapter 1.4, 'Insulation vs. Insulation with Heat Storage/Release Functionality', can be addressed as follows:

- As we attempt for a more sustainable and energy-efficient future, with the goal of achieving a zero-emission building stock by 2050, the integration of insulation together with thermal energy storage systems will be essential in reducing heating and specially cooling demands and advancing cleaner renewable energy sources.
- Both insulation and thermal energy storage have unique advantages and are essential components of sustainable building design and energy management. Insulation plays a fundamental role in

enhancing the overall thermal performance of buildings and mitigating thermal bridging. Thermal Energy Storage, as a complementary strategy in combination with insulation, is essential for optimizing energy usage and achieving a significant reduction in peak energy demand, especially in the context of summer heat protection and lowering electricity consumption for cooling.

In this regard, TES mineral foam systems provide a unique approach for building insulation, featuring adjustable thermal conductivity in contrast to traditional methods. This technology has demonstrated promising outcomes in increasing thermal inertia by varying the envelope's thermal resistance according to specific operational periods throughout the year. The study's empirical and theoretical findings validate the impact of sensible and latent heat storage on the insulating properties of porous blended cementitious composites. These results favor the selection of insulation materials with integrated thermal energy storage, as determined through a comprehensive study within the scope of three sub-research questions.

Despite the significant contributions made, this study acknowledges several **limitations**.

- **Experimental Scope**: The study had limitations due to the lack of available data in the sustainable biobased PCM field, coming from the limited availability of biobased materials in the market and the insufficient research and development in this area. These materials are essential for the future sustainable development of TES materials and composites.
- **Context Dependence**: The effectiveness of insulation, thermal energy storage, or their combination is context dependent. Factors such as extreme climate, unusual building design, and specific energy consumption patterns could potentially limit the effectiveness of the results, requiring customized solutions.
- **Environmental Considerations:** While the environmental impact of materials is an important concern, the scope of this PhD study doesn't allow for an extensive evaluation of long-term performance, stability, life cycle assessments, or the full spectrum of sustainability aspects of the materials and components applied in this study.

To build upon this work and address its limitations, future research is suggested to investigate advanced mineral materials for similar applications, optimizing the current state of thermal energy storage using PCMs, and developing integrated control strategies for PCM activation/deactivation. This can enhance the synergy between material insulation properties and thermal energy storage. Moreover, a detailed study of the environmental impacts and long-term performance of these strategies is important in bridging the gap toward effective, eco-friendly, and adaptable thermal energy storage solutions. Specific steps for **future research** can be listed as:

- **Expanded material exploration for encapsulation**: Investigattion of a broader range of formaldehyde-free microcapsules and assess their suitability in various mineral contexts.
- **Sustainability analysis:** Comprehensive life cycle assessments to evaluate the environmental impact of materials and systems proposed in this study, ensuring alignment with sustainability goals.
- **Real-World testing**: Implementation of real-world testing (i.e., different climate and/or meteorological conditions) along with long-term monitoring of the proposed composites in buildings

that incorporate different insulation and thermal energy storage strategies to validate theoretical findings and assess durability and reliability.

In conclusion, the synergy between insulation, thermal energy storage, and their combined use is multifaceted and demands careful consideration. This research has established the foundation for understanding their benefits, offering a platform for further advancements in sustainable building practices and energy management.